Chemical Science

ROYAL SOCIETY OF CHEMISTRY

EDGE ARTICLE

View Article Online
View Journal | View Issue

Cite this: *Chem. Sci.*, 2023, **14**, 298

All publication charges for this article have been paid for by the Royal Society of Chemistry

Insights into the thermodynamic–kinetic synergistic separation of propyne/propylene in anion pillared cage MOFs with entropy–enthalpy balanced adsorption sites†

Yunjia Jiang,‡[a] Lingyao Wang,‡[a] Tongan Yan,‡[b] Jianbo Hu,‡[c] Wanqi Sun,[a] Rajamani Krishna,[d] Dongmei Wang,[a] Zonglin Gu,[e] Dahuan Liu,[b] Xili Cui,[c] Huabin Xing[c] and Yuanbin Zhang*[a]

Propyne/propylene (C_3H_4/C_3H_6) separation is an important industrial process yet challenged by the trade-off of selectivity and capacity due to the molecular similarity. Herein, record C_3H_4/C_3H_6 separation performance is achieved by fine tuning the pore structure in anion pillared MOFs. SIFSIX-Cu-TPA (ZNU-2-Si) displays a benchmark C_3H_4 capacity (106/188 $cm^3\ g^{-1}$ at 0.01/1 bar and 298 K), excellent C_3H_4/C_3H_6 IAST selectivity (14.6–19.3) and kinetic selectivity, and record high C_3H_4/C_3H_6 (10/90) separation potential (36.2 mol kg^{-1}). The practical C_3H_4/C_3H_6 separation performance is fully demonstrated by breakthroughs under various conditions. 37.8 and 52.9 mol kg^{-1} of polymer grade C_3H_6 can be produced from 10/90 and 1/99 C_3H_4/C_3H_6 mixtures. 4.7 mol kg^{-1} of >99% purity C_3H_4 can be recovered by a stepped desorption process. Based on the *in situ* single crystal analysis and DFT calculation, an unprecedented entropy–enthalpy balanced adsorption pathway is discovered. MD simulation further confirmed the thermodynamic–kinetic synergistic separation of C_3H_4/C_3H_6 in ZNU-2-Si.

Received 15th October 2022
Accepted 22nd November 2022

DOI: 10.1039/d2sc05742e

rsc.li/chemical-science

Introduction

Propylene (C_3H_6) is the world's second largest volume hydrocarbon with the global production capacity exceeding 140 million tons in 2020. It is a basic olefin feedstock for the manufacture of various polymers and chemicals such as polypropylene and propylene oxide.[1] Originating from the cracking of crude oil, C_3H_6 is inevitably mixed with a small amount of propyne (C_3H_4), which must be reduced to a ppm level before further processing as it can severely poison the C_3H_6 polymerization catalysts.[2] The state-of-the-art industrial technologies for the removal of C_3H_4 from C_3H_6 rely on noble-metal catalyst based selective hydrogenation, which suffers from several drawbacks such as high cost, low efficiency and potential secondary pollution. On the other hand, C_3H_4 that can be manufactured from the catalytic or thermal pyrolysis of C_3H_6 is also a fundamental material for speciality fuel and chemical intermediates.[3] To recover C_3H_4, solvent extraction is the current dominant technology, which is not only energy intensive but also associated with pollution. Thus, it is of urgent importance to develop new technologies for efficient C_3H_4/C_3H_6 separation.

Adsorptive separation based on porous solid adsorbents has been recognized as a promising alternative technology for gas/vapor separation because of its eco-friendly nature and energy efficiency.[4–10] However, due to the great similarity in the molecular size (C_3H_4: 4.16 × 4.01 × 6.51 $Å^3$, C_3H_6: 4.65 × 4.16 × 6.44 $Å^3$) and polarizability (C_3H_4: 55.5 × 10^{-25} cm^3, C_3H_6: 62.6 × 10^{-25} cm^3), the adsorptive separation of C_3H_4/C_3H_6 by molecular recognition is still very challenging.[11] Only two examples of zeolites are reported and their C_3H_4 capacity is relatively low.[10] Recently, metal–organic frameworks (MOFs) with tuneable pore size/shape and chemistry have emerged as a new class of porous materials for the separation of C_3H_4/C_3H_6.[12–27] Among them, **pcu** type anion pillared MOFs (APMOFs) with strong Lewis basic functional sites display the benchmark separation performance.[12–18] Nonetheless, the trade-off between the capacity and selectivity is still a critical problem to overcome.

[a]*Key Laboratory of the Ministry of Education for Advanced Catalysis Materials, College of Chemistry and Life Sciences, Zhejiang Normal University, Jinhua 321004, China. E-mail: ybzhang@zjnu.edu.cn*

[b]*State Key Laboratory of Organic-Inorganic Composites, Beijing University of Chemical Technology, Beijing 100029, China*

[c]*Department of Chemistry, Zhejiang University, 38 Zheda Road, 310027 Hangzhou, P. R. China*

[d]*Van't Hoff Institute for Molecular Sciences, University of Amsterdam, Science Park 904, 1098 XH Amsterdam, Netherlands*

[e]*College of Physical Science and Technology, Yangzhou University, Jiangsu, 225009, China*

† Electronic supplementary information (ESI) available. CCDC 2190367–2190372. For ESI and crystallographic data in CIF or other electronic format see DOI: https://doi.org/10.1039/d2sc05742e

‡ These authors contributed equally to this work.

For example, SIFSIX-3-Ni (pore size = 4.2 Å, Scheme 1a) as a single-molecule trap for C_3H_4 can afford extremely high C_3H_4/C_3H_6 selectivity (>200), but the capacity of C_3H_4 is only 67 $cm^3\ g^{-1}$; SIFSIX-1-Cu (pore size = 8.0 Å, Scheme 1b) can accommodate a large amount of C_3H_4 (201 $cm^3\ g^{-1}$) by cooperative host–guest interactions, but the separation selectivity is <10. Besides, these pillared layered SIFSIX MOFs are not chemically stable and some are even sensitive to humid air, which hinders the practical applications.[8d,28] On the other hand, the kinetic separation of C_3H_4/C_3H_6 has never been reported.

Anion pillared cage-like MOFs with **ith-d** topology are a new class of APMOFs.[27,29] The rational combination of anion pillars and tridentate organic linkers provides anion sustained cage-like APMOFs with ultrahigh chemical stability. In 2021, Wu *et al.* discovered the first pillar-cage **ith-d** MOF SIFSIX-Cu-TPA (Scheme 1c) with a complete SiF_6^{2-} cross-link for CO_2/C_2H_2 separation.[29] Soon after, our group reported independently an isomorphic MOF termed ZNU-2 (TIFSIX-Cu-TPA).[27] Considering the slight change of the organic linker, the metal ion or anion pillar in **pcu**-type APMOFs can lead to a dramatic separation difference, we envision that tuning the pore aperture and pore window in cage-like APMOFs can also be applied to tune the gas adsorption properties. Nonetheless, the length and angle matching between the tridentate ligand and anion pillar is very significant to construct the pillar embedding structures. Pillar-cage Tripp-Cu-SIFSIX with the overlong organic linker 2,4,6-tris(4-pyridyl)pyridine is not stable upon guest removal since the mononuclear Cu ion center is only half sustained by SiF_6^{2-} and coordination unsaturated.[30] $[Cu_3(SiF_6)_3(TMTPB)_4]$ (FJI-W1) with triangular ligand 1,3,5-trimethyl-2,4,6-tris(4-pyridyl) benzene belongs to pillar-layer APMOFs that feature 1D hexagonal channels.[26] Thus, only the modification of the anion pillar or metal ion (size difference < 0.1 Å) is a good alternative to fine-tune the pore structure and chemistry while retaining the topology. Furthermore, the integration of large cages and narrow interlaced channels has the potential to show a kinetic difference for C_3H_4 and C_3H_6 molecules with a slight diameter difference (Scheme 1d), which has not been explored in theory yet.

With this in mind, herein we prepared three isomorphic APMOFs using SiF_6^{2-}, TiF_6^{2-}, and $NbOF_5^{2-}$ as the pillars, and investigated the C_3H_4/C_3H_6 adsorption and separation performance. To our delight, these three reticular MOFs exhibit quite distinctive but ordered C_3H_4 adsorption capacity as well as C_3H_4/C_3H_6 selectivity. The pore size follows the sequence of SIFSIX-Cu-TPA < TIFSIX-Cu-TPA < NbOFFIVE-Cu-TPA while the C_3H_4 adsorption capacity and the separation selectivity are both SIFSIX-Cu-TPA > TIFSIX-Cu-TPA > NbOFFIVE-Cu-TPA. Benchmark high uptakes of C_3H_4 are observed both at low pressure (106 STP $cm^3\ g^{-1}$ at 0.01 bar and 298 K) and normal pressure (188 STP $cm^3\ g^{-1}$ at 1 bar and 298 K) on SIFSIX-Cu-TPA. The C_3H_4 storage density reached 0.60 and 0.65 g cm^{-3} at 298 and 278 K, 89% and 97% of the liquid C_3H_4 density. The calculated IAST selectivity is 14.6–19.3 depending on the ratio of C_3H_4/C_3H_6 (1/99–50/50). Record high C_3H_4/C_3H_6 (10/90) separation potential (36.2 mol kg^{-1}) is obtained, which is 65% higher than the previous benchmark of NKMOF-11 without anion functionalities. The modestly high C_3H_4 adsorption heat of 43.2 kJ mol^{-1} is advantageous for both C_3H_4 adsorption and facile regeneration. Simulated breakthroughs indicated SIFSIX-Cu-TPA displays the best separation performance for C_3H_4/C_3H_6 (10/90) mixtures. Practical separations of C_3H_4/C_3H_6 (50/50, 10/90, 1/99) mixtures were also confirmed by breakthrough experiments. Notably, the practical separation performance is even superior to that of simulation due to the kinetic enhancement, which has never been reported in C_3H_4/C_3H_6 separation. 37.8 and 52.9 mol kg^{-1} of C_3H_6 is produced from the 10/90 and 1/99 C_3H_4/C_3H_6 mixtures, respectively. The productivity is increased to 79.2 mol kg^{-1} when the process temperature decreased to 278 K. Such high productivity has never been achieved by chemically stable porous materials. 4.7 mol kg^{-1} of >99% purity C_3H_4 can be recovered. Repeated

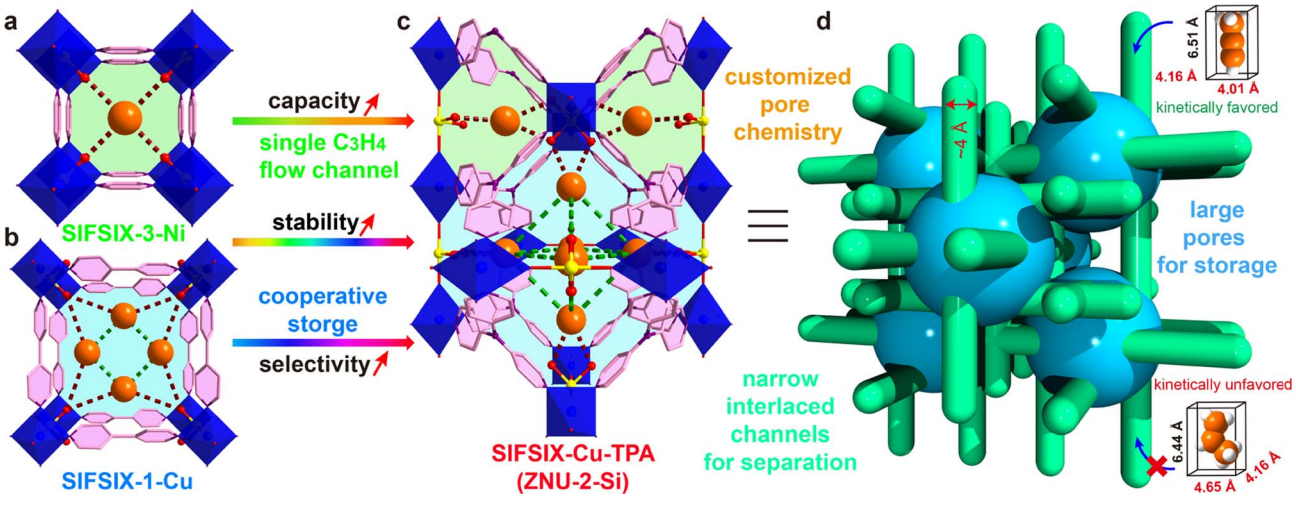

Scheme 1 Strategies to overcome the trade-off of capacity and selectivity in C_3H_4/C_3H_6 separation in a stable cage-like APMOF by the thermodynamic–kinetic synergism mechanism. (a) Structure of SIFSIX-3-Ni. (b) Structure of SIFSIX-1-Cu. (c) Structure of SIFSIX-Cu-TPA. (d) Illustration of the thermodynamic–kinetic cooperation for C_3H_4/C_3H_6 separation.

breakthrough experiments under dry or humid conditions showed the complete retention of separation performance, confirming the high stability of SIFSIX-Cu-TPA for practical separations. The *in situ* single crystal structure of C_3H_4-loaded SIFSIX-Cu-TPA directly demonstrates the C_3H_4 binding configuration under near-saturation conditions, which is distinct from the previous study.[27] Comprehensive modelling studies including Grand Canonical Monte Carlo (GCMC) simulations, Molecular Dynamics (MD) simulations and Density Functional Theory (DFT) calculations were completely applied to investigate the adsorption/separation process, which indicated that the contracted channel serves as a single molecule flow channel that differentiates C_3H_4/C_3H_6 kinetically while the large cage provides high affinity for C_3H_4 adsorption by cooperative host–guest and guest–guest interactions. To the best of our knowledge, the kinetic separation of C_3H_4/C_3H_6 has for the first time been revealed by MD simulations. The obvious thermodynamic–kinetic synergism in breakthroughs has never been reported in porous materials for C_3H_4/C_3H_6 separation. Moreover, our study unprecedentedly disclosed the important role of entropy effects on C_3H_4 adsorption and gas cluster assembly in the pores while the GCMC and DFT based gas binding configuration may not reflect the practical gas binding sites due to the neglect of the entropy effect.

Results and discussion

The single crystals of isostructural SIFSIX-Cu-TPA (ZNU-2-Si), TIFSIX-Cu-TPA (ZNU-2-Ti) and NbOFFIVE-Cu-TPA (ZNU-2-Nb) are all produced by layering a MeOH solution of TPA onto an aqueous solution of CuX (X = SiF_6^{2-}, TiF_6^{2-}, $NbOF_5^{2-}$). ZNU-2-Nb has been reported for the first time (Fig. 1a and b). All of these three coordination complexes crystallize in three-dimensional (3D) frameworks with the cubic $Pm\bar{3}n$ space group (Table S1†). The frameworks consist of large icosahedral cages (~8.5 Å, Fig. 1c) with 12 outlets and narrow interlaced channels (~4 Å, Fig. 1d) that connect four independent cages (Fig. S6 and S7†). The large cages have abundant Lewis basic F binding sites in the surface for C_3H_4 adsorption and storage. Such interconnected 3D channel pores (Fig. 1e) are distinct from those of pillar-layer MOFs (*e.g.* SIFSIX-3-Ni) with straight 1D channels. Due to the tiny size difference of anion pillars, the pore aperture and channel diameter also show a very slight difference (<0.05 Å), which is reflected in the N···N and Cu···Cu distances (Fig. 1f). As the channel diameter is very close to the cross-sections (4.01 × 4.16 $Å^2$ for C_3H_4 and 4.65 × 4.16 $Å^2$ for C_3H_6), a slight shrinking of the channel may provide a much enhanced kinetic difference in C_3H_4/C_3H_6 adsorption. Thus, ZNU-2-Si with a reduced channel diameter has the potential to show a remarkable kinetic difference in C_3H_4 and C_3H_6 adsorption. In brief, ZNU-2-Si features the most promising structure to offer benchmark C_3H_4/C_3H_6 separation performance by thermodynamic–kinetic synergism.

Before gas adsorption experiments, the chemical and thermal stability of ZNU-2-M is fully studied since stability is a prerequisite for practical use in real-world systems. To our delight, all three materials are highly stable in humid air and water as indicated by the PXRD patterns (Fig. S12, S14 and S15†). To provide straightforward evidence, we take photographs of the single crystals of ZNU-2-M after different

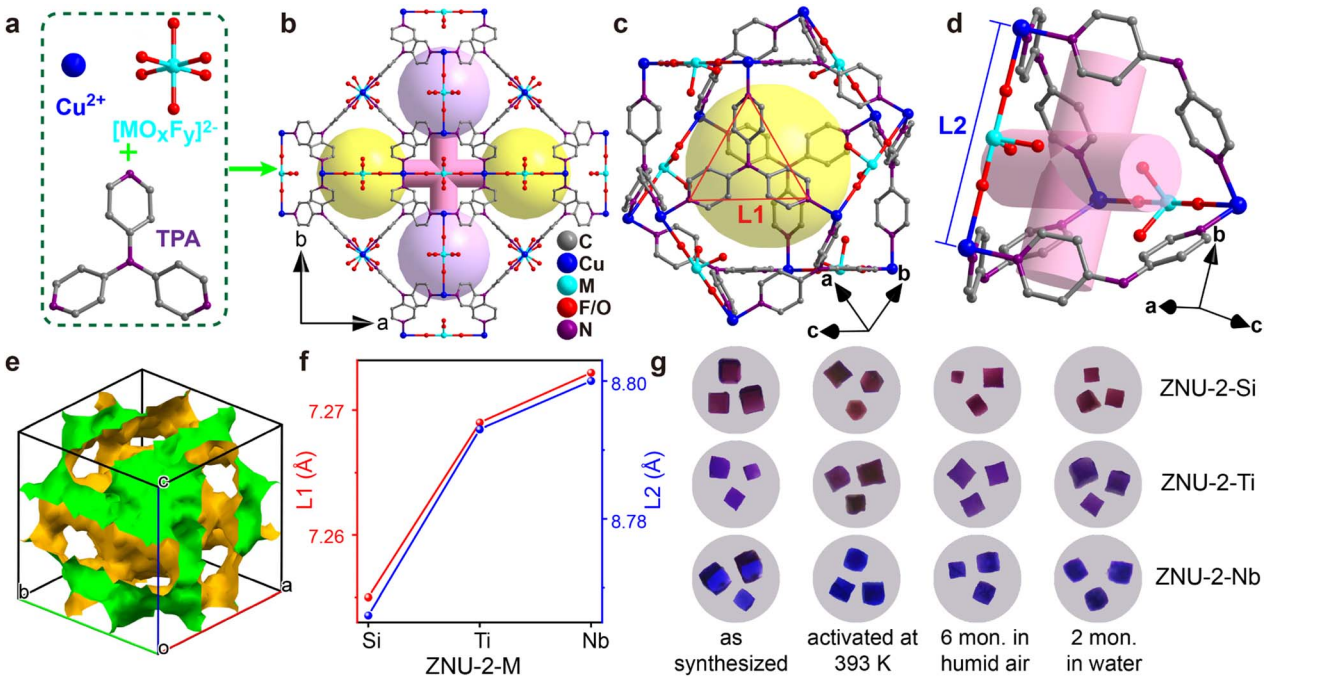

Fig. 1 Porous structure and stability test of ZNU-2-M (M = Si, Ti, Nb). (a) Basic units to construct ZNU-2-M. (b) Structure of ZNU-2-M with cage-like pores and interlaced channels. (c) Structure of the icosahedral Cu^{II} cage with the N···N distance (L1) of TPA highlighted. (d) Structure of the interlaced channel between four cages with the Cu···Cu distance (L2) highlighted. (e) The voids of ZNU-2-Si illustrating the interlinked 3D channels. (f) Comparison of the L1 and L2 among ZNU-2-M. (g) Optical microscopy of single crystals of ZNU-2-M (M = Si, Ti, Nb) after different treatments.

treatments (Fig. 1g, S86, S88 and S90†). As shown, the single crystals are still of high quality after being left in humid air for 6 months, soaking in water for 2 months, soaking in acidic and basic aqueous solutions or exposure to humid HCl vapor at 323 K for 3 h. Heating at 393 K under vacuum provides desolvated ZNU-2-M with the same crystal structure as indicated by single crystal and powder XRD analysis (Fig. 1g, S11, S14, S15 and S86–S90†). TGA curves showed that the framework of ZNU-2-M is stable at 523, 581, and 573 K (250, 308 and 300 °C), respectively (Fig. S13–S15†). The weight reduction between room temperature and 423 K is ascribed to the loss of solvents ($MeOH/H_2O$) in the pores of ZNU-2-M.

Encouraged by the ultrahigh stability of ZNU-2-M, we are interested in investigating their permanent porosity as well as unary gas adsorption difference between C_3H_4 and C_3H_6. At first, N_2 gas adsorption experiments at 77 K were conducted (Fig. S16–S19†), which indicated their microporous character with pore size distribution in the range of 6.27–9.84 Å, 6.56–9.40 Å, and 7.85–9.40 Å, respectively, very close to the pore aperture of ~8.5 Å calculated from the single crystal structure. The BET surface areas and pore volumes are 1339/1380/1281 $m^2\ g^{-1}$ and 0.565/0.575/0.521 $cm^3\ g^{-1}$, for ZNU-2-Si, ZNU-2-Ti and ZNU-2-Nb respectively. These BET surface areas are all superior to the benchmark of SIFSIX-1-Cu (1128 $m^2\ g^{-1}$) in pillar-layer APMOFs.[14]

Single-component C_3H_4 adsorption isotherms were then collected at 298 K (Fig. 2a). At 1 bar, the C_3H_4 uptakes were 188, 171 and 162 $cm^3\ g^{-1}$ for ZNU-2-Si, ZNU-2-Ti and ZNU-2-Nb, corresponding to 4.52, 4.25, and 4.34 C_3H_4 molecules adsorbed per anion (Fig. 2b). Such a high C_3H_4/anion ratio means every free F site can bind 1.13, 1.06, and 1.09 C_3H_4 molecules, much higher than those of SIFSIX-2-Cu-i (2.57), TIFSIX-14-Cu-i (2.31), ZU-62 (2.30) and SIFSIX-3-Ni (1.09) (Fig. 2b). The adsorption capacities under 0.01 and 0.1 bar were further compared with those of other MOFs (Fig. 2c). The C_3H_4 uptake of ZNU-2-Si at 0.01 bar is record high at 106 $cm^3\ g^{-1}$. This uptake is even much higher than the saturated capacities (1 bar) of most MOFs, such as ELM-12 (61.4 $cm^3\ g^{-1}$),[19] SIFSIX-3-Ni

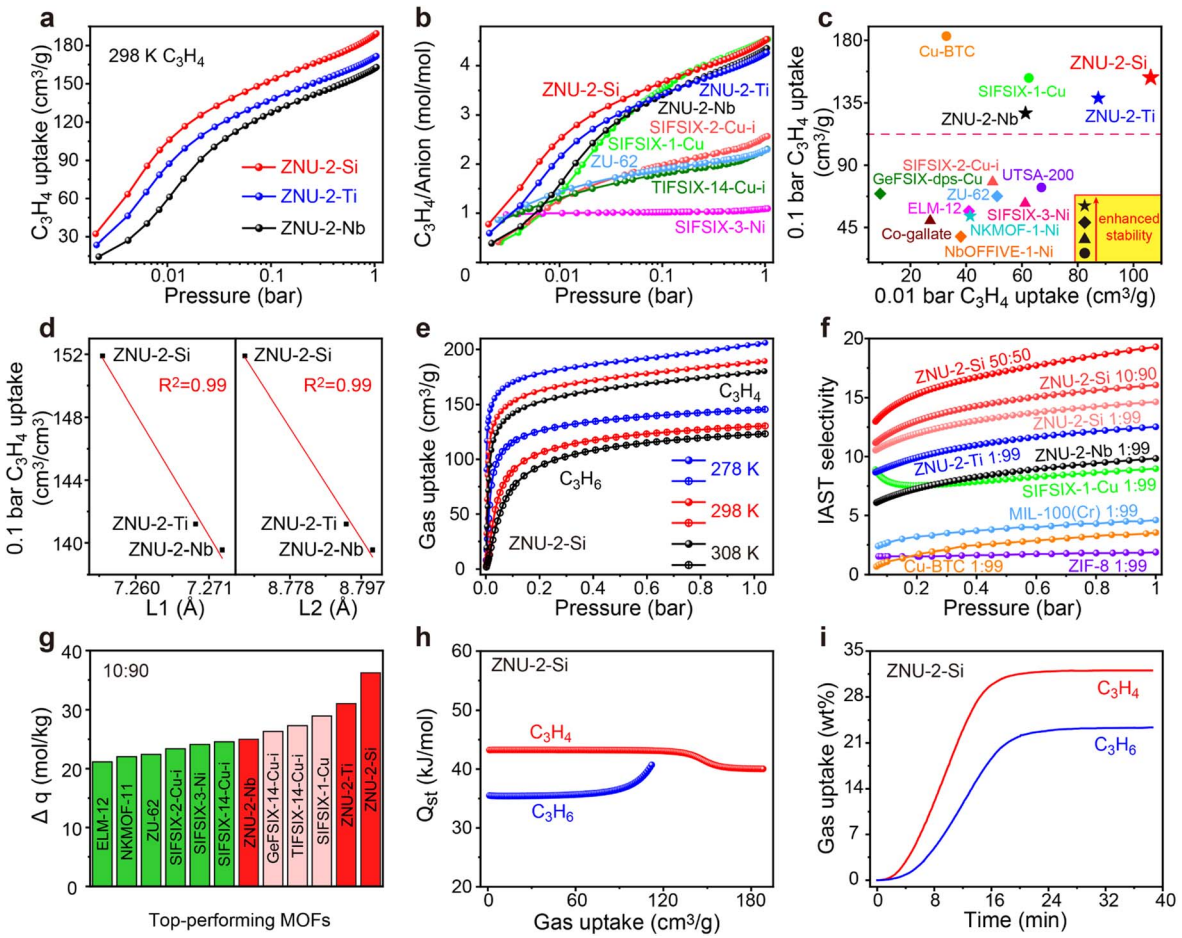

Fig. 2 (a) C_3H_4 adsorption isotherms in the ZNU-2 family at 298 K. (b) Comparison of the C_3H_4 adsorption isotherms of the ZNU-2 family with fluorinated anion hybrid microporous materials. (c) Comparison of the low pressure C_3H_4 uptake and stability among top-performing MOFs. (d) Plot of C_3H_4 uptake at 0.1 bar *vs.* N···N distance (L1)/Cu···Cu distance (L2). (e) C_3H_4 and C_3H_6 adsorption isotherms for ZNU-2-Si at 278, 298 and 308 K. (f) Comparison of IAST selectivity of the ZNU-2 family with other MOFs showing high C_3H_4 capacity (>100 $cm^3\ g^{-1}$). (g) Comparison of ZNU-2's IAST based separation potential ($\Delta q = C_3H_4$ uptake $\times\ 9 - C_3H_6$ uptake) for C_3H_4/C_3H_6 (10/90) mixtures with reported top performing MOFs. (h) The isosteric heat of adsorption, Q_{st}, for C_3H_4 and C_3H_6 in ZNU-2-Si. (i) Adsorption kinetic curves of C_3H_4 and C_3H_6 in ZNU-2-Si.

(66.8 $cm^3\ g^{-1}$),[14] NKMOF-11 (69.4 $cm^3\ g^{-1}$),[20] GeFSIX-14-Cu-i (75.3 $cm^3\ g^{-1}$),[17] Ca-based MOF (67.4 $cm^3\ g^{-1}$),[25] UTSA-200 (81.1 $cm^3\ g^{-1}$),[15] ZU-62 (82.0 $cm^3\ g^{-1}$)[18] and TIFSIX-14-Cu-i (86.5 $cm^3\ g^{-1}$).[17] Interestingly, a good negative linear relationship between the C_3H_4 uptakes under low pressure (0.1 bar) and the N···N/Cu···Cu distances is observed (Fig. 2d). Such a structure–capacity relationship has never been reported before. Then C_3H_4 and C_3H_6 adsorption isotherms on ZNU-2-M at 278, 298 and 308 K were all collected (Fig. 2e). The C_3H_6 adsorption capacities are much lower than those of C_3H_4, especially in low pressure regions. The C_3H_4/C_3H_6 selectivity on ZNU-2 at 298 K was calculated by using Ideal Adsorbed Solution Theory (IAST). As shown in Fig. 2f, the selectivity of ZNU-2-Si for 1/99 C_3H_4/C_3H_6 is 14.64, which is higher than that of ZNU-2-Ti (12.53), ZNU-2-Nb (9.84), ZIF-8 (1.9),[15] FJI-W1 (2.2),[26] Cu-BTC (3.2),[15] MIL-100(Cr) (4.5),[15] and SIFSIX-1-Cu (9.0)[14] (Fig. 2f). The increased ratio of C_3H_4 in the gas mixture results in increased C_3H_4/C_3H_6 selectivity, which is 16.05 and 19.29 for 10/90 and 50/50 C_3H_4/C_3H_6 mixtures, respectively. The simultaneous increase of the C_3H_4/C_3H_6 selectivity along the uptakes or C_3H_4 ratios suggests the existence of cooperative interactions inside ZNU-2-Si.

The static C_3H_4 and C_3H_6 uptakes from the 10/90 mixture of C_3H_4/C_3H_6 were calculated for the ZNU-2 family and other leading materials (Fig. S30, S35, S40 and S42–S48†). The separation potential ($\Delta q = q_1y_2/y_1 - q_2$)[31] as a combined metric of both selectivity and capacity was utilized here for further comparison, which showed a trend of ZNU-2-Si (36.2 mol kg^{-1}) > ZNU-2-Ti (31.0 mol kg^{-1}) > SIFSIX-1-Cu (29.0 mol kg^{-1})[14] > TIFSIX-14-Cu-i (27.3 mol kg^{-1})[17] > GeFSIX-14-Cu-i (26.3 mol kg^{-1})[17] > ZNU-2-Nb (25.0 mol kg^{-1}) > SIFSIX-14-Cu-i (24.6 mol kg^{-1}) > SIFSIX-3-Ni (24.1 mol kg^{-1})[14] > SIFSIX-2-Cu-i (23.4 mol kg^{-1})[14] > ZU-62 (22.4 mol kg^{-1})[18] > NKMOF-11 (22.0 mol kg^{-1})[20] > ELM-12 (21.2 mol kg^{-1})[19] at 1 bar and 298 K (Fig. 2g). The isosteric enthalpies of adsorption (Q_{st}) for ZNU-2-M were then calculated with the Clausius–Clapeyron equation. Q_{st} values at near-zero loading for C_3H_4 and C_3H_6 were 43.2/43.0/41.6 and 35.5/34.5/32.4 kJ mol^{-1}, respectively (Fig. 2h, S28, S33 and S38†). The Q_{st} values for C_3H_4 in the ZNU-2 family are lower than those of most MOFs for C_3H_4/C_3H_6 separation such as ZU-62 (71.0 kJ mol^{-1}),[25] SIFSIX-3-Ni (68.0 kJ mol^{-1}),[14] NKMOF-1-Ni (65.1 kJ mol^{-1}),[25] Ca-based MOF (55.4 kJ mol^{-1}),[25] UTSA-200 (55.3 kJ mol^{-1}),[15] ELM-12 (60.6 kJ mol^{-1})[19] and SIFSIX-2-Cu-i (46.0 kJ mol^{-1}),[14] but slightly higher than that of SIFSIX-1-Cu (37.2 kJ mol^{-1})[14] (Table S18†). Such modestly high Q_{st} not only facilitates preferential C_3H_4 adsorption, but also allows the facile recovery of C_3H_4 by desorption under mild conditions. To further compare the adsorption difference of C_3H_4 and C_3H_6 on ZNU-2-Si, we studied the kinetic adsorption behavior. The adsorption rate of C_3H_4 in ZNU-2-Si is faster than that of C_3H_6. This means that the intra-crystalline diffusion of C_3H_4 is faster than that of C_3H_6 (Fig. 2i). To the best of our knowledge, such kinetic difference has not been reported in pillar-layered APMOFs for C_3H_4/C_3H_6 separations. Besides, adsorption thermodynamics and diffusion are usually anti-synergistic as stronger adsorption often implies reduced mobility.[32] Therefore, ZNU-2-Si with thermodynamic–kinetic synergism is highly promising to provide benchmark practical C_3H_4/C_3H_6 separation performance.

To obtain direct host–guest interaction information between ZNU-2-Si and adsorbed gases, we introduced C_3H_4 and C_3H_6 into the desolvated ZNU-2-Si and measured it in the single crystal X-ray diffractometer. Due to the high stability of ZNU-2-Si, the C_3H_4 and C_3H_6 loaded structures are ambiguously resolved (Fig. 3 and S10†). 24 C_3H_4 molecules and 18 C_3H_6 molecules are adsorbed per cell, equal to 4 C_3H_4 and 3 C_3H_6 molecules for every SIFSIX anion, consistent with the experimental results. After adsorption, the framework remained in the same cubic $Pm\bar{3}n$ space group with negligible bond or angle changes (Table S2†). From the *in situ* crystals, C_3H_4 showed disorder into two overlapping configurations. The configuration with the alkynyl C–H end closer to SiF_6^{2-} is chosen to be discussed in the following text. The hydrogen bond distances between the terminal C_3H_4 hydrogen and F atom of SiF_6^{2-} are all 2.576 Å. Interestingly, no single C_3H_4 molecule is completely loaded in the narrow interlaced single molecule channel, which was previously considered as the best energy favored single molecule binding site.[27] Instead, four C_3H_4 molecules are equally close to the interlaced channel while their alkynyl C–H ends are inside (Fig. 3b). On the other hand, all C_3H_4 molecules can be considered to locate in the large cage with their C–H end reaching outside (Fig. 3c). Therefore, every

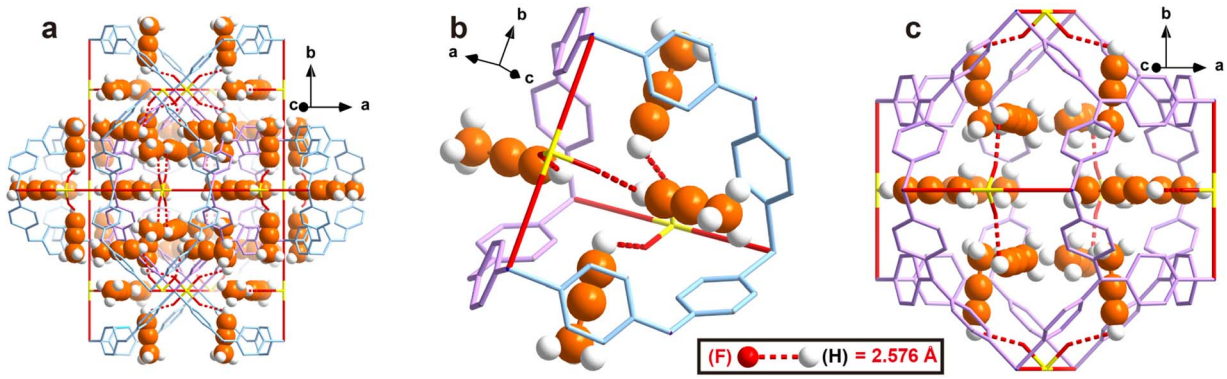

Fig. 3 Single crystal structure of C_3H_4 loaded ZNU-2-Si. (a) A holistic view. (b) View around the interlaced channel. (c) View around the cage.

large cage can accommodate 12 C_3H_4 molecules. The C_3H_6 adsorption sites are very close to that for C_3H_4. Due to the high symmetry, every free F atom is able to bind 0.75 C_3H_6 molecules (Fig. S10†). Strangely, the hydrogen bond distance (2.108 Å) between terminal $=CH_2$ and the F atom is even shorter than the $\equiv$C–H···F distance. Thus, DFT calculations are applied to directly compare their binding energies, which will be discussed in the next part.

The structure of ZNU-2-Si with less C_3H_4 loading is also obtained by controlling the adsorption pressure at 0.01 bar. However, due to the ultrahigh adsorption uptake of C_3H_4 under low pressure, there is still a large amount of C_3H_4 observed in the cage of ZNU-2-Si and the binding sites are the same. The only difference is the occupancy of every C_3H_4 molecule is only *ca.* 50%, equal to 6 C_3H_4 molecules in every cage. Such uptake is close to the experimental adsorption capacity (106 $cm^3\ g^{-1}$) under 0.01 bar.

In most of the literature, bond length is used to compare the interaction strength. However, in our case, the $\equiv$C–H···F distance (2.576 Å) is longer than the $=$CH···F distance (2.108 Å), making it difficult to judge which interaction is stronger as the acidity of the $\equiv$C–H hydrogen is stronger than that of $=CH_2$. Thus, crystallography based DFT calculation is applied to calculate the bonding energy. First of all, we calculate the bonding energy between the framework and single gas molecule. To our delight, the results indicated the binding energy between a single C_3H_4 molecule and ZNU-2-Si is −39.35 kJ mol^{-1} (Fig. 4a) while that for C_3H_6 is only −34.26 kJ mol^{-1} (Fig. 4b), indicating the interaction between C_3H_4 and ZNU-2-Si is stronger. The binding energy difference (5.09 kJ mol^{-1}) is also close to the experimental Q_{st} difference (7.7 kJ mol^{-1}).

The binding energies of ZNU-2-Si and six gas molecules were also calculated, which are −42.57 and −36.93 kJ mol^{-1} for C_3H_4 and C_3H_6 (Fig. 4c and d), respectively. These binding energies can be separated into two parts: ZNU-2-Si···gas (host–guest) interaction energy and gas···gas (guest–guest) interaction energy. For C_3H_4, the ZNU-2-Si···C_3H_4 binding energy is still −39.35 kJ mol^{-1} and the interaction energy of six C_3H_4···C_3H_4 molecules is −3.22 kJ mol^{-1} (Fig. 4c). For C_3H_6, the ZNU-2-Si···C_3H_6 binding energy is −34.27 kJ mol^{-1} and the interaction energy of six C_3H_6···C_3H_6 molecules is −2.66 kJ mol^{-1} (Fig. 4d). These results indicated that the C_3H_4···C_3H_4 interactions are stronger than C_3H_6···C_3H_6 interactions in the confined cavity while the ZNU-2-Si···gas molecules remained nearly unchanged with the loading increase.

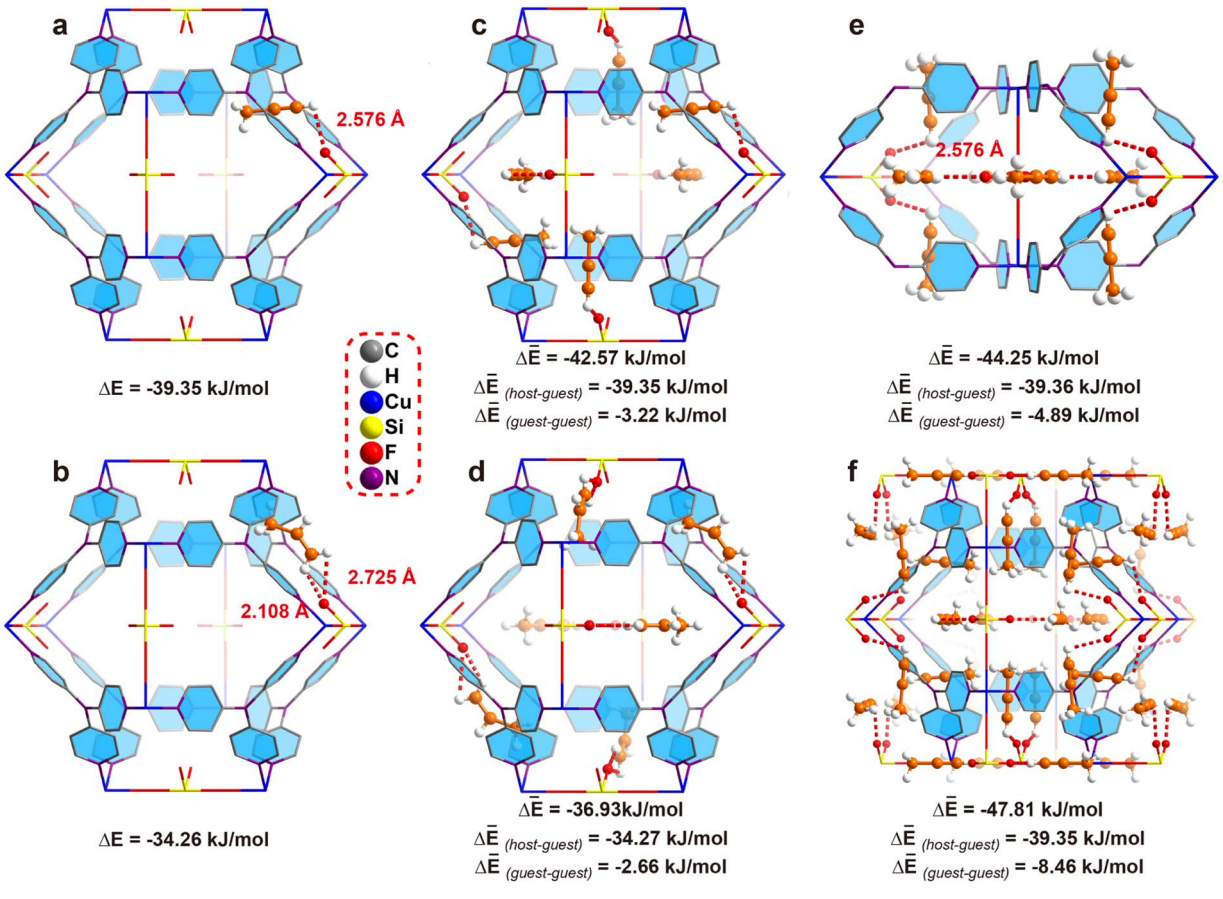

Fig. 4 The DFT-D calculated interaction energy of ZNU-2-Si and gas molecules under different loadings based on the single crystal structure. (a and b) A C_3H_4 or C_3H_6 molecule located in a cage. (c and d) Six C_3H_4 or C_3H_6 molecules located in a cage. (e) 8 C_3H_4 molecules located near two neighbouring interlaced channels. (f) 24 C_3H_4 molecules in a unit cell.

To gain more insight into the $C_3H_4\cdots C_3H_4$ cluster, we choose another two models with different C_3H_4 molecules for comparison. Fig. 4e displays the structure of 8 C_3H_4 molecules in two neighboring interlaced channels, where the $C_3H_4\cdots C_3H_4$ interaction energies increased to -4.89 kJ mol^{-1}. Fig. 4f displays the complete loading of C_3H_4 molecules in the cages (*i.e.* 24 C_3H_4 molecules in a unit cell), where the $C_3H_4\cdots C_3H_4$ interaction energies are further increased to -8.46 kJ mol^{-1}. These results unambiguously revealed the boosted C_3H_4 adsorption behavior in ZNU-2-Si through cooperative guest⋯guest interactions.

To gain more insight into the gas adsorption behavior, GCMC simulations were performed, which indicated two distinct binding sites: one located completely in the interlaced channel and the other completely inside the cage. Moreover, the results indicated that 30 C_3H_4 molecules can be adsorbed in a single unit cell at 298 K and 1 bar (Fig. S68†), equal to 209 cm^3 g^{-1} for ZNU-2-Si, similar to the experimental value of 188 cm^3 g^{-1}. DFT calculations were then applied to identify the adsorption configuration and binding energies of C_3H_4 in ZNU-2-Si. Fig. 5a shows that the C_3H_4 molecule in the first binding site is completely in the interlaced channel. The three hydrogen atoms from the methyl group in C_3H_4 strongly interact with three F atoms at the sharing edges of four different cages. The hydrogen bond distances are 2.24, 2.73, 2.86 and 2.89 Å. Besides, multiple additional weak van der Waals interactions exist with the C⋯H distances of 2.68, 2.77 and 2.85 Å (Fig. S56†). All of these interactions contribute to a high binding energy of -55.31 kJ mol^{-1}. The second binding site located inside the cage adsorbs C_3H_4 by two strong hydrogen bonds between the terminal hydrogen of C_3H_4 and two adjacent F atoms with distances of 2.29 and 2.31 Å (Fig. 5b). This binding energy is -42.87 kJ mol^{-1}. The binding energy for the second C_3H_4 molecule inside the cage increases to -46.45 kJ mol^{-1}. Thus, the average binding energy of two C_3H_4 molecules inside the cavity is -44.66 kJ mol^{-1}. In addition, the binding energies increase to -48.98, -49.72, and -50.55 kJ mol^{-1} for accommodation of 6, 10 and 13 C_3H_4 molecules in a cage, respectively (Fig. 5c–f). To provide direct comparison, the GCMC simulation result with 24 C_3H_4 molecules located both in the narrow channel and the large cage was chosen as a model for optimization. DFT calculation indicated the average bonding energy is -50.85 kJ mol^{-1} (Fig. S69a†), which is still higher than that (-47.81 kJ mol^{-1}) based on the single crystal structure. Moreover, the GCMC optimized C_3H_4 configurations (*i.e.* 6 C_3H_4 molecules completely in the 6 narrow channels and 18 C_3H_4 molecules in two large cages) do not display distinct changes under DFT optimization.

As described above, the GCMC based DFT calculation obviously provided more energy favorable binding sites for C_3H_4 molecules compared to those based on the single crystal structure. Then why do C_3H_4 molecules not follow this pathway for accommodation? Analysis of the cage-channel structure indicates that the narrow interlaced channel is the only passage that connects cages. Gas molecules in cage I must pass through the intersection to reach cage II. Thus, once the intersection is

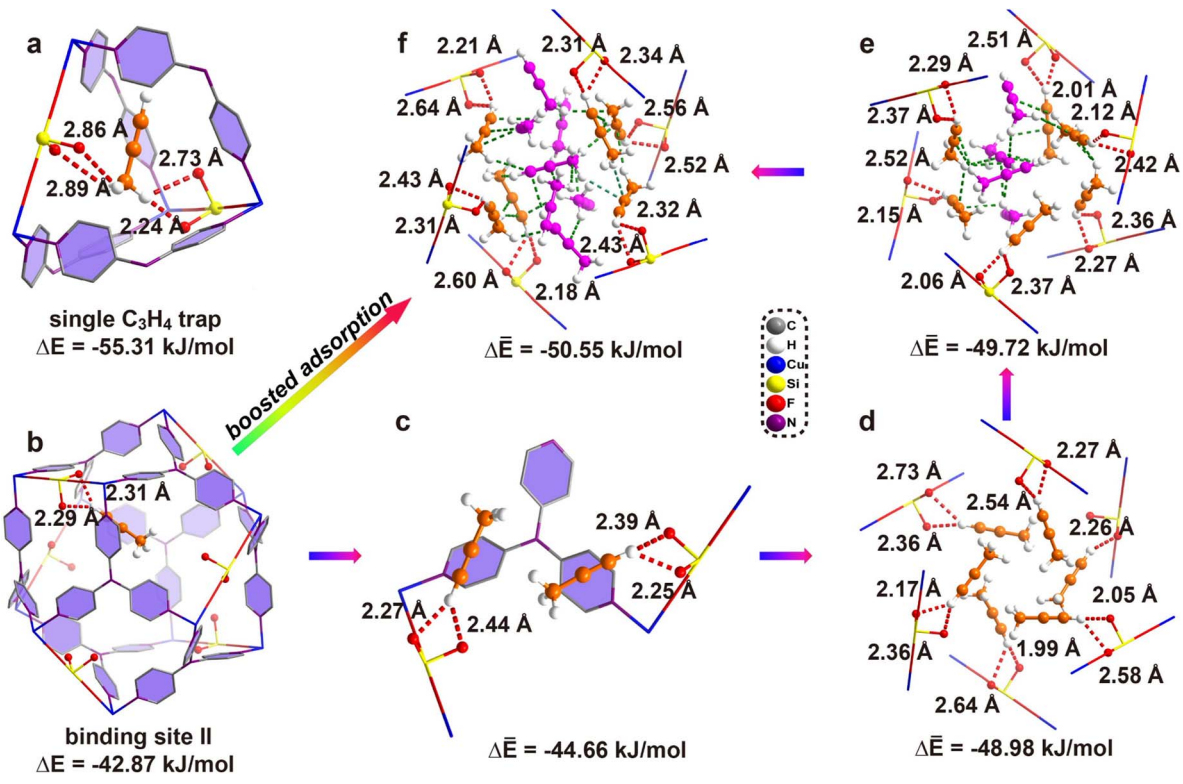

Fig. 5 The DFT-D optimized C_3H_4 adsorption configuration based on GCMC simulation and bonding energy of C_3H_4 in ZNU-2-Si. (a) Binding site I inside the interlaced channel. (b) Binding site II inside the cage. (c–f) 2, 6, 10, and 13 C_3H_4 molecules adsorbed inside the cage.

occupied, the diffusion is limited. Moreover, the entropy of C_3H_4 in the interlaced channel is the lowest because the rotation is highly restricted in the narrow channel. The diffusion of C_3H_4 from the intersection to the large cages is entropy favorable. Therefore, the experimentally observed C_3H_4 binding configuration is an entropy–enthalpy balanced result. As GCMC simulations neglect the influence of diffusion or entropy effect, they may not reflect the real binding sites in biporous materials.[33] Binding site I (Fig. 5a) can be the exact location for the adsorption of the first C_3H_4 molecule under extremely low pressure. Once the pressure or number of C_3H_4 molecules increases, the diffusion or entropy effect becomes obvious, and the symmetrical binding sites in Fig. 4 to provide higher entropy are favored. On the other hand, the final C_3H_4 adsorption configuration can be considered as the result of competitive adsorption of C_3H_4 from different cages. Due to the high symmetry of the framework, four C_3H_4 molecules in the neighbouring large cages show the same potential to enter the interlaced channel to be strongly trapped but this narrow channel can only accommodate a single C_3H_4 completely. Thus, four C_3H_4 molecules squeeze their smaller ≡C–H ends into the interlaced channel but leave their larger ≡C–CH_3 ends outside of the channel. We further calculate the bonding energy between 24 C_3H_4 molecules and ZNU-2-Si based on single crystal structures with all molecules relaxed (Fig. S69b†). In this case, the binding energy of -50.42 kJ mol^{-1} is only slightly inferior to the GCMC result (-50.85 kJ mol^{-1}), which is easy to be covered by the entropy penalty. In brief, GCMC based DFT calculations can provide some information on the initial adsorption while *in situ* single crystal structures give the direct adsorption behavior under the measured conditions.

To gain some insight into the distinct adsorption kinetic difference of C_3H_4 and C_3H_6 in ZNU-2-Si as well as to provide more evidence for the entropy effect, MD simulations were carried out. The configurations of C_3H_4 and C_3H_6 molecules are based on the GCMC simulations and the whole framework is considered flexible except the Cu atoms. Fig. 6a–c illustrate the MSD in the *x*, *y* and *z* directions for 1, 4, and 7 C_3H_4 or C_3H_6 molecules per cage of ZNU-2-Si respectively. These graphs show that within the period of 5000 ps, the C_3H_4 molecules can migrate to other cages through the interlaced channels freely independent of the pressure, namely the number of C_3H_4 molecules located in a cage (Fig. 6d, S70, S71 and S73†). However, the C_3H_6 molecules can only move inside the original cage and are not able to spread to other cages until the number of molecules accommodated in a single cage reaches 5 (Fig. 6e, S70, S72 and S74†). MD-derived C_3H_4 and C_3H_6 diffusion coefficients in ZNU-2-Si were further calculated. The values are $4.72 \times 10^{-11}/6.79 \times 10^{-14}$, $4.89 \times 10^{-11}/4.64 \times 10^{-13}$, and $7.55 \times 10^{-11}/2.50 \times 10^{-11}$ m^2 s^{-1} for 1, 4 and 7 C_3H_4 or C_3H_6 molecules located inside a cage. Therefore, the diffusion coefficient of C_3H_4 is much higher than that of C_3H_6, especially under low pressure with the number of the gas molecules in a cage less than 5 (Table S20†). In other words, the diffusion

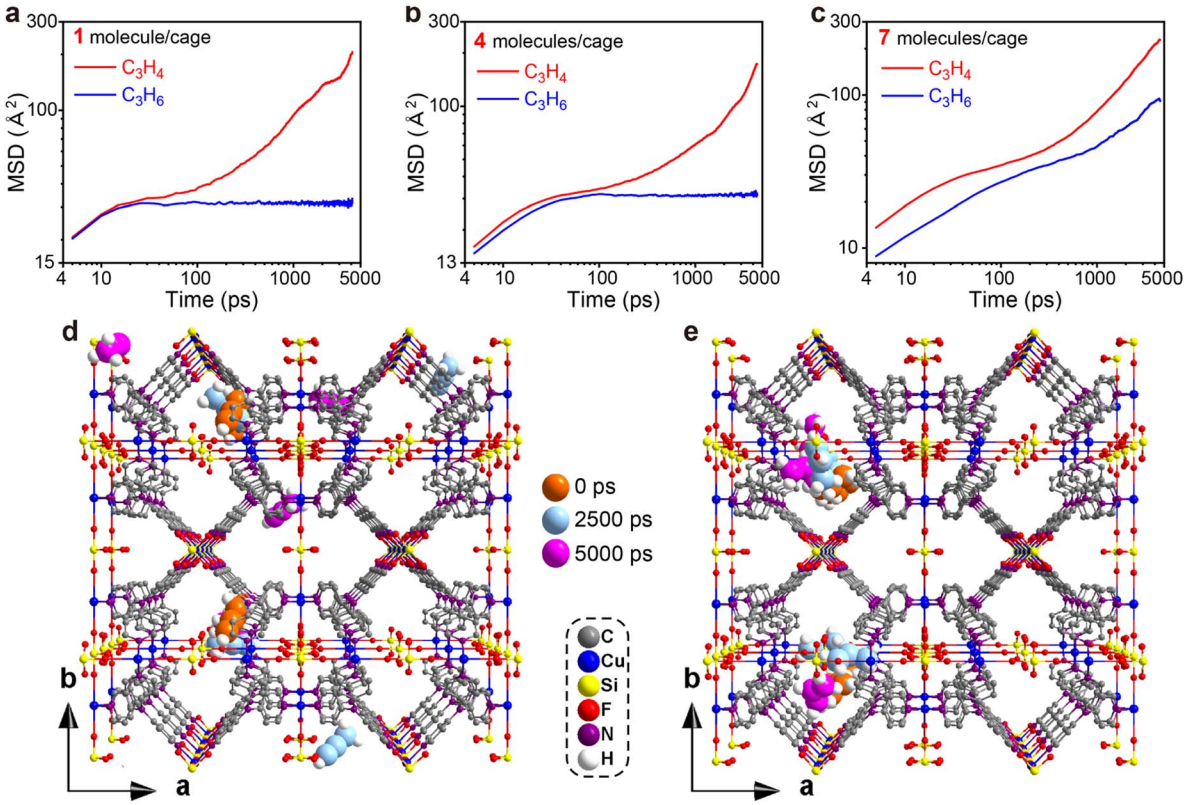

Fig. 6 MD simulations. (a–c) MSD plot of C_3H_4 and C_3H_6 molecules in ZNU-2-Si with 1, 4 and 7 molecules in a single cage. (d and e) Snapshots of MD simulation of C_3H_4 (d) and C_3H_6 (e) molecules at 0, 2500, and 5000 ps.

rate of C_3H_4 in ZNU-2-Si is much faster than that of C_3H_6. The C_3H_4/C_3H_6 kinetic selectivity is as high as ~695 under low pressures and ~3.0 under high pressures. Such high kinetic selectivity has never been found in porous materials for C_3H_4/C_3H_6 separation, which is highly related to its unique framework structure with large cavities and narrow channels. Since the cages are connected by narrow interlaced channels, the gas molecules must pass through the channels when they need to diffuse from one cage to another. As the cross-section of C_3H_6 (4.65×4.16 Å^2) is larger than that of C_3H_4 (4.01×4.16 Å^2), larger pressure is needed to expand the channel sizes (original size ~ 4 Å) by the rotation of the pyridine ring. Therefore, the narrow interlaced channels can be regarded as molecular sieves to allow the C_3H_4 molecules to pass through while prohibiting the migration of the C_3H_6 molecules under certain pressures. Only when the pressure increased to a higher degree did the gate opening (*i.e.* ligand rotation) allow C_3H_6 to diffuse fast within different cages.

We also tried MD simulation considering the framework is completely rigid. In this case, it is very difficult for both C_3H_4 and C_3H_6 molecules to diffuse from one cage to another due to the limitation of the over-contracted intersection (~4 Å). Therefore, the free energies of C_3H_4 and C_3H_6 moving from the narrow channels to the large cages were compared by calculating the potential of mean force (PMF). The results are presented in Fig. S75† which showed that C_3H_4 has a lower free energy barrier than C_3H_6, suggesting the diffusion of C_3H_4 is much easier than C_3H_6.

To evaluate the practical separation performance of ZNU-2-Si for selective C_3H_4/C_3H_6 separation, transient breakthrough simulations were conducted for the 10/90 C_3H_4/C_3H_6 mixture. The results showed that highly efficient separations could be accomplished by ZNU-2-Si (Fig. 7a). The productivity of C_3H_6 (>99.996% purity) in a single adsorption process is also calculated for ZNU-2-Si and other benchmark materials, which showed ZNU-2-Si has the record C_3H_6 productivity of 30.8 mol kg^{-1} (Fig. 7b), consistent with the separation potential Δq_{IAST} based on the static gas adsorption isotherms. Experimental breakthrough studies with the C_3H_4/C_3H_6 (10/90) mixture flowed over a ZNU-2-Si packed column with a flow rate of 4 mL min^{-1} at 298 K were then carried out. The experimental results were superior to the simulated one and 37.8 mol kg^{-1} of high purity C_3H_6 can be produced (Fig. 7c). Such enhancement can be attributed to the existence of the kinetic effect, which has never been reported in C_3H_4/C_3H_6 separation. For isomorphic ZNU-2-Ti, the kinetic enhancement is not obvious. The experimental C_3H_4 productivity (25.50 mol kg^{-1}) is even slightly lower than that of the simulation (25.93 mol kg^{-1}). The difference between ZNU-2-Si and ZNU-2-Ti can be accounted for by the reduced channel aperture in ZNU-2-Si that increases the diffusion difference in C_3H_4/C_3H_6 adsorption.

To thoroughly identify the separation performance of ZNU-2-Si, we conducted more breakthrough experiments under various conditions. C_3H_4/C_3H_6 mixtures containing a higher ratio (50%) or lower ratio (1%) of C_3H_4 were tested. In both cases, clean C_3H_4/C_3H_6 separations were achieved. For the 50 :

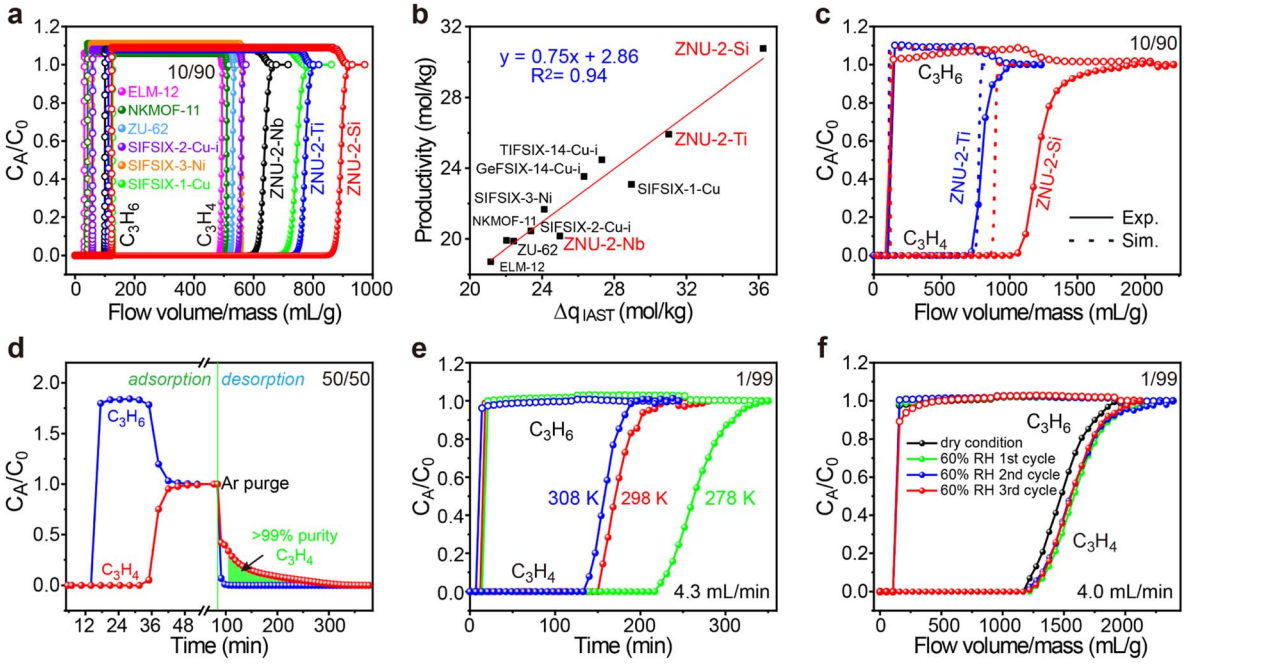

Fig. 7 (a) Simulated breakthrough curves of ZNU-2-Si and other top-performing materials for C_3H_4/C_3H_6 (10/90) at 298 K. (b) Plots of the calculated productivity of C_3H_6 in >99.996% purity and separation potential Δq_{IAST}. (c) Comparison of the experimental and simulated breakthrough curves of ZNU-2-Si and ZNU-2-Ti for C_3H_4/C_3H_6 (10/90). (d) Experimental breakthrough curves and desorption curves of ZNU-2-Si for C_3H_4/C_3H_6 (50/50) at 298 K. (e) Experimental breakthrough curves of ZNU-2-Si for C_3H_4/C_3H_6 (1/99) at 278, 298, and 308 K. (f) Experimental breakthrough curves of ZNU-2-Si for C_3H_4/C_3H_6 (1/99) at 298 K under dry and humid conditions (activation conditions of ZNU-2-Si between cycles: Ar flow rate 20 mL min^{-1} at 393 K).

50 C_3H_4/C_3H_6 mixture, the retention time of C_3H_4 is over twice that of C_3H_6. 7.06 mol kg^{-1} of C_3H_4 was captured in the column with a purity of ~86% (Fig. 7d). Controlling the desorption conditions, 4.7 mol kg^{-1} of >99% purity C_3H_4 can be recovered from the column by evacuation after blowing C_3H_6 out firstly (Fig. 7d and S81†). This record high dynamic productivity of C_3H_4 is impossible to obtain by other APMOFs due to their low C_3H_4 capacity. For the 1 : 99 C_3H_4/C_3H_6 mixture, C_3H_6 broke out at ~18 min and became saturated immediately while C_3H_4 was not detected until ~156 min and reached saturation slowly (Fig. 7e). The calculated experimental productivity of C_3H_6 from the 1 : 99 C_3H_4/C_3H_6 mixture at 298 K is 52.9 mol kg^{-1}, much higher than those of SIFSIX-1-Cu (5.0 mol kg^{-1}), ELM-12 (15.0 mol kg^{-1}), SIFSIX-3-Ni (20.0 mol kg^{-1}), SIFSIX-2-Cu-i (25.5 mol kg^{-1}) and ZNU-2-Ti (42.0 mol kg^{-1}). Upon lowering the experimental temperature to 278 K, the productivity of C_3H_6 increased to 79.20 mol kg^{-1}, exceeding that of UTSA-200 (62.9 mol kg^{-1}, 298 K)[15] and NKMOF-11 (74.4 mol kg^{-1}, 298 K)[20] (Fig. 7e and S79†). Due to its extremely high water stability, we further carried out the breakthrough experiments under humid conditions. The C_3H_4/C_3H_6 (1 : 99) mixture was firstly bubbled into a bottle full of water and then introduced into the column packed with ZNU-2-Si. The humidity was measured constantly, which was stable at ~60% after reaching equilibrium. From the repetitive humidity tests, it can be concluded that the influence of moisture is negligible for C_3H_4/C_3H_6 separation in ZNU-2-Si (Fig. 7f). Finally, the breakthrough experiments were conducted for six cycles, and the excellent separation capacity of ZNU-2-Si was retained, indicating that ZNU-2-Si possesses a high cycling stability (Fig. S84 and S85†). In summary, ZNU-2-Si sets a new record for practical simultaneous C_3H_6 purification and C_3H_4 recovery/storage by the combination of high productivity of polymer grade C_3H_6, large amount recovery of C_3H_4, retention of separation performance under humid conditions, outstanding recycling capacity and facile regeneration conditions.

Conclusions

In conclusion, we reported a chemically stable MOF, ZNU-2-Si, with large three-dimensional pores and narrow interlaced channels for record propyne storage and propyne/propylene separation. Notable features of this work include: (1) benchmark C_3H_4 capacity of 106 cm^3 g^{-1} under a low pressure of 0.01 bar; (2) extremely high C_3H_4 storage capacity (188 cm^3 g^{-1}, 298 K) and storage density (0.60/0.65 g cm^{-3} at 298/278 K) at 1.0 bar; (3) record high C_3H_4/C_3H_6 (10/90) separation potential (36.2 mol kg^{-1}); (4) record high experimental C_3H_6 productivity (37.81 mol kg^{-1}) from 10/90 C_3H_4/C_3H_6 mixtures; (5) record high >99% purity C_3H_4 recovery (4.7 mol kg^{-1}) from a 50/50 C_3H_4/C_3H_6 mixture by a stepped desorption process; (6) benchmark experimental C_3H_6 productivity (52.9/79.2 mol kg^{-1} at 298/278 K) from 1/99 C_3H_4/C_3H_6 mixtures; (7) excellent breakthrough recyclability and performance retention under humid conditions; (8) unprecedented revelation of the adsorption and separation mechanism by *in situ* single crystal analysis and GCMC/MD simulations and DFT calculations. In general, our work not only proposes a strategy of using MOFs with large cages and narrow channels for thermodynamic–kinetic synergistic separation, but also highlights the importance of combining the *in situ* single crystal structure analysis and theoretical studies to investigate the adsorption/separation mechanism. These cage-like APMOFs with optimal pore chemistry and pore structures are supposed to be promising for many other challenging gas separations.

Data availability

All the data supporting this article have been included in the main text and the ESI.†

Author contributions

Y. J.: synthesis, characterization, adsorption experiments, draft preparation; L. W.: single crystal structure measurement and analysis, funding; T. Y.: GCMC simulation, DFT calculation, MD simulation; J. H.: GCMC simulation, DFT calculation; W. S.: breakthrough experiments; R. K.: IAST calculation, breakthrough simulation; D. W.: discussion, advice; Z. G.: PMF calculation; D. L.: supervision of the theoretical study; X. C.: supervision of the theoretical study; H. X.: supervision of the theoretical study; Y. Z.: concept, supervision, draft preparation, funding.

Conflicts of interest

There are no conflicts to declare.

Acknowledgements

This work was supported by the National Natural Science Foundation of China (No. 21908193 and 22205207) and Jinhua Industrial Key Project (2021A22648).

References

1 (*a*) I. Amghizar, L. A. Vandewalle, K. M. Van Geem and G. B. Marin, *Engineering*, 2017, **3**, 171–178; (*b*) M.-Y. Gao, B.-Q. Song, D. Sensharma and M. J. Zaworotko, *SmartMat*, 2021, **2**, 38–55.

2 A. Chavel and G. Lefebvre, *Petrochemical Process*, Institut Francais du Petrole Publications, Gulf Publishing, 1989, pp. 199–208.

3 (*a*) Z. Miao, A. M. Esper, S. S. Nadif, S. A. Gonsales, B. S. Sumerlin and A. S. Veige, *React. Funct. Polym.*, 2021, **169**, 105088; (*b*) J. L. Alterman and G. A. Kraus, *Synthesis*, 2022, **54**, 655–657.

4 (*a*) H. Wang and J. Li, *Acc. Chem. Res.*, 2019, **52**, 1968–1978; (*b*) B. R. Barnett, M. I. Gonzalez and J. R. Long, *Trends Chem.*, 2019, **1**, 159–171; (*c*) X. Zhao, Y. Wang, D. S. Li, X. Bu and P. Feng, *Adv. Mater.*, 2018, **30**, 1705189; (*d*) R.-B. Lin, S. Xiang, W. Zhou and B. Chen, *Chem*, 2020, **6**, 337–363; (*e*) Z. Zhang, S. B. Peh, C. Kang, K. Chai and

D. Zhao, *EnergyChem*, 2021, **3**, 100057; (*f*) S.-Q. Yang and T.-L. Hu, *Coord. Chem. Rev.*, 2022, **468**, 214628.

5 (*a*) Z. Shi, Y. Tao, J. Wu, C. Zhang, H. He, L. Long, Y. Lee, T. Li and Y. Zhang, *J. Am. Chem. Soc.*, 2020, **142**, 2750–2754; (*b*) W. Sun, J. Hu, S. Duttwyler, L. Wang, R. Krishna and Y. Zhang, *Sep. Purif. Technol.*, 2022, **283**, 120220; (*c*) Y. Zhang, X. Cui and H. Xing, *Mater. Chem. Front.*, 2021, **5**, 5970–6013; (*d*) O. T. Qazvini and S. G. Telfer, *ACS Appl. Mater. Interfaces*, 2021, **13**, 12141–12148; (*e*) X.-W. Zhang, D.-D. Zhou and J.-P. Zhang, *Chem*, 2021, **7**, 1006–1019.

6 (*a*) K. Chen, D. G. Madden, T. Pham, K. A. Forrest, A. Kumar, Q. Yang, W. Xue, B. Space, J. J. Perry IV, J. Zhang, X. Chen and M. J. Zaworotko, *Angew. Chem., Int. Ed.*, 2016, **55**, 10268–10272; (*b*) S. Tu, L. Yu, D. Lin, Y. Chen, Y. Wu, X. Zhou, Z. Li and Q. Xia, *ACS Appl. Mater. Interfaces*, 2022, **14**, 4242–4250; (*c*) R. L. Siegelman, P. J. Milner, A. C. Forse, J. Lee, K. A. Colwell, J. B. Neaton, J. A. Reimer, S. C. Weston and J. R. Long, *J. Am. Chem. Soc.*, 2019, **141**, 13171–13186; (*d*) P. Hu, H. Wang, C. Xiong, H. Liu, J. Han, J. Zhou, Z. Zhao, Y. Wang and H. Ji, *ACS Sustainable Chem. Eng.*, 2021, **9**, 15897–15907; (*e*) J. Li, G. L. Smith, Y. Chen, Y. Ma, M. Kippax-Jones, M. Fan, W. Lu, M. D. Frogley, G. Cinque, S. J. Day, S. P. Thompson, Y. Cheng, L. L. Daemen, A. J. Ramirez-Cuesta, M. Schröder and S. Yang, *Angew. Chem., Int. Ed.*, 2022, **61**, 202207259.

7 (*a*) L. Wang, W. Sun, Y. Zhang, N. Xu, R. Krishna, J. Hu, Y. Jiang, Y. He and H. Xing, *Angew. Chem., Int. Ed.*, 2021, **60**, 22865–22870; (*b*) H. Zeng, M. Xie, Y.-L. Huang, Y. Zhao, X.-J. Xie, J. Bai, M.-Y. Wan, R. Krishna, W. Lu and D. Li, *Angew. Chem., Int. Ed.*, 2019, **58**, 8515–8519; (*c*) Z. Niu, X. Cui, T. Pham, G. Verma, P. C. Lan, C. Shan, H. Xing, K. A. Forrest, S. Suepaul, B. Space, A. Nafady, A. M. Al-Enizi and S. Ma, *Angew. Chem., Int. Ed.*, 2021, **60**, 5283–5288; (*d*) J. Wang, Y. Zhang, Y. Su, X. Liu, P. Zhang, R.-B. Lin, S. Chen, Q. Deng, Z. Zeng, S. Deng and B. Chen, *Nat. Commun.*, 2022, **13**, 200; (*e*) W. Sun, J. Hu, Y. Jiang, N. Xu, L. Wang, J. Li, Y. Hu, S. Duttwyler and Y. Zhang, *Chem. Eng. J.*, 2022, **439**, 135745; (*f*) W. Lou, J. Li, W. Sun, Y. Hu, L. Wang, R. F. Neumann, M. Steiner, Z. Gu, B. Luan and Y. Zhang, *Chem. Eng. J.*, 2023, **452**, 139296.

8 (*a*) Y. Zhang, J. Hu, R. Krishna, L. Wang, L. Yang, X. Cui, S. Duttwyler and H. Xing, *Angew. Chem., Int. Ed.*, 2020, **59**, 17664–17669; (*b*) R.-B. Lin, L. Li, H. Wu, H. Arman, B. Li, R.-G. Lin, W. Zhou and B. Chen, *J. Am. Chem. Soc.*, 2017, **139**, 8022–8028; (*c*) W. Fan, S. Yuan, W. Wang, L. Feng, X. Liu, X. Zhang, X. Wang, Z. Kang, F. Dai, D. Yuan, D. Sun and H. Zhou, *J. Am. Chem. Soc.*, 2020, **142**, 8728–8737; (*d*) Q. Dong, Y. Huang, K. Hyeon-deuk, I.-Y. Chang, J. Wan, C. Chen, J. Duan, W. Jin and S. Kitagawa, *Adv. Funct. Mater.*, 2022, **32**, 2203745.

9 (*a*) G.-D. Wang, Y.-Z. Li, W.-J. Shi, L. Hou, Y.-Y. Wang and Z. Zhu, *Angew. Chem., Int. Ed.*, 2022, **61**, e202205427; (*b*) X.-W. Gu, J.-X. Wang, E. Wu, H. Wu, W. Zhou, G. Qian, B. Chen and B. Li, *J. Am. Chem. Soc.*, 2022, **144**, 2614–2623; (*c*) P. Zhang, Y. Zhong, Y. Zhang, Z. Zhu, Y. Liu, Y. Su, J. Chen, S. Chen, Z. Zeng, H. X., S. Deng and J. Wang, *Sci. Adv.*, 2022, **8**, eabn9231; (*d*) L. Yang, L. Yan, W. Niu, Y. Feng, Q. Fu, S. Zhang, Y. Zhang, L. Li, X. Gu, P. Dai, D. Liu, Q. Zheng and X. Zhao, *Angew. Chem., Int. Ed.*, 2022, **61**, e202204046; (*e*) P.-Q. Liao, W.-X. Zhang, J.-P. Zhang and X.-M. Chen, *Nat. Commun.*, 2015, **6**, 8697.

10 (*a*) C. He, R. Krishna, Y. Chen, J. Yang, J. Li and L. Li, *Chin. J. Chem. Eng.*, 2021, **37**, 217–221; (*b*) Y. Chai, X. Han, W. Li, S. Liu, S. Yao, C. Wang, W. Shi, I. Da-Silva, P. Manuel, Y. Cheng, L. D. Daemen, A. J. Ramirez-Cuesta, C. C. Tang, L. Jiang, S. Yang, N. Guan and L. Li, *Science*, 2020, **368**, 1002–1006.

11 (*a*) H. Li, L. Li, R.-B. Lin, W. Zhou, Z. Zhang, S. Xiang and B. Chen, *EnergyChem*, 2019, **1**, 100006; (*b*) K. Adil, Y. Belmabkhout, R. S. Pillai, A. Cadiau, P. M. Bhatt, A. H. Assen, G. Maurin and M. Eddaoudi, *Chem. Soc. Rev.*, 2017, **46**, 3402–3430; (*c*) L. Yang, S. Qian, X. Wang, X. Cui, B. Chen and H. Xing, *Chem. Soc. Rev.*, 2020, **49**, 5359–5406.

12 X. Li, H. Bian, W. Huang, B. Yan, X. Wang and B. Zhu, *Coord. Chem. Rev.*, 2022, **470**, 214714.

13 H.-M. Wen, L. Li, R.-B. Lin, B. Li, B. Hu, W. Zhou, J. Hu and B. Chen, *J. Mater. Chem. A*, 2018, **6**, 6931–6937.

14 L. Yang, X. Cui, Q. Yang, S. Qian, H. Wu, Z. Bao, Z. Zhang, Q. Ren, W. Zhou, B. Chen and H. Xing, *Adv. Mater.*, 2018, **30**, 1705374.

15 L. Li, H. M. Wen, C. He, R. B. Lin, R. Krishna, H. Wu, W. Zhou, J. Li, B. Li and B. Chen, *Angew. Chem., Int. Ed.*, 2018, **57**, 15183–15188.

16 Z. Zhang, Q. Ding, J. Cui, X. Cui and H. Xing, *Small*, 2020, **16**, 2005360.

17 L. Yang, X. Cui, Y. Zhang, Q. Yang and H. Xing, *J. Mater. Chem. A*, 2018, **6**, 24452–24458.

18 L. Yang, X. Cui, Z. Zhang, Q. Yang, Z. Bao, Q. Ren and H. Xing, *Angew. Chem., Int. Ed.*, 2018, **57**, 13145–13149.

19 L. Li, R. B. Lin, R. Krishna, X. Wang, B. Li, H. Wu, J. Li, W. Zhou and B. Chen, *J. Am. Chem. Soc.*, 2017, **139**, 7733–7736.

20 Y.-L. Peng, T. Wang, C. Jin, P. Li, S. Suepaul, G. Beemer, Y. Chen, R. Krishna, P. Cheng, T. Pham, B. Space, M. J. Zaworotko and Z. Zhang, *J. Mater. Chem. A*, 2021, **9**, 2850–2856.

21 Z. T. Lin, Q. Y. Liu, L. Yang, C. T. He, L. Li and Y. L. Wang, *Inorg. Chem.*, 2020, **59**, 4030–4036.

22 Y. L. Peng, C. He, T. Pham, T. Wang, P. Li, R. Krishna, K. A. Forrest, A. Hogan, S. Suepaul, B. Space, M. Fang, Y. Chen, M. J. Zaworotko, J. Li, L. Li, Z. Zhang, P. Cheng and B. Chen, *Angew. Chem., Int. Ed.*, 2019, **58**, 10209–10214.

23 T. Ke, Q. Wang, J. Shen, J. Zhou, Z. Bao, Q. Yang and Q. Ren, *Angew. Chem., Int. Ed.*, 2020, **59**, 12725–12730.

24 Z. Li, L. Li, L. Guo, J. Wang, Q. Yang, Z. Zhang, Y. Yang, Z. Bao and Q. Ren, *Ind. Eng. Chem. Res.*, 2020, **59**, 13716–13723.

25 L. Li, L. Guo, F. Zheng, Z. Zhang, Q. Yang, Y. Yang, Q. Ren and Z. Bao, *ACS Appl. Mater. Interfaces*, 2020, **12**, 17147–17154.

26 S. Zou, Z. Di, H. Li, Y. Liu, Z. Ji, H. Li, C. Chen, M. Wu and M. Hong, *Inorg. Chem.*, 2022, **61**, 7530–7536.

27 Y. Jiang, J. Hu, L. Wang, W. Sun, N. Xu, R. Krishna, S. Duttwyler, X. Cui, H. Xing and Y. Zhang, *Angew. Chem., Int. Ed.*, 2022, **61**, e202200947.
28 (*a*) D. O'Nolan, A. Kumar and M. J. Zaworotko, *J. Am. Chem. Soc.*, 2017, **139**, 8508–8513; (*b*) S. Noro, R. Kitaura, M. Kondo, S. Kitagawa, T. Ishii, H. Matsuzaka and M. Yamashita, *J. Am. Chem. Soc.*, 2002, **124**, 2568–2583.
29 H. Li, C. Liu, C. Chen, Z. Di, D. Yuan, J. Pang, W. Wei, M. Wu and M. Hong, *Angew. Chem., Int. Ed.*, 2021, **60**, 7547–7552.
30 M. Lusi, P. B. A. Fechine, K.-J. Chen, J. J. Perry IV and M. J. Zaworotko, *Chem. Commun.*, 2016, **52**, 4160–4162.
31 (*a*) R. Krishna, *RSC Adv.*, 2017, **7**, 35724–35737; (*b*) R. Krishna, *ACS Omega*, 2020, **5**, 16987–17004.
32 R. Krishna and J. M. van Baten, *ACS Omega*, 2022, **7**, 13050–13056.
33 M. Xie, Z. Lu, W. Lu and D. Li, *Inorg. Chem. Front.*, 2022, **9**, 2697–2705.

Supporting information

Insights into thermodynamic-kinetic synergistic separation of propyne/propylene in anion pillared cage MOFs with entropy-enthalpy balanced adsorption sites

Yunjia Jiang,[§a] Lingyao Wang,[§a] Tongan Yan,[§b] Jianbo Hu,[§c] Wanqi Sun,[a] Rajamani Krishna,[d] Dongmei Wang,[a] Zonglin Gu,[e] Dahuan Liu,[b] Xili Cui,[c] Huabin Xing[c] and Yuanbin Zhang*[a]

[§] These authors contributed equally to this work

[a] Key Laboratory of the Ministry of Education for Advanced Catalysis Materials, College of Chemistry and Life Sciences, Zhejiang Normal University, Jinhua 321004, China. E-mail: ybzhang@zjnu.edu.cn.

[b] State Key Laboratory of Organic-Inorganic Composites, Beijing University of Chemical Technology, Beijing 100029, China.

[c] Department of Chemistry, Zhejiang University 38 Zheda Road, 310027 Hangzhou, P. R. China.

[d] Van't Hoff Institute for Molecular Sciences, University of Amsterdam, Science Park 904, 1098 XH Amsterdam, Netherlands.

[e] College of Physical Science and Technology, Yangzhou University, Jiangsu, 225009, China.

Table of Contents

I General Information and Procedures

Unless otherwise noted, all the reactions were performed under air without N_2 or Ar protection. All reagents were used as received without purification unless stated otherwise.

Chemicals: Tri(pyridin-4-yl)amine (TPA, 99%) was purchased from Tensus Biotech Company. 4,4'-Bipyridine (98%) and pyrazine (99%) were purchased from Energy Chemical. 1,2-Di(pyridin-4-yl)ethyne (97%) and 1,2-di(pyridin-4-yl)diazene (98%) wee purchased from Chemsoon. The purity of the organic compound was identified by ^{1}H NMR and $^{13}C\{^{1}H\}$ NMR. $Cu[NO_3]_2 \cdot 3H_2O$ (99%), $Ni(BF_4)_2$ (99%) , $(NH_4)_2GeF_6$ (99.99%), $(NH_4)_2SiF_6$ (99.99%) and CuO (99%) were purchased from Energy Chemical. $(NH_4)_2TiF_6$ (98%) was purchased from Alab Chemical. Nb_2O_5 was purchased from Macklin. Aqueous H_2SiF_6 (35%) was purchased from Alfa Aesar. HF (≥ 40%) was purchased from Greagent. C_3H_4 (99.9%), C_3H_6 (99.9%), N_2(99.9999%), He (99.9999%), Ar (99.9999%), C_3H_4/C_3H_6 (50:50), C_3H_4/C_3H_6 (10:90) and C_3H_4/C_3H_6 (1:99) were purchased from Datong Co., Ltd. All other reagents were purchased from Adamas-beta and used without further purification.

Preparation of $CuSiF_6 \cdot 4H_2O$: $CuSiF_6 \cdot 4H_2O$ was prepared according to the reported literature **[1]**. CuO (3.015 g, 38 mmol, 1 eq) and H_2SiF_6 (aq, 35%, 15 mL, 1 eq) were added to a 50 mL Teflon lined stainless autoclave. The mixture was heated at 105 ℃ for 24 h. After that the mixture was cooled to room temperature and a clear blue aqueous $CuSiF_6$ solution was obtained with a small amount of unreacted CuO black solid in the bottom. After removing the solid by filtration, the blue aqueous solution was evaporated at 80 ℃ for more than 5 h in an oil bath, yielding the blue crystalline powder of $CuSiF_6 \cdot 4H_2O$ (7.8 g, 73.0% based on CuO).

Caution! Hydrofluoric acid is toxic and corrosive! It must be handled with extreme caution and the appropriate protective gear.

Preparation of $CuNbOF_5 \cdot 4H_2O$: $CuNbOF_5 \cdot xH_2O$ was prepared according to the reported literature [2]. CuO (1.50 g, 18.9 mmol, 2 eq), Nb_2O_5 (2.51 g, 9.45 mmol, 1 eq) and 4.11 mL HF (aq, 40%, 10 eq) were added to a 50 mL Teflon lined stainless autoclave. The mixture was stirred under the room temperature for 2 h and then was heated at 60 ℃ for 24 h. After that the mixture was cooled to room temperature and a clear blue aqueous $CuNbOF_5$ solution was obtained. After removing the solid by filtration, the blue aqueous solution was evaporated at 80 ℃ for more than 5 h in an oil bath, yielding the blue crystalline powder of $CuNbOF_5 \cdot 4H_2O$ (5.2 g, 81.0% based on CuO).

Preparation of ZNU-2-Nb: To a 5 mL long thin tube was added a 1 mL of aqueous solution with $CuNbOF_5 \cdot 4H_2O$ (~1.8 mg). 2 mL of MeOH/H_2O mixture (v:v=1:1) was slowly layered above the solution, followed by a 1 mL of MeOH solution of TPA (~1.0 mg). The tube was sealed and left undisturbed at 298 K. After ~1 week, purple single crystals were obtained.

Preparation of ZNU-2-Ti: To a 5 mL long thin tube was added a 1 mL of aqueous solution with $Cu(NO_3)_2 \cdot 3H_2O$ (~1.3 mg) and $(NH_4)_2TiF_6$ (~1.0 mg). 2 mL of MeOH/H_2O mixture (v:v=1:1) was slowly layered above the solution, followed by a 1 mL of MeOH solution of TPA (~1.0 mg). The tube was sealed and left undisturbed at 298 K. After ~1 week, purple single crystals were obtained.

Preparation of ZNU-2-Si: To a 5 mL long thin tube was added a 1 mL of aqueous solution with $CuSiF_6 \cdot 4H_2O$ (~1.5 mg). 2 mL of MeOH/H_2O mixture (v:v=1:1) was slowly layered above the solution, followed by a 1 mL of MeOH solution of TPA (~1.0 mg). The tube was sealed and left undisturbed at 298 K. After ~1 week, dark violet single crystals were obtained.

Preparation of gas loaded ZNU-2-Si: The synthesized ZNU-6 was filled into a glass tube and activated at 120 ℃ for 12 h. After the sample cooling down, the C_3H_4 or

C_3H_6 was induced into the sample respectively with Builder SSA 7000 (Beijing) instrument until the pressure reach to 1 bar at 298 K and maintain the state for another hour. Then, the tube was sealed. Finally, the crystals were picked out and covered with the degassed oil, and single crystal X-ray diffraction measurements were carried out at 298 K as soon as possible.

Preparation of SIFSIX-1-Cu: SIFSIX-1-Cu was prepared according to the reported literature [3-5]. 58.3 mg 4,4'-bipyridine (0.37 mmol) was dissolved in 6.5 mL ethylene glycol at 338 K in a 25 mL round bottom flask and an aqueous solution (3 mL) of $CuSiF_6 \cdot 4H_2O$ (51.8 mg, 0.19 mmol) was added to the former solution. The mixture was then heated at 338K for 3 h with stirring. The obtained purple powder was washed with methanol, and soaked in anhydrous MeOH for storage.

Preparation of of SIFSIX-2-Cu-i: SIFSIX-2-Cu-i was prepared according to the reported literature [4-6]. A MeOH solution (4.0 mL) of 1,2-di(pyridin-4-yl)ethyne (~51.5 mg, 0.286 mmol) was mixed with an aqueous solution (4.0 mL) of $CuSiF_6 \cdot 4H_2O$ (~72.2 mg, 0.260 mmol) in a 25 mL round bottom flask and then heated at 358 K for 12 h. The obtained blue powder was washed with methanol, and soaked in anhydrous MeOH for storage. Single crystals of SIFSIX-2-Cu-i was prepared according to the reported literature [6]: To a 5 mL long thin tube was added 2 mL of DMSO solution of 1,2-di(pyridin-4-yl)ethyne (20.7 mg). 2 mL of MeOH solution of $CuSiF_6 \cdot 4H_2O$ (41.4 mg) was slowly layered above the solution. The tube was sealed and left undisturbed at 298 K. After ~1 week, blue single crystals were obtained.

Preparation of ZU-62: ZU-62 was prepared according to the reported literature [2]. A preheated water solution (4.0 mL) of $CuNbOF_5$ (~73.0 mg) was mixed with a preheated methanol solution (4.0 mL) of 1,2-di(pyridin-4-yl)ethyne (~51.5 mg) in a 25 mL round bottom flask. Then the mixture was heated at 353 K for 24 h. The obtained blue powder was washed with methanol, and soaked in anhydrous MeOH for storage. Single crystals of ZU-62 were prepared according to the reported literature

[2]: To a long thin tube was added 3 mL of DMSO solution with 1,2-di(pyridin-4-yl)ethyne (~21.9 mg). 2 mL of DMSO/MeOH mixture (v:v=1:1) was slowly layered above the solution, followed by 3 mL of MeOH solution of $CuNbOF_5$ (~15 mg). The tube was sealed and left undisturbed at 298 K. After ~1 week, blue single crystals were obtained.

Prparation of SIFSIX-3-Ni: SIFSIX-3-Ni was prepared according to the reported literature **[4, 5, 7]**. A methanol solution (20 mL) of $(NH_4)_2SiF_6$ (1 mmol)，$Ni(BF_4)_2$ (1 mmol) and pyrazine (2 mmol) was mixed in a 50 mL round bottom flask, and then heated at 358 K for 3 days. The obtained blue powder was washed with methanol/water, and soaked in anhydrous MeOH for storage.

Preparation of SIFSIX-14-Cu-i: SIFSIX-14-Cu-i was prepared according to the reported literature **[8, 9]**. A methanol solution (3.0 mL) of 1,2-di(pyridin-4-yl) diazene (~49.0 mg) was mixed with an aqueous solution (2.5 mL) of $CuSiF_6$ (~68.6 mg) in a 25 mL round bottom flask. Then the mixture was heated at 353 K for 15 min, additional 1 h at 323 K, and then at 298 K for 24 h resulting in a bright grey precipitate, which was then washed with methanol, and soaked in anhydrous MeOH for storage. Single crystals of SIFSIX-14-Cu-i were prepared according to the reported literature **[8]**: Saffron prism-shaped single crystals of SIFSIX-14-Cu-i/UTSA-200 were synthesized in quantitative yield at room temperature by slow diffusion of a methanol solution of $CuSiF_6$ (2 mL, 0.15 mmol) into a DMSO solution of 1,2-di(pyridin-4-yl)diazene (0.12 mmol) after one week.

Preparation of TIFSIX-14-Cu-i: TIFSIX-14-Cu-i was prepared according to the reported literature **[10]**. A preheated ethanol solution (2.0 mL) of 1,2-di(pyridin-4-yl)diazene (~60.0 mg) was mixed with a preheated glycol solution (3.0 mL) of $Cu(NO_3)_2{\cdot}3H_2O$ (~60.4 mg) and $(NH_4)_2TiF_6$ (~49.5 mg) in a 25 mL round bottom flask. Then the mixture was heated at 338 K for 24 h. The obtained brownish red powder was washed with methanol, and soaked in anhydrous MeOH for storage.

Single crystals of TIFSIX-14-Cu-i were prepared according to the reported literature [10]: To a long thin tube was added 3 mL of DMSO solution with 1,2-di(pyridin-4-yl)diazene (~9 mg). 1 mL of DMSO/ MeOH mixture (v:v=1:1) was slowly layered above the solution, followed by 3 mL of MeOH solution of $Cu(NO_3)_2 \cdot 3H_2O$ (~9.1 mg) and $(NH_4)_2TiF_6$ (~7.5 mg). The tube was sealed and left undisturbed at 298 K. After ~1 week, blue single crystals were obtained.

Preparation of GeFSIX-14-Cu-i: GeFSIX-14-Cu-i was prepared according to the reported literature [11]. A methanol solution (20.0 mL) of 1,2-di(pyridin-4-yl)diazene (~50.3 mg) was mixed with an aqueous solution (25.0 mL) of $Cu(NO_3)_2 \cdot 3H_2O$ (~62.8 mg) and $(NH_4)_2GeF_6$ (~57.9 mg) in a 100 mL round bottom flask. Then the mixture was heated at 298 K for 24 h. The obtained brownish red powder was washed with methanol, and soaked in anhydrous MeOH for storage. Single crystals of GeFSIX-14-Cu-i were prepared according to the reported literature [11]: To a long thin tube was added 3 mL of DMSO solution with 1,2-di(pyridin-4-yl)diazene (~9 mg). 1 mL of DMSO/ MeOH mixture (v:v=1:1) was slowly layered above the solution, followed by 3 mL of MeOH solution of $Cu(NO_3)_2 \cdot 3H_2O$ (~9.1 mg) and $(NH_4)_2GeF_6$ (~8.4 mg). The tube was sealed and left undisturbed at 298 K. After ~2 week, blue single crystals were obtained.

[1] Sun, W. Q. et al. Flexible molecular sieving of C_2H_2 from CO_2 by a new cost-effective metal organic framework with intrinsic hydrogen bonds. *Chem. Eng. J.* **439**, 135745 (2022).

[2] Yang, L. et al. An Asymmetric Anion-Pillared Metal-Organic Framework as a Multisite Adsorbent Enables Simultaneous Removal of Propyne and Propadiene from Propylene. *Angew. Chem. Int. Ed.* **57**, 13145-13149 (2018)..

[3] Noro, S. et al. Framework Engineering by Anions and Porous Functionalities of Cu(II)/4,4'-bpy Coordination Polymers. *J. Am. Chem. Soc.* **124**, 2568-2583 (2002).

[4] Cui, X. et al. Pore chemistry and size control in hybrid porous materials for acetylene capture from ethylene. *Science* **353**, 141-144 (2016).

[5] Yang, L. et al. A Single-Molecule Propyne Trap: Highly Efficient Removal of Propyne from Propylene with Anion-Pillared Ultramicroporous Materials. *Adv. Mater.* **30**, 1705374 (2018).

[6] Nugent, P. et al. Porous materials with optimal adsorption thermodynamics and kinetics for CO_2 separation. *Nature* **495**, 80-84 (2013).

[7] Kumar, A. et al. Direct Air Capture of CO_2 by Physisorbent Materials. *Angew. Chem. Int. Ed.* **54**, 14372-14377 (2015).

[8] Li, B. et al. An Ideal Molecular Sieve for Acetylene Removal from Ethylene with Record Selectivity and Productivity. *Adv. Mater.* **29**, 1704210 (2017).

[9] Li, L. et al. A Metal-Organic Framework with Suitable Pore Size and Specific Functional Sites for the Removal of Trace Propyne from Propylene. *Angew. Chem. Int. Ed.* **57**, 15183-15188 (2018).

[10] Yang, L. et al. A highly sensitive flexible metal–organic framework sets a new benchmark for separating propyne from propylene. *J. Mater. Chem. A* **6**, 24452-24458 (2018).

[11] Zhang, Z. et al. Sorting of C_4 Olefins with Interpenetrated Hybrid Ultramicroporous Materials by Combining Molecular Recognition and Size-Sieving. *Angew. Chem. Int. Ed.* **56**, 16282-16287 (2017).

Single-crystal X-ray diffraction studies were conducted at 293 K、173 K、184 K on the Bruker D8 VENTURE diffractometer equipped with a PHOTON-II detector (MoKα, λ = 0.71073 Å). Indexing was performed using APEX2. Data integration and reduction were completed using SaintPlus 6.01. Absorption correction was performed by the multi-scan method implemented in SADABS. The space group was determined using XPREP implemented in APEX2. The structure was solved with SHELXS-97 (direct methods) and refined on F2 (nonlinear least-squares method) with SHELXL-97 contained in APEX2, WinGX v1.70.01, and OLEX2 v1.1.5 program packages. All non-hydrogen atoms were refined anisotropically. The contribution of disordered solvent molecules was treated as diffuse using the Squeeze routine implemented in Platon.

Powder X-ray diffraction (PXRD) data were collected on the SHIMADZU XRD-6000 diffractometer (Cu Kαλ = 1.540598 Ǻ) with an operating power of 40 KV, 30 mA and a scan speed of 4.0°/min. The range of 2θ was from 5° to 50°.

Thermal gravimetric analysis was performed on the TGA STA449F5 instrument. Experiments were carried out using a platinum pan under nitrogen atmosphere which conducted by a flow rate of 60 mL/min nitrogen gas. First, the samples were heated at 353 K for 2 h to remove the water residue and equilibrated for 5 minutes, then cooled down to 323 K. The data were collected at the temperature range of 323 K to 873 K with a ramp of 10 K /min.

The static gas adsorption equilibrium measurements were performed on the Builder SSA 7000 (Beijing) instrument. Before gas adsorption measurements, the samples of ZNU-2 series (ZNU-2-Nb, ZNU-2-Ti, ZNU-2-Si) (~100 mg) were evacuated at 298 K for 2 h firstly, and then at 393 K for 10 h until the pressure dropped below 7 μmHg. The sorption isotherms were collected at 77, 278, 298 and 308 K on activated samples.The experimental temperatures were controlled by liquid

nitrogen bath (77 K), ethanol-water bath (273 K) and water bath (298 and 308 K), respectively.

Before gas adsorption measurements, the sample of SIFSIX-1-Cu was evacuated at 298 K for 24-48 h until the pressure dropped below 7 μmHg; the sample of SIFSIX-2-Cu-i was evacuated at 353 K for 2 days until the pressure dropped below 7 μmHg; the sample of ZU-62 was evacuated at 353 K for 2 days until the pressure dropped below 7 μmHg; the sample of SIFSIX-3-Ni was evacuated at 353 K for 2 days until the pressure dropped below 7 μmHg; the sample of SIFSIX-14-Cu-i was evacuated at 298 K for 36 h until the pressure dropped below 7 μmHg; the sample of TIFSIX-14-Cu-i was evacuated at 338 K for 24 h until the pressure dropped below 7 μmHg; the sample of GeFSIX-14-Cu-i was evacuated at 298 K for 18 h until the pressure dropped below 7 μmHg. The sorption isotherms were collected at 298 K on activated samples.

The gas adsorption kinetics measurements were performed on the TGA STA449 F5 instrument. Before gas adsorption measurements, the sample of ZNU-2 was activated. After loading the activated ZNU-2-Si (~10 mg) into the pan of the balance (precision: 10^{-7} g), it was firstly heated under N_2 flow (20 mL/min) from 298-423 K with a ramp of 10 K /min. The temperature of 423 K was stayed for 2 hour for the complete removal of moisture adsorbed during the transfer and weighing, which is evidenced by the consistent weight. Then, the sample was cooled to 298 K under N_2 flow (20 mL/min). The temperature of 298 K was stayed for 1 hours. Finally, C_3H_4 or C_3H_6 was introduced with a flow rate of 10 mL/min. The weight was measured constantly.

Fitting of experimental data on pure component isotherms

The unary isotherm data for C_3H_4, and C_3H_6, measured at three different temperatures 278 K, 298 K, and 308 K in ZNU-2 series were fitted with good accuracy using the dual-site Langmuir-Freundlich model, where we distinguish two distinct adsorption sites A and B:

$$q = \frac{q_{sat,A} b_A p^{\nu A}}{1 + b_A p^{\nu A}} + \frac{q_{sat,B} b_B p^{\nu B}}{1 + b_B p^{\nu B}} \quad \text{(S1)}$$

Here, P is the pressure of the bulk gas at equilibrium with the adsorbed phase (Pa), q is the adsorbed amount per mass of adsorbent (mol kg^{-1}), $q_{sat,\,A}$ an $q_{sat,\,B}$ are the saturation capacities of site A and B (mol kg^{-1}), b_A and b_B are the affinity coefficients of site A and B (Pa^{-1}).

In eq (S1), the Langmuir-Freundlich parameters b_A, b_B can be temperature dependent or temperature independent .

$$b_A = b_{A0} \exp\left(\frac{E_A}{RT}\right); \quad b_b = b_{B0} \exp\left(\frac{E_B}{RT}\right) \quad \text{(S2)}$$

In eq (S2), E_A, E_B are the energy parameters associated with sites A, and B, respectively.

The isosteric heat of adsorption, Q_{st}, is defined as

$$Q_{st} = -RT^2 \left(\frac{\partial \ln p}{\partial T}\right)_q \quad \text{(S3)}$$

where the derivative in the right member of eq (S3) is determined at constant adsorbate loading, q. The calculations are based on the use of the Clausius-Clapeyron equation.

IAST calculations of adsorption selectivity and uptake capacities:

We consider the separation of binary 50/50 C_3H_4(1)/C_3H_6(2), 10/90 C_3H_4(1)/C_3H_6(2) and 1/99 C_3H_4(1)/C_3H_6(2) mixtures in various MOFs at 298 K, and varying total pressures.

The adsorption selectivity for separation of binary mixtures of species 1 and 2 is defined by

$$S_{ads} = \frac{q_1 / q_2}{p_1 / p_2} \quad \text{(S4)}$$

where q_1, q_2 are the molar loadings (units: mol kg^{-1}) in the adsorbed phase in equilibrium with a gas mixture with partial pressures p_1, p_2 in the bulk gas.

The $C_3H_4(1)/C_3H_6(2)$ mixture separations are envisaged to be carried out in fixed bed adsorbers. In such devices, the separations are dictated by a combination of adsorption selectivity and uptake capacity. Using the shock wave model for fixed bed adsorbers, Krishna[1, 2] has suggested that the appropriate metric is the separation potential, Δq_2. The appropriate expression describing the productivity of pure C_3H_6 in the desorption phase of fixed-bed operations is

$$\Delta q_2 = q_1 \frac{y_{20}}{y_{10}} - q_2 \qquad \text{(S5)}$$

In eq (S5) y_{10}, y_{20} are the mole fractions of the feed mixture during the adsorption cycle. In the derivation of eq (S5), it is assumed that the concentration "fronts" traversed the column in the form of shock waves during the desorption cycle. The Adsorbed Solution Theory (IAST) of Myers and Prausnitz using the unary isotherm fits as data inputs.[3] The physical significance of Δq_1 is the maximum productivity of pure $C_3H_6(2)$ that is achievable in PSA operations.

Transient breakthrough simulations

The performance of industrial fixed bed adsorbers is dictated by a combination of adsorption selectivity and uptake capacity. Transient breakthrough simulations were carried out for 10/90 and 1/99 $C_3H_4(1)/C_3H_6(2)$ mixtures operating at a total pressure of 100 kPa and 298 K, using the methodology described in earlier publications.[2] In these simulations, intra-crystalline diffusion influences are ignored.

For comparing the separation performance of MOFs, we carried out simulations of transient desorption in which we choose: length of packed bed, L = 0.3 m; superficial gas velocity at the entrance to the bed, $u_0 = 0.04$ m s^{-1}; voidage of the packed bed, ε = 0.4. We choose the mass of the adsorbent in the bed $m_{ads} = 180$ kg,

cross-sectional area, A = 1 m^2; superficial gas velocity at the bed inlet, u_0 = 0.04 m s^{-1}; voidage of the packed bed, ε = 0.4. The interstitial gas velocity $v = \frac{u}{\varepsilon}$. If the total length of the bed is L m, the total volume of the bed is $V_{bed} = LA$. The volume of zeolite or MOF used in the simulations is $V_{ads} = LA(1-\varepsilon)$. It is important to note that the volume of adsorbent, V_{ads}, includes the pore volume of the adsorbent material. If ρ is the framework density, the mass of the adsorbent in the bed is $m_{ads} = (1-\varepsilon)\times(L \text{ m})\times(A \text{ m}^2)\times(\rho \text{ kg m}^{-3})$ kg.

For presenting the breakthrough simulation results, we may use the dimensionless time, $\tau = \frac{tu}{L\varepsilon}$, obtained by dividing the actual time, t, by the characteristic time, $\frac{L}{v} = \frac{\varepsilon L}{u_0}$, where L is the length of adsorber, v is the interstitial gas velocity.

For comparison of breakthrough simulations with breakthrough experiments, it is most convenient to use $\frac{Q_0 t}{m_{ads}}$ as the x-axis when presenting the breakthrough simulation data

$$\frac{(Q_0 = \text{flow rate mL min}^{-1} \text{ at STP})\times(\text{time in min})}{(\text{g MOF packed in tube})} = \frac{Q_0 t}{m_{ads}} = \text{mL g}^{-1} \qquad \text{(S6)}$$

[1] Krishna, R. Screening Metal-Organic Frameworks for Mixture Separations in Fixed-Bed Adsorbers using a Combined Selectivity/Capacity Metric. *RSC Adv*. **7**, 35724−35737 (2017).

[2] Krishna, R. Metrics for Evaluation and Screening of Metal-Organic Frameworks for Applications in Mixture Separations. *ACS Omega* **5**, 16987-17004 (2020).

[3] Myers, A. L. Prausnitz, J. M. Thermodynamics of Mixed Gas Adsorption. *A.I.Ch.E.J*. **11**, 121-130 (1965).

Breakthrough experiments

The breakthrough experiments were carried out in the dynamic gas breakthrough equipment HP-MC41. The experiments were conducted using a stainless steel column (4.6 mm inner diameter × 50 mm length). The weight of ZNU-2-Si and ZNU-2-Ti packed in the columns was 0.49 g and 0.51 g respectively. The column packed with sample was first purged with a Ar flow (5 mL min^{-1}) for 18 h at 393 K. The mixed gas of C_3H_4/C_3H_6 (v/v, 50:50, 10:90, 1:99) was then introduced. Outlet gas from the column was monitored using gas chromatography (GC-9860-5CNJ) with the thermal conductivity detector TCD. After the breakthrough experiment, the sample was regenerated with a Ar purge or under vaccum. All the flowrates are calibrated using self-made soap film flowmeter.

The illustration of the gas breakthrough equipment working mechanism is showing as below: A-B) under work; C) under purge; D) under vacuum.

A) Under Work (dry conditions)

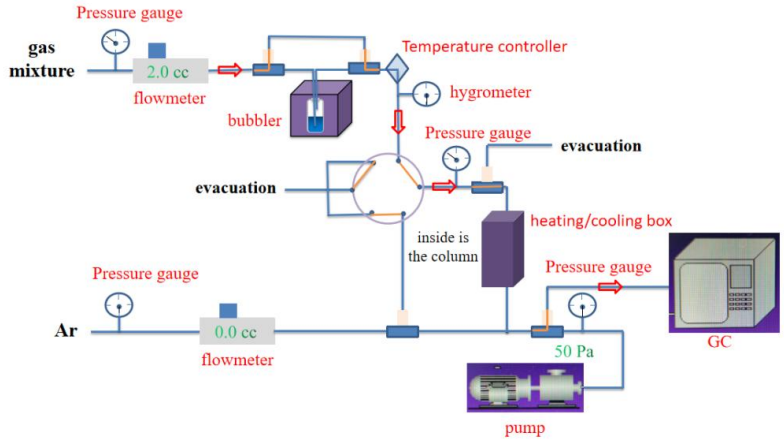

B) Under Work (humid conditions)

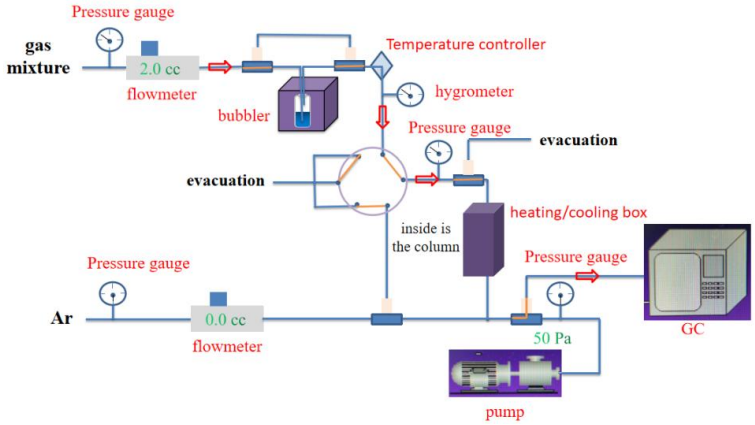

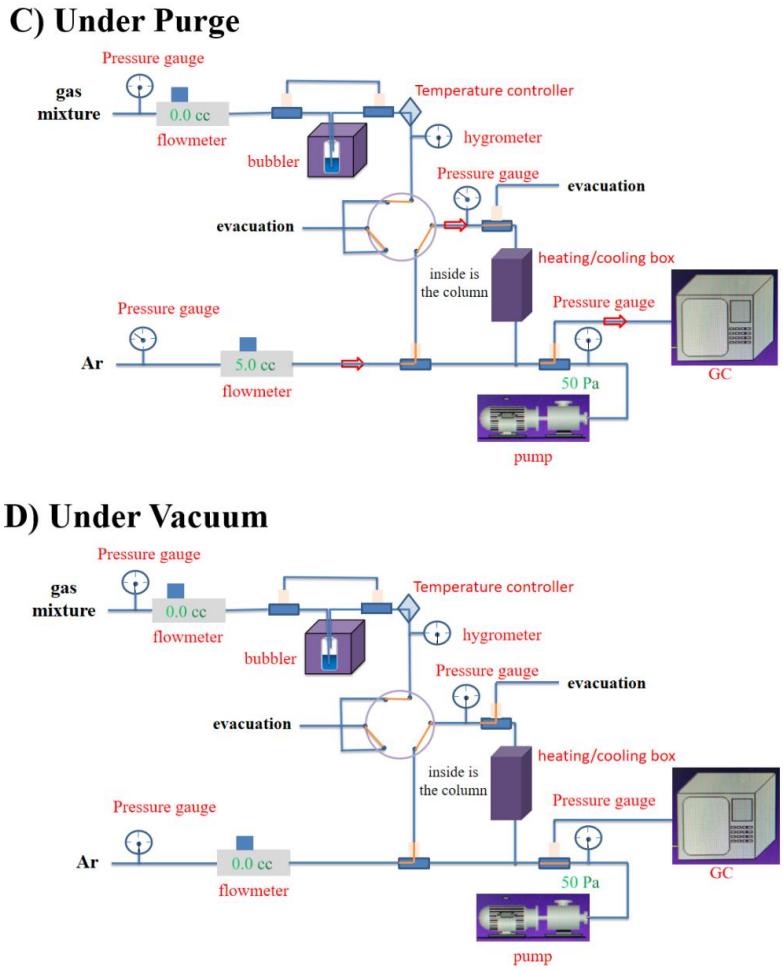

Fig. S1 The illustration of the gas breakthrough equipment working mechanism containing gas pipelines, pressure gauge, flowmeter, hygrometer, GC, bubbler and pump: A) under work in dry conditions; B) under work in humid conditions; C) under purge; D) under vacuum.

Calculation of separation factor (α)

The amount of gas adsorbed i (q_i) is calculated from the breakthrough curve using the following:

$$q_i = \frac{V_T P_i \Delta T}{m}$$

Here, V_T is the total flow rate of gas (cm^3/min), P_i is the partial pressure of gas i (atm), ΔT is the time for initial breakthrough of gas i to occur (mins) and m is the mass of the sorbent (g). The separation factor (α) of the breakthrough experiment is determined as

$$\alpha = \frac{q_1 y_2}{q_2 y_1}$$

Where, y_i is the partial pressure of gas i in the gas mixture.

Molecular simulation

The structures of ZNU-2-Si and ZNU-2-Ti were firstly optimized *via* DFT geometry optimization. The atoms on the framework are assumed to be frozen in their crystallographic positions and the partial point charges of the framework are distributed by QEq method (*Mol. Phys.* **1996**, *87,* 1117–1157). Based on DFT calculations, the ESP charge of the atoms in C_3H_4/C_3H_6 molecules has been calculated. For the framework, the LJ parameters are taken from the UFF force field (*J. Am. Chem. Soc.* **1992**, *114*, 10024–10035). And the LJ parameters for C_3H_4 and C_3H_6 molecules were taken from the optimized OPLS-AA force field by Rego *et. al* (*Fluid Phase Equilibria*, **2022**, *554*, 113314).

Grand canonical Monte Carlo (GCMC) simulations consider four different types of trials: translation, rotation, regrowth, and swap of a molecule adopted the locate task, Metropolis method. During the simulation, the framework was considered to be rigid during the simulations and the interaction energy between the adsorbed molecules and the framework were computed through the Coulomb and Lennard-Jones 12-6 (LJ) potentials. The number of MOF units in the simulation box was 2×2×2 to ensure that the simulation unit was extended, and periodic boundary condition was applied. The cutoff radius was chosen 15.5 Å for Van der Walls interaction and the long-range electrostatic interactions were handled using the Ewald summation method. GCMC simulations of 2×10^7 steps were performed to simulate the favorable adsorption sites and adsorption uptakes at a fixed pressure, with the first 1×10^7 steps used for equilibration and the remaining steps for production. Fugacity was calculated *via* Peng-Robinson equation.

Molecular dynamics (MD) simulations of the canonical ensemble were carried out at 298 K according to the molecular loading results obtained by GCMC simulations,. Each MD was simulated for 5×10^6 steps (i.e., 5 ns) in a time step of 1 fs and then balanced for 5×10^6 steps (i.e., 5 ns). Nosé–Hoover chain (*Mol. Phys.* **1996**, *87,* 1117–1157) thermostat was used to maintain constant temperature conditions, and velocity Verlet algorithm was used to integrate Newton's equation of motion. The framework except Cu atoms is considered flexible during MD simulations. The self-diffusion coefficient can be obtained by averaging 10 independent trajectories. In order to ensure the statistical accuracy of MD simulation, the simulation box was expanded for ZNU-2-Si to increase the number of C_3H_4 and C_3H_6 molecules. From the slope of the mean square displacement (MSD) of the C_3H_4 and C_3H_6, the self-diffusion coefficient of the molecules were calculated. All simulations were performed using Sorption/Forcite module in the Material Studio software version 2017R2.

Potential of mean forces (PMFs) calculation

The PMF values of C_3H_4 and C_3H_6 along the direction from the narrow channel interior to cage-like pores were calculated according to the umbrella sampling approach in Gromacs software package (Figure S74). The framework is considered completely rigid during PMF calculation. The pulling distances (d) to the binding site in channel interior were restrained at a reference distance (d_0) with a harmonic force, $F = k \times (d - d_0)$, where k was the force constant. The spacing of the sampling windows was 0.05 nm. At each d_0, the system was equilibrated for 2 ns, followed by a 10 ns productive run. The free energy profiles were acquired by the g_wham tool that implements the Weighted Histogram Analysis Method.

Density functional theory (DFT) calculations

The static binding energy was calculated using the combination of first principle DFT and plane-wave ultrasoft pseudopotential implemented by CASTEP module in the Materials Studio software version 2017R2. For van der Waals interactions, a semi-empirical addition of dispersive forces was included in the calculation. Calculations were performed under the generalized gradient approximation (GGA) with Perdew–Burke–Ernzerhof (PBE) exchange correlation. A cutoff energy of 520 eV and a 2×2×2 k-point mesh were found to be enough for the total energy to converge within 1×10^{-5} eV $atom^{-1}$. ZNU-2-Si/ZNU-2-Ti crystal structure and an isolated gas molecule in a super cell (with the same cell dimensions as the ZNU-2-Si/ZNU-2-Ti single crystal) were optimized and relaxed. Various guest gas molecules were then introduced to different locations of the channel pore, followed by a full structural relaxation. The equation for the calculation of binding energy (ΔE) is defined as: ΔE = E(MOF) + E(gas) – E(MOF+gas).

II Characterization (SCXRD, PXRD, TGA)

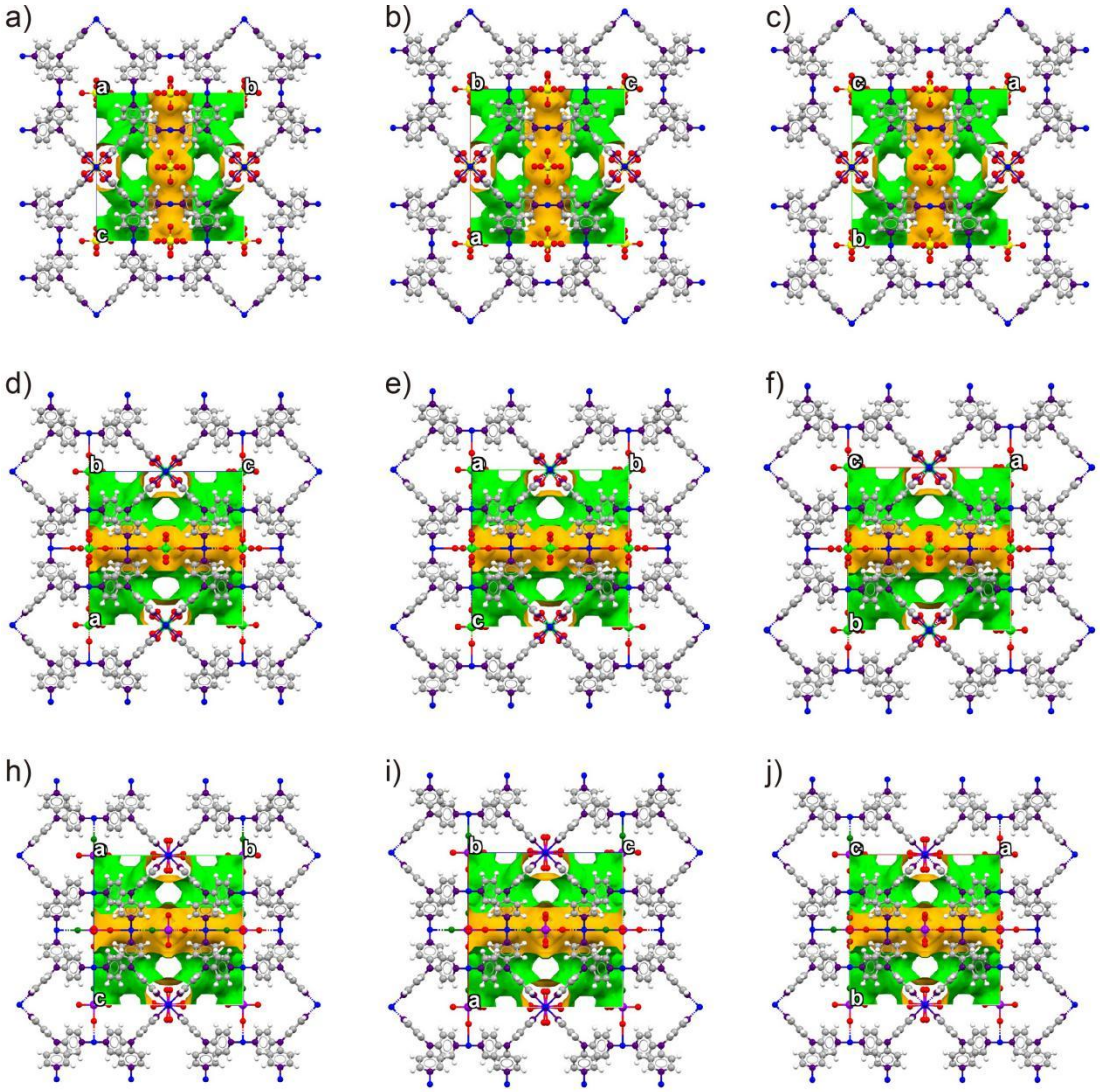

Fig. S2 1 × 1 × 1 packing diagrams of ZNU-2 family viewed down the crystallographic *a*-, *b*-, *c*-axis (a, b, c) in ball-stick mode with pore surface in green representing the inside and yellow the outside determined using a probe with a radius of 1.2 Å by PLATON, (ZNU-2-Si: a-c; ZNU-2-Ti: d-f; ZNU-2-Nb: h-i).

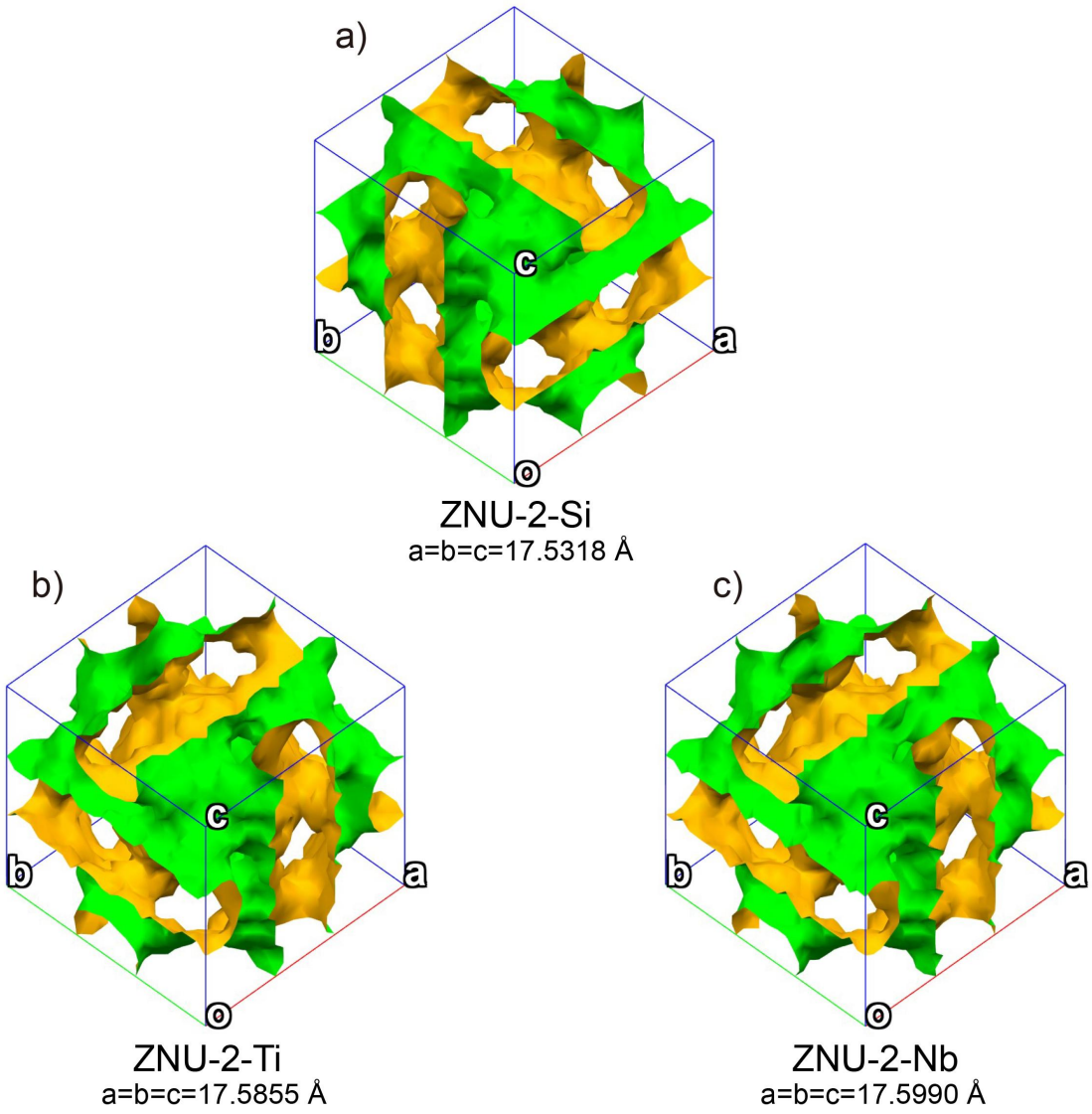

Fig. S3 Void surface of ZNU-2 family (Outside colour: yellow; Inside colour: green).

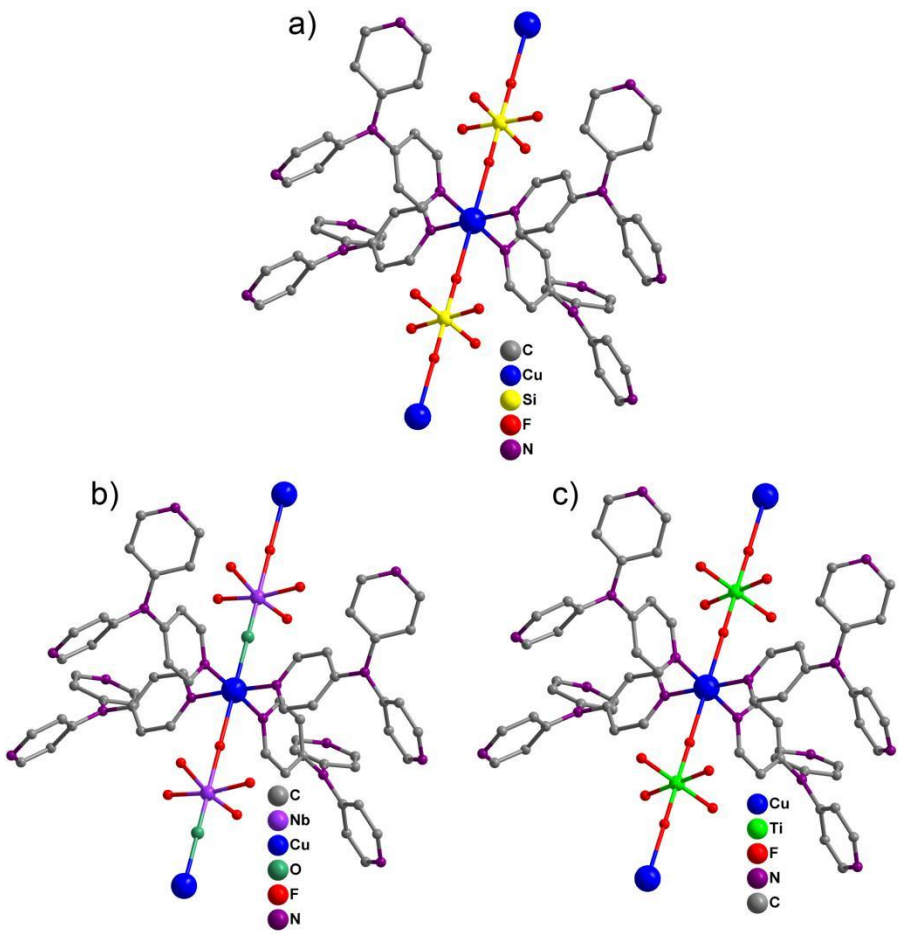

Fig. S4 The Cu(II) coordination environment of the ZNU-2 family (a: ZNU-2-Si; b; ZNU-2-Nb; c: ZNU-2-Ti).

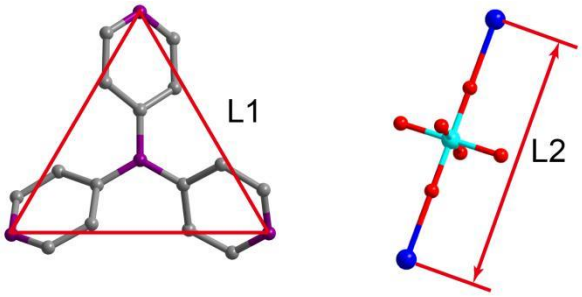

	ZNU-2-Si	ZNU-2-Ti	ZNU-2-Nb
L1 (Å)	7.255	7.269	7.273
L2 (Å)	8.766	8.793	8.800

Fig. S5 The dimensions of tridentate ligands and Cu-Cu distances of the ZNU-2 family .

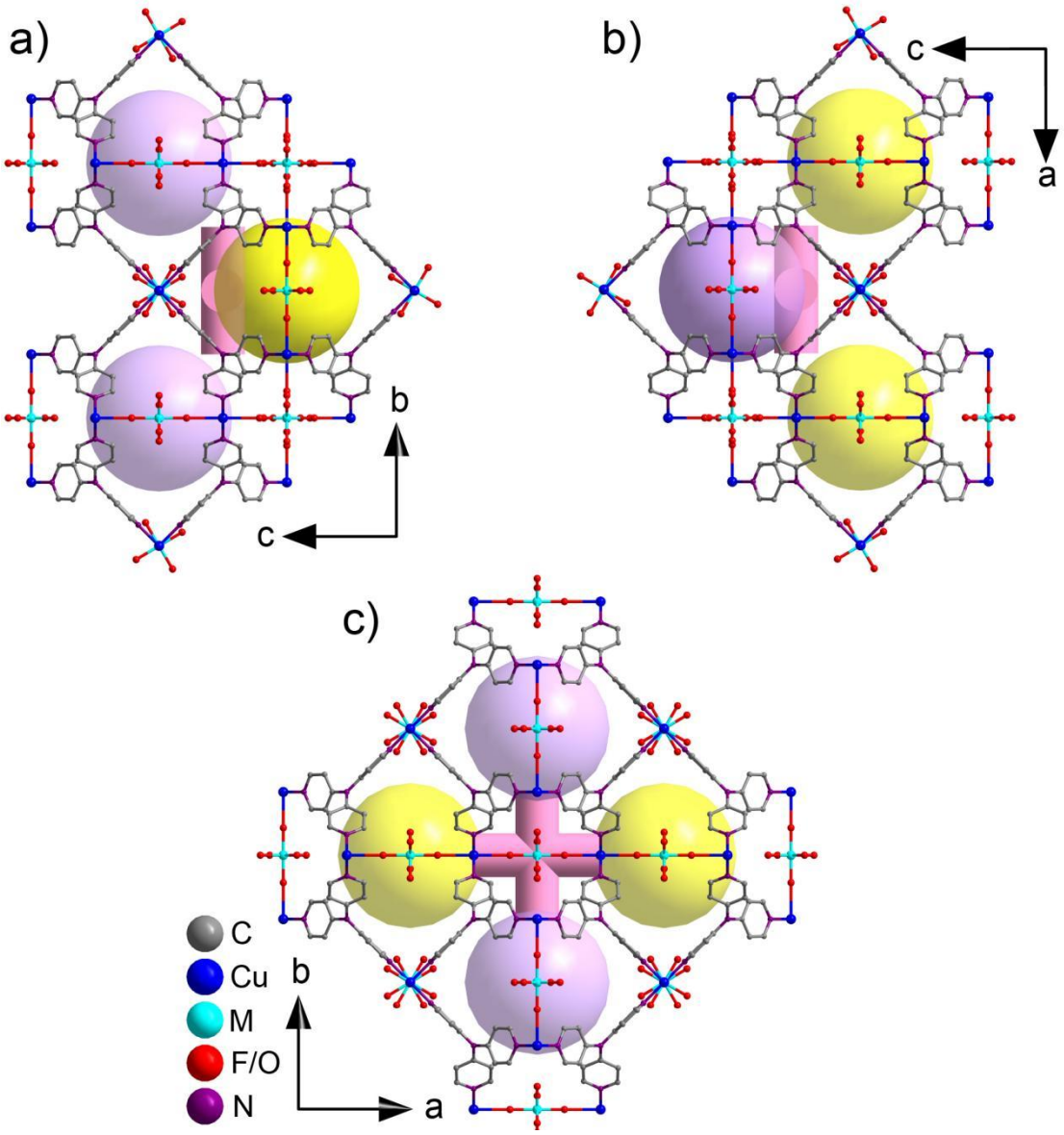

Fig. S6 Structure of the ZNU-2 family with cage-like pores and interlaced channel. One interlaced channel connects four cage-like pores.

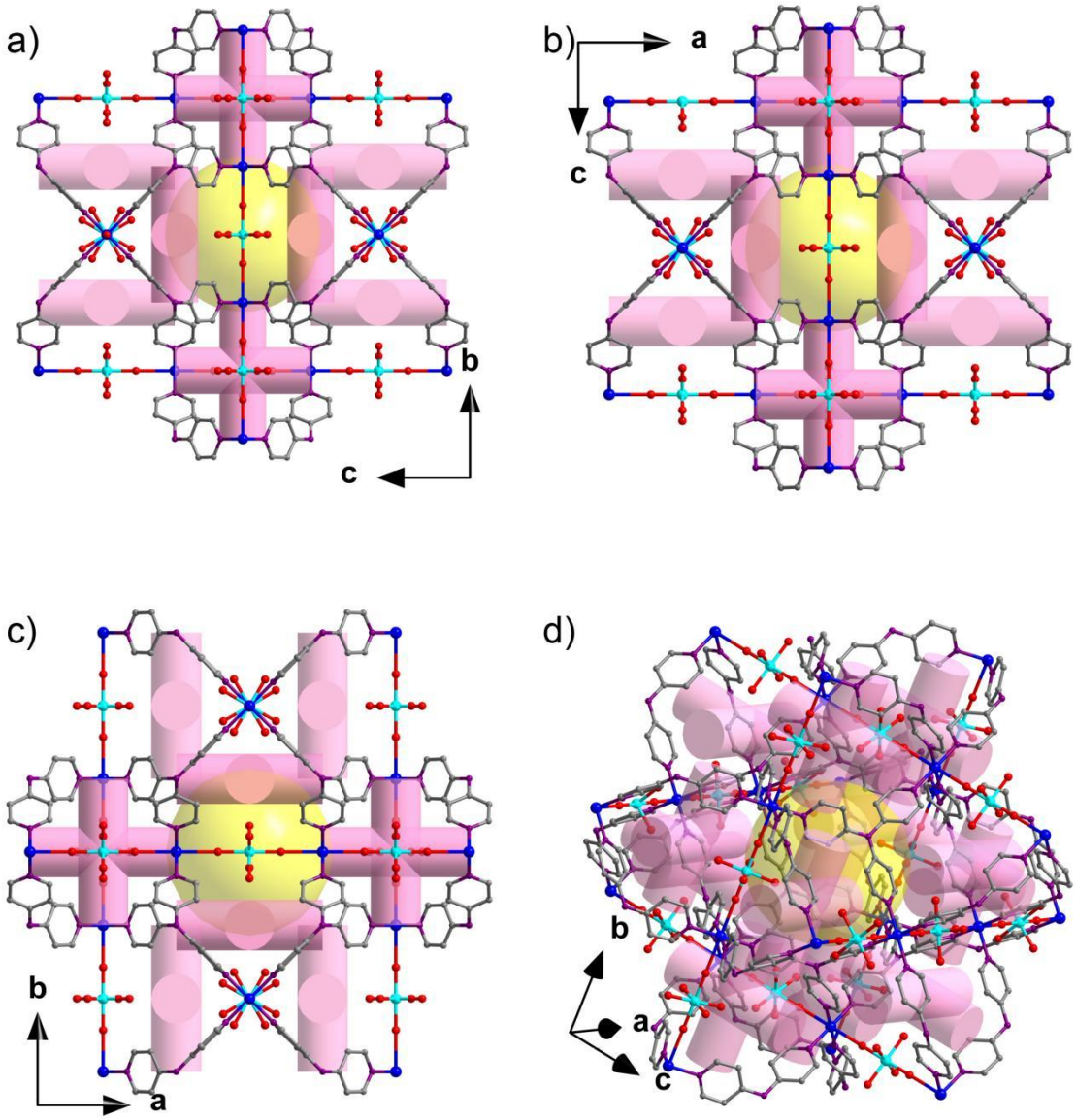

Fig. S7 Structure of the ZNU-2 family with cage-like pore and interlaced channels. One cage-like pore is surrounded with twelve interlaced channels.

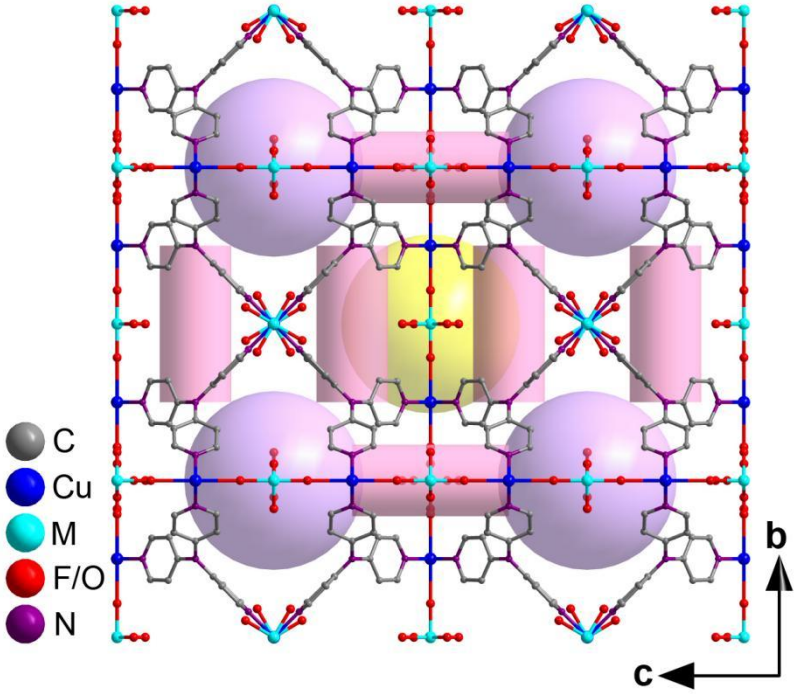

Fig. S8 Structure of the ZNU-2 family viewed from a axis..

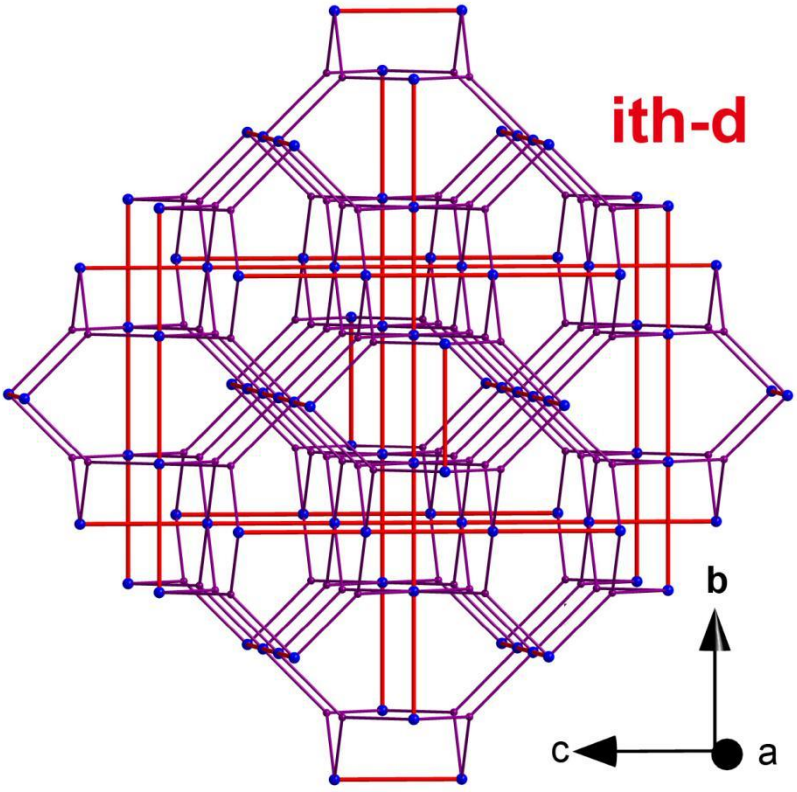

Fig. S9 The ith-d topology of the ZNU-2 family .

Table S1 Crystallographic parameters of the ZNU-2 family .

Materials	ZNU-2-Si	ZNU-2-Ti	ZNU-2-Nb
Cell	a=17.5318(3)	a=17.5855(9)	a=17.5990(5)
	b=17.5318(3)	b=17.5855(9)	b=17.5990(5)
	c=17.5318(3)	c=17.5855(9)	c=17.5990(5)
	α=90	α=90	α=90
	β=90	β=90	β=90
	γ=90	γ=90	γ=90
Temperature	293 K	173 K	184 K
Volume ($Å^3$)	5388.6(3)	5438.3(8)	5450.8(5)
Space group	Pm-3n	Pm-3n	Pm-3n
Hall group	-P 4n 2 3	-P 4n 2 3	-P 4n 2 3
formula	$C_{20}H_{16}CuF_6N_{5.33}Si$	$C_{20}H_{16}CuF_6N_{5.33}Ti$	$C_{60}H_{48}Cu_3F_{15}N_{16}Nb_3O_3$
MW	536.69	556.49	1795.46
density	0.992	1.020	1.094
Z	6	6	2
R	0.0530(887)	0.0586(989)	0.0487(797)
wR2	0.1813(1142)	0.1890(1137)	0.1458(924)
S	1.133	1.148	1.101
CCDC Nos.	2190368	2142633	2190367/2190959

Table S2 Crystallographic parameters of ZNU-2-Si.

Materials	ZNU-2-Si (as synthesized)	ZNU-2-Si (after activation)	ZNU-2-Si 24 C_3H_4 @ MOF	ZNU-2-Si 18 C_3H_6 @ MOF
Cell	a=17.5318(3)	a=17.5051(3)	a=17.5254(5)	a=17.4998(5)
	b=17.5318(3)	b=17.5051(3)	b=17.5254(5)	b=17.4998(5)
	c=17.5318(3)	c=17.5051(3)	c=17.5254(5)	c=17.4998(5)
	α=90	α=90	α=90	α=90
	β=90	β=90	β=90	β=90
	γ=90	γ=90	γ=90	γ=90
Temperature	293 K	102 K	100 K	101 K
Volume ($Å^3$)	5388.6(3)	5364.1(3)	5382.8(5)	5359.2(5)
Space group	Pm-3n	Pm-3n	Pm-3n	Pm-3n
Hall group	-P 4n 2 3	-P 4n 2 3	-P 4n 2 3	-P 4n 2 3
formula	$C_{20}H_{16}CuF_6N_{5.33}Si$	$C_{20}H_{16}CuF_6N_{5.33}Si$	$C_{32}H_{32}CuF_6N_{5.33}Si$	$C_{29}H_{34}CuF_6N_{5.33}Si$
MW	536.69	536.69	696.94	662.92
density	0.992	0.997	1.290	1.232
Z	6	6	6	6
R	0.0530 (887)	0.0362 (937)	0.0509 (874)	0.0926 (916)
wR2	0.1813 (1142)	0.1174 (1135)	0.1966 (915)	0.3134 (1135)
S	1.133	1.240	1.176	1.106
CCDC. Nos	2190368	2190370	2190371	2190372

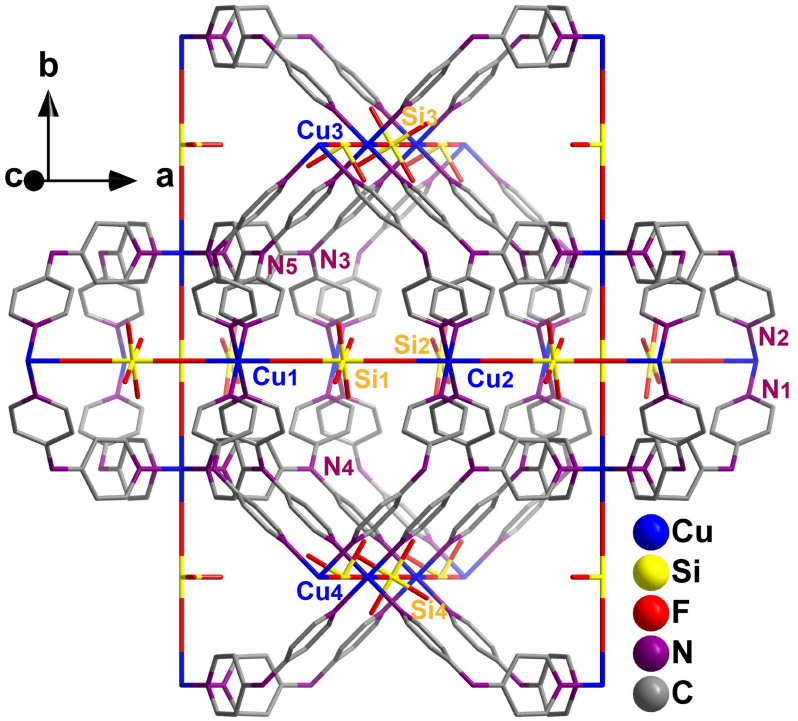

Table S3 Selected bond length in the structures of ZNU-2-Si.

	ZNU-2-Si (as synthesized)	ZNU-2-Si (after activation)	ZNU-2-Si C_3H_4 @ MOF	ZNU-2-Si C_3H_6 @ MOF
Cu1···Cu2	8.766	8.753	8.763	8.750
Cu3···Cu4	17.532	17.505	17.525	17.500
N1···N2	2.842	2.826	2.832	2.821
N3···N4	8.766	8.753	8.763	8.750
N3···N5	8.766	8.753	8.763	8.750
Si1···Si2	17.532	17.505	17.525	17.500
Si3···Si4	17.532	17.505	17.525	17.500

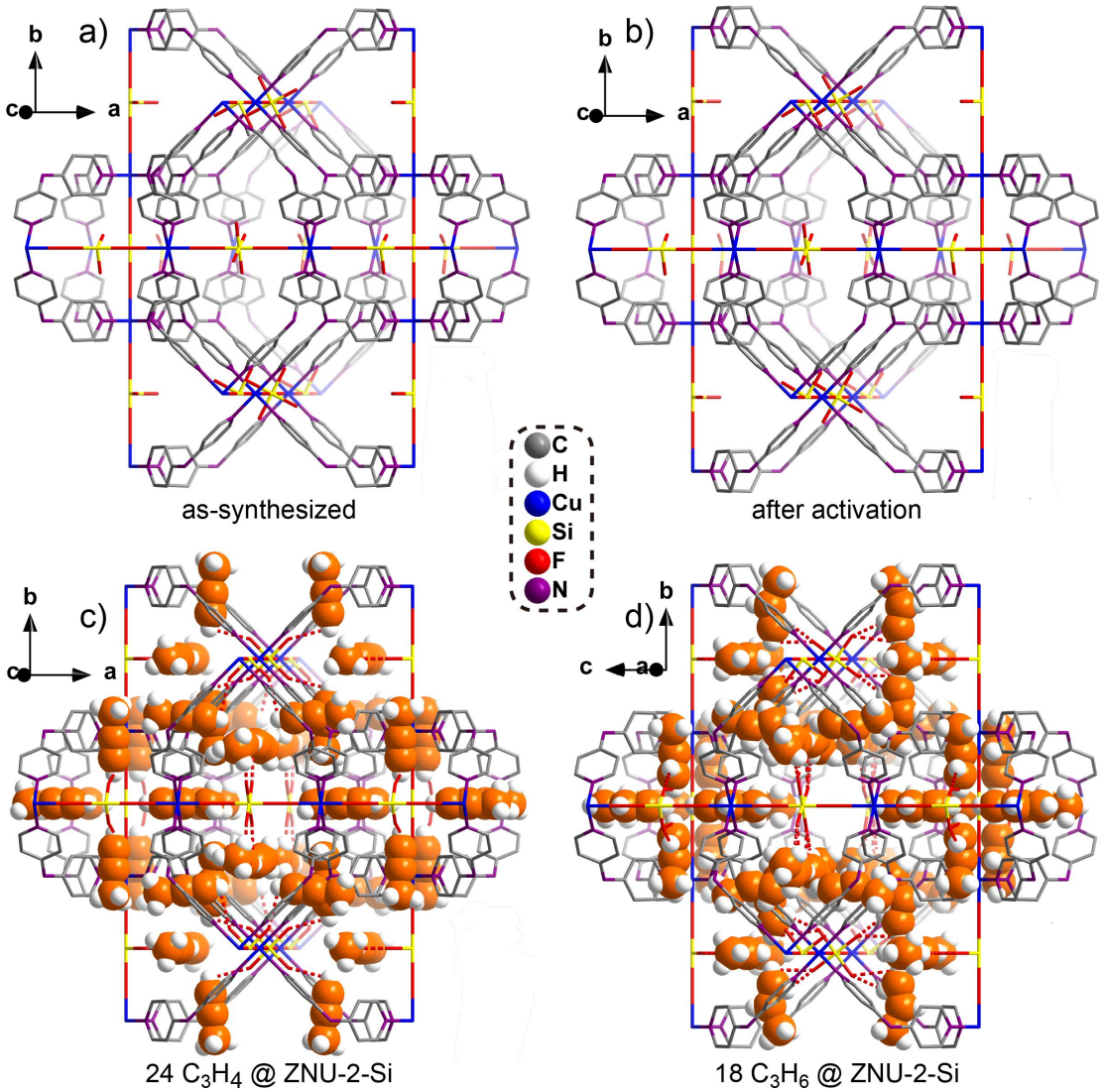

Fig. S10 Single crystal structure of (a) as-synthesized ZNU-2-Si. (b) activated ZNU-2-Si. (c) C_3H_4 loaded ZNU-2-Si. (d) C_3H_6 loaded ZNU-2-Si.

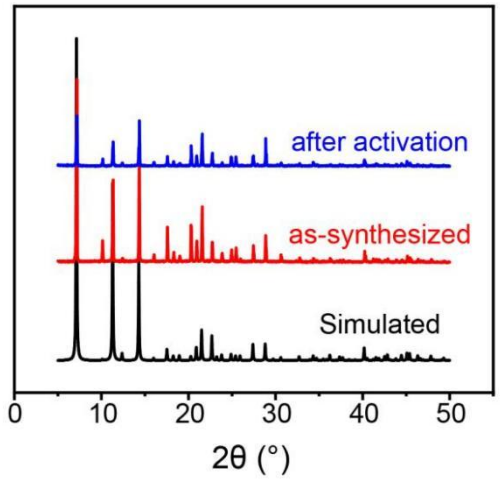

Fig. S11 PXRD patterns of ZNU-2-Si

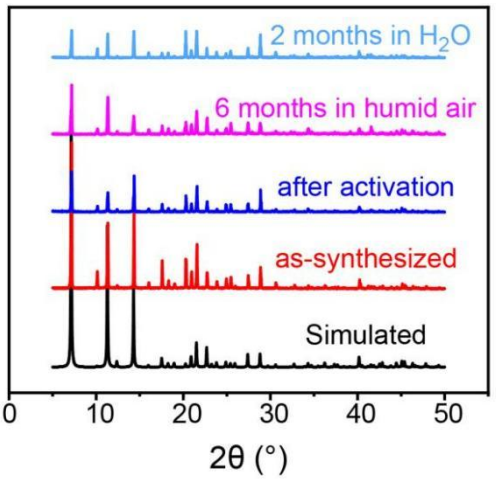

Fig. S12 PXRD patterns of ZNU-2-Si after different treatments.

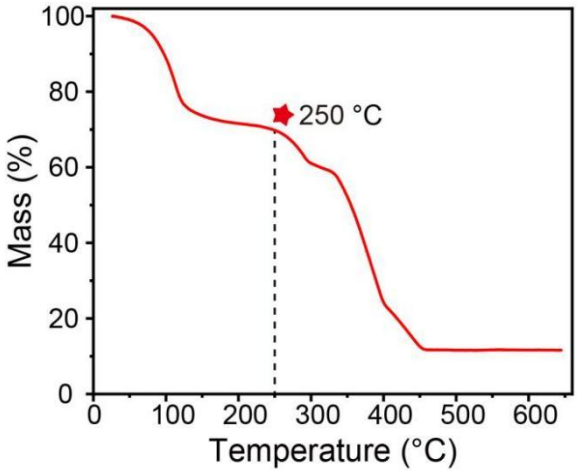

Fig. S13 TGA curve of ZNU-2-Si. The weight loss between 20-110 ºC is because of the loss of MeOH and water from the sample. The weight keeps consistent until ~250 ºC.

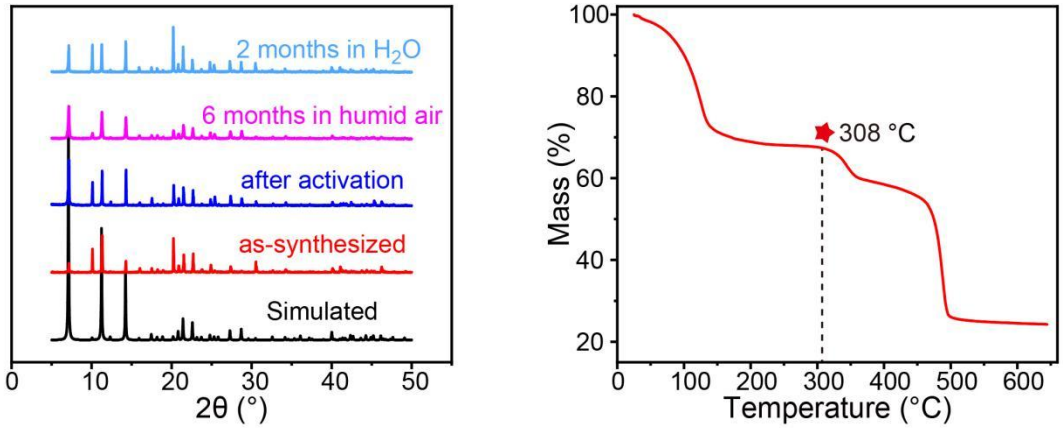

Fig. S14 PXRD patterns of ZNU-2-Ti after different treatments (Left). TGA curve of ZNU-2-Ti (Right). The weight loss between 30-110 ºC is because of the loss of MeOH and water from the sample. The weight keeps consistent until ~308 ºC.

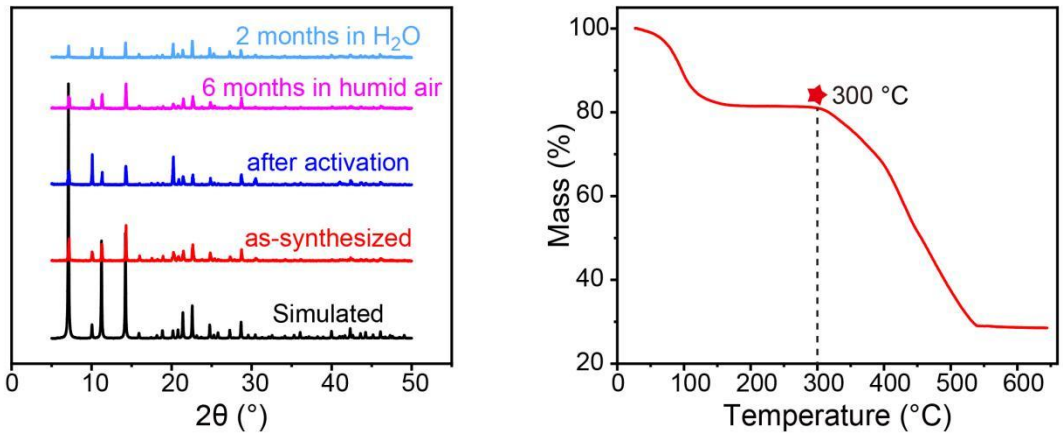

Fig. S15 PXRD patterns of ZNU-2-Nb after different treatments (Left). TGA curve of ZNU-2-Nb (Right). The weight loss between 30-110 ºC is because of the loss of MeOH and water from the sample. The weight keeps consistent until ~300 ºC.

III Adsorption data, IAST selectivity and *Q*st

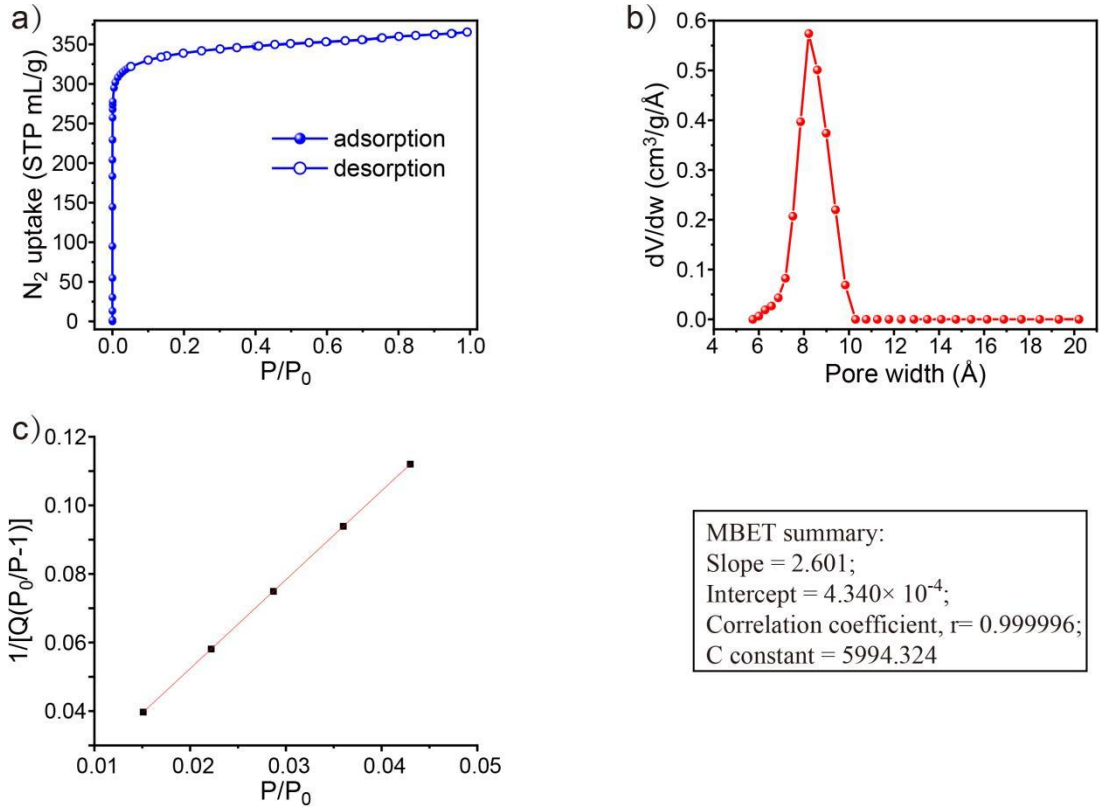

Fig. S16 (A) The adsorption and desorption isotherm of N_2 on ZNU-2-Si at 77 K. (B) The calculated pore size distribution of ZNU-2-Si. (C) Plot for the calculation of the BET surface area.

The BET surface area calculated from the N_2 adsorption isotherms under the pressure range of P/P_0 = 0.01-0.05 (for micropores) is 1339 m^2/g.

The total pore volume calculated from the N_2 adsorption isotherms is 0.565 cm^3/g.

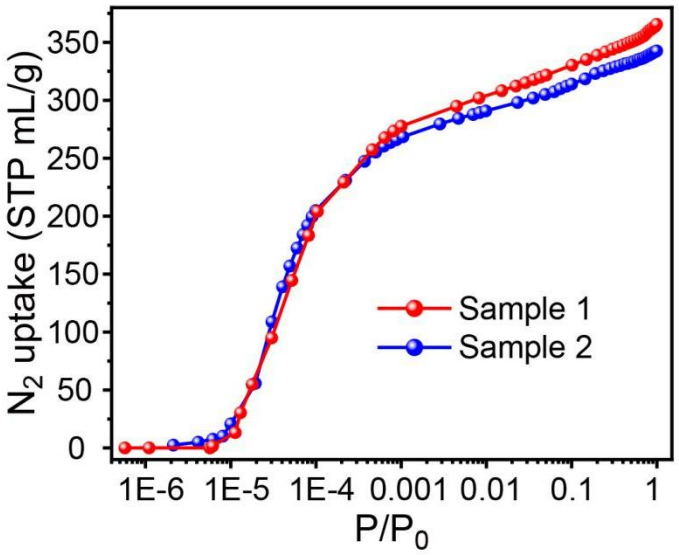

Fig. S17 The adsorption isotherms of N_2 on two batches of ZNU-2-Si samples at 77 K.

The adsorption curve of 77 K N_2 for sample 2 is approximately consistent with that for sample 2. This means that the synthesis of ZNU-2-Si is repeatable.

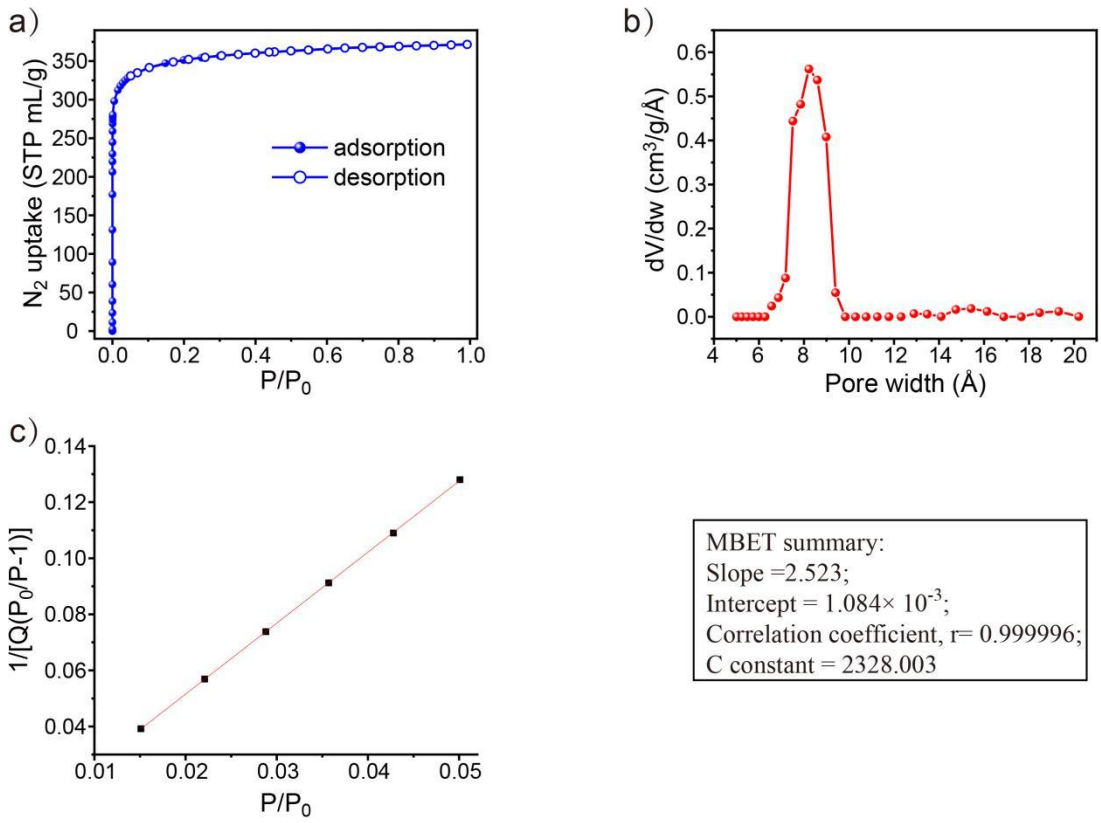

Fig. S18 (A) The adsorption and desorption isotherm of N_2 on ZNU-2-Ti at 77 K. (B) The calculated pore size distribution of ZNU-2-Ti. (C) Plot for the calculation of the BET surface area.

The BET surface area calculated from the N_2 adsorption isotherms under the pressure range of P/P_0 = 0.01-0.05 (for micropores) is 1380 m^2/g.

The total pore volume calculated from the N_2 adsorption isotherms is 0.575 cm^3/g.

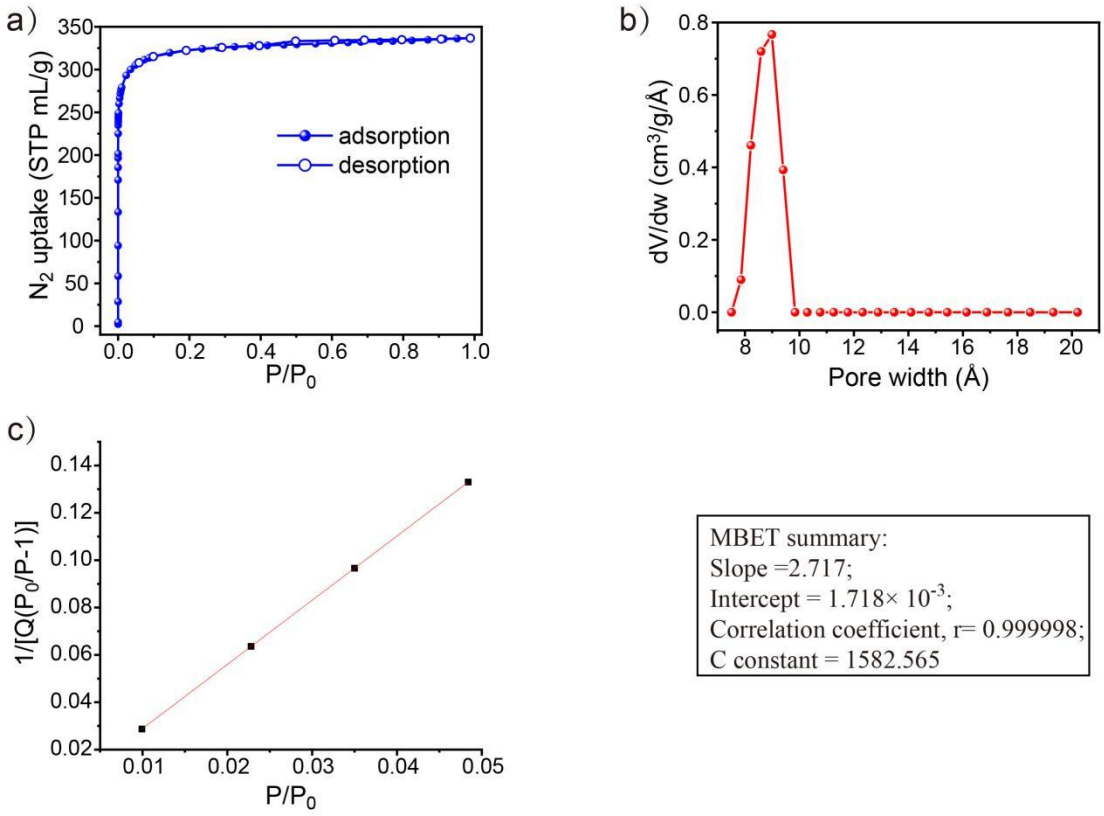

Fig. S19 (A) The adsorption and desorption isotherm of N_2 on ZNU-2-Nb at 77 K. (B) The calculated pore size distribution of ZNU-2-Nb. (C) Plot for the calculation of the BET surface area.

The BET surface area calculated from the N_2 adsorption isotherms under the pressure range of P/P_0 = 0.01-0.05 (for micropores) is 1281 m^2/g.

The total pore volume calculated from the N_2 adsorption isotherms is 0.521 cm^3/g.

Table S4 Comparison of C_3H_4, C_3H_6, C_2H_2, C_2H_4 and CO_2.

Gas molecules	Kinetic Diameter (Å)	Molecular size (Å^3)	Boiling point (K)	Polarizability ($\times 10^{-25}$ cm^3)
C_3H_4	4.2	4.16 x 4.01 x 6.51	249.95	55.5
C_3H_6	4.6	4.65 x 4.16 x 6.44	225.45	62.6
C_2H_2	3.3	3.32 x 3.34 x 5.70	189.3	33.3-39.3
C_2H_4	4.2	3.28 x 4.18 x 4.84	169.5	42.5
CO_2	3.3	3.18 x 3.33 x 5.36	194.7	25.93

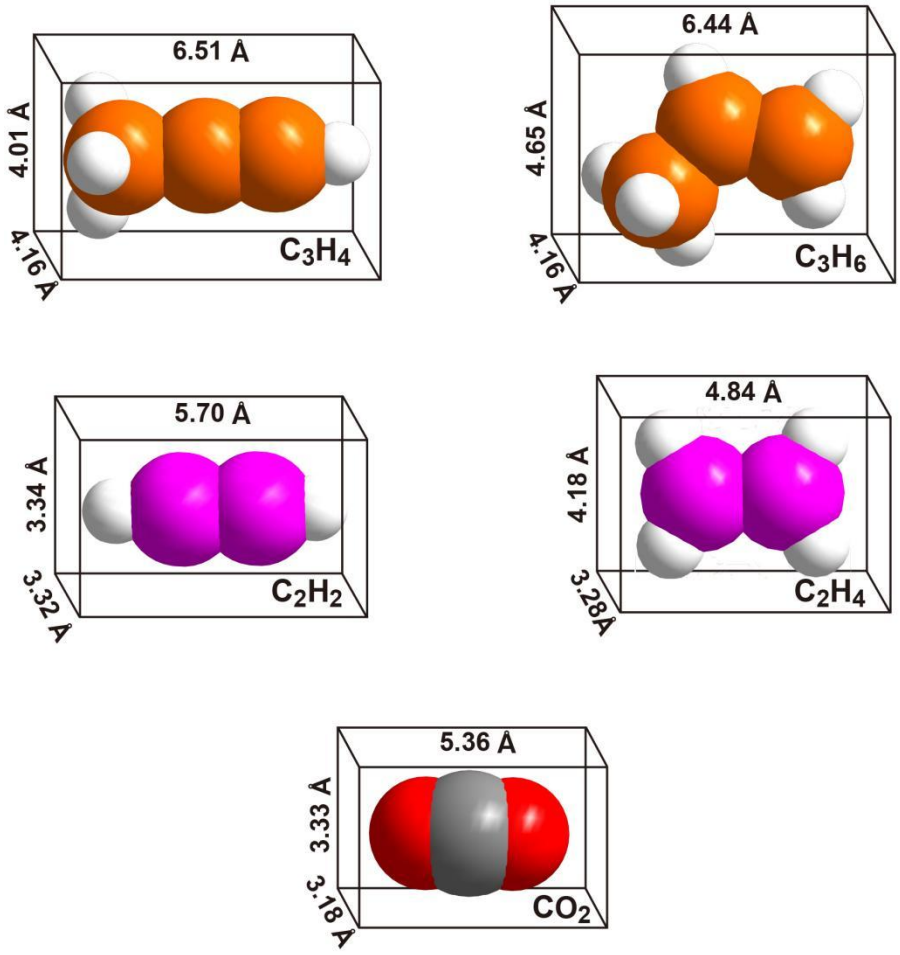

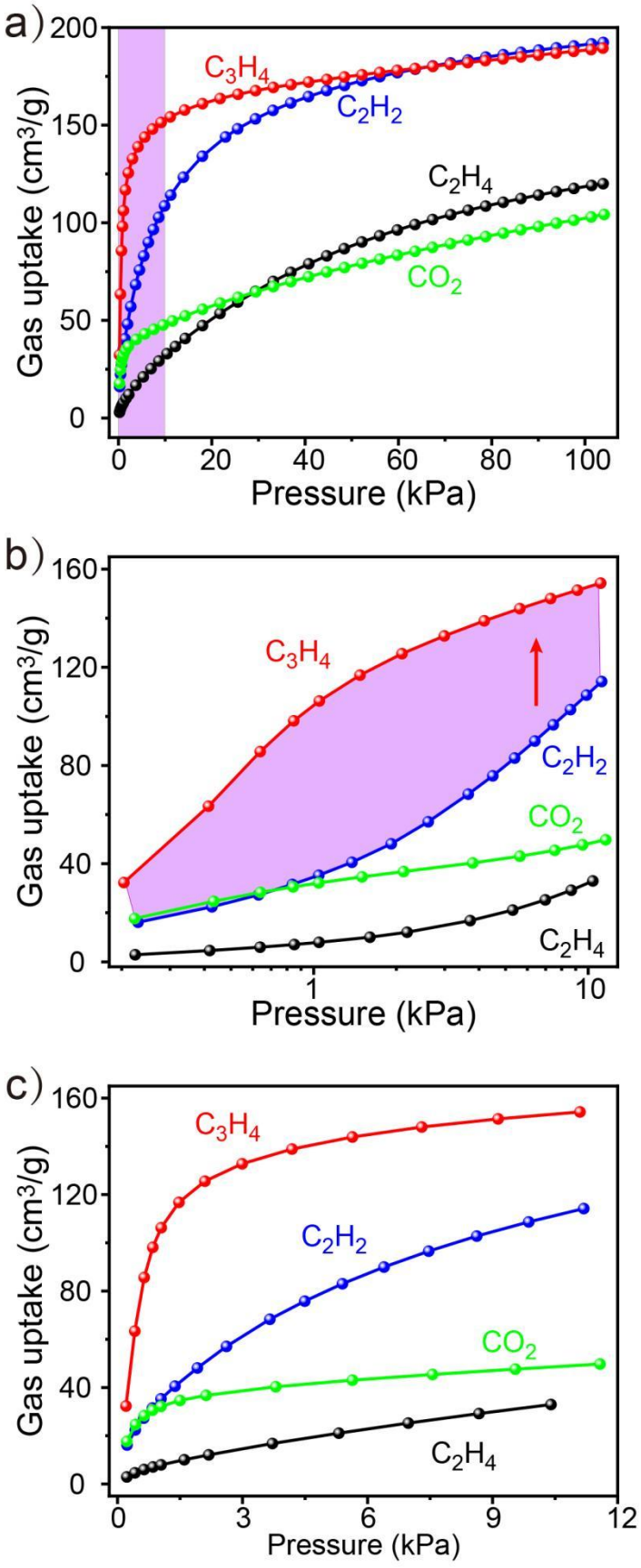

Fig. S20 Comparison of the C_3H_4, C_2H_2, CO_2, C_2H_4 adsorption isotherms on ZNU-2-Si (a: between 1-100 kPa, b, c: between 1-10 kPa).

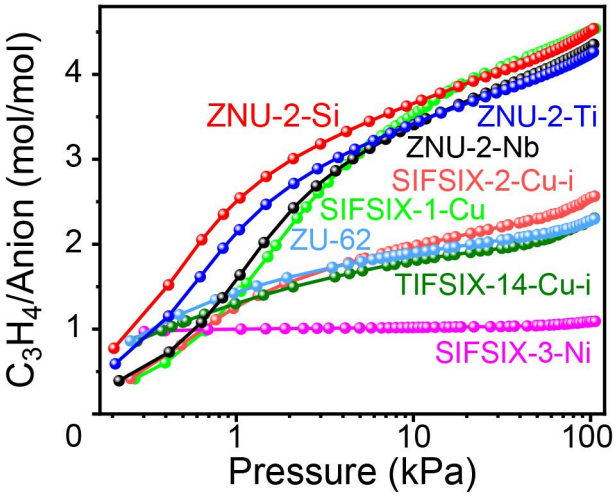

Fig. S21 Comparison of the C_3H_4 adsorption isotherms of the ZNU-2 family with fluorinated anion hybrid ultramicroporous materials.

Table S5 Comparison of the C_3H_4 adsorption isotherms of ZNU-2 family with fluorinated anion hybrid ultramicroporous materials.

	C_3H_4/Anion (mol/mol)			
	1 kPa	10 kPa	100 kPa	
ZNU-2-Si	**2.54**	**3.66**	**4.54**	**This work**
ZNU-2-Ti	**2.17**	**3.42**	**4.26**	**This work/[15]**
ZNU-2-Nb	**1.64**	**3.41**	**4.35**	**This work**
SIFSIX-1-Cu	1.45	3.53	4.52	This work/[5]
SIFSIX-2-Cu-i	1.25	1.97	2.57	This work/[5,13,14]
TIFSIX-14-Cu-i	1.30	1.80	2.31	This work/[13]
ZU-62	1.47	1.89	2.30	This work/[14]
SIFSIX-3-Ni	1.00	1.02	1.09	This work/[5]

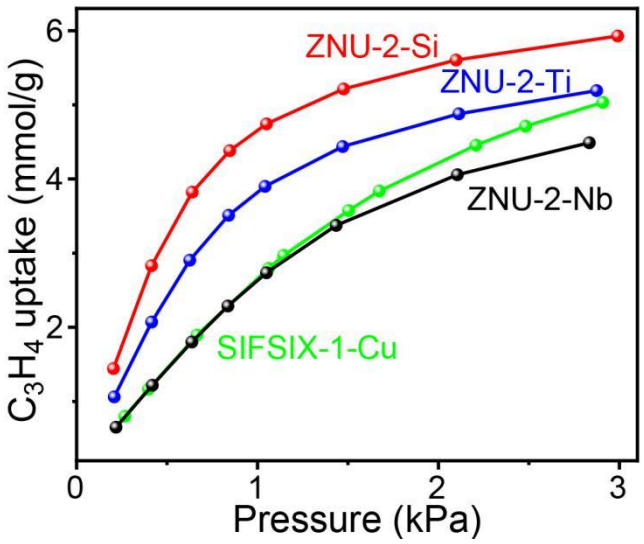

Fig. S22 Comparison of the C_3H_4 adsorption isotherms of the ZNU-2 family with SIFSIX-1-Cu between 1-3 kPa.

Table S6 Comparison of the C_3H_4 storage density of ZNU-2 family and liquid C_3H_4.

	storage density (g/cm^3)
ZNU-2-Si (298 K)	0.60
ZNU-2-Ti (298 K)	0.53
ZNU-2-Nb (298 K)	0.56
ZNU-2-Si (278 K)	0.65
C_3H_4 (l)	0.67

Storage density= Q (adsorption capacity, mmol/g) × M (relative molecular mass, mg/mmol) / V (pore volume, cm^3/g)

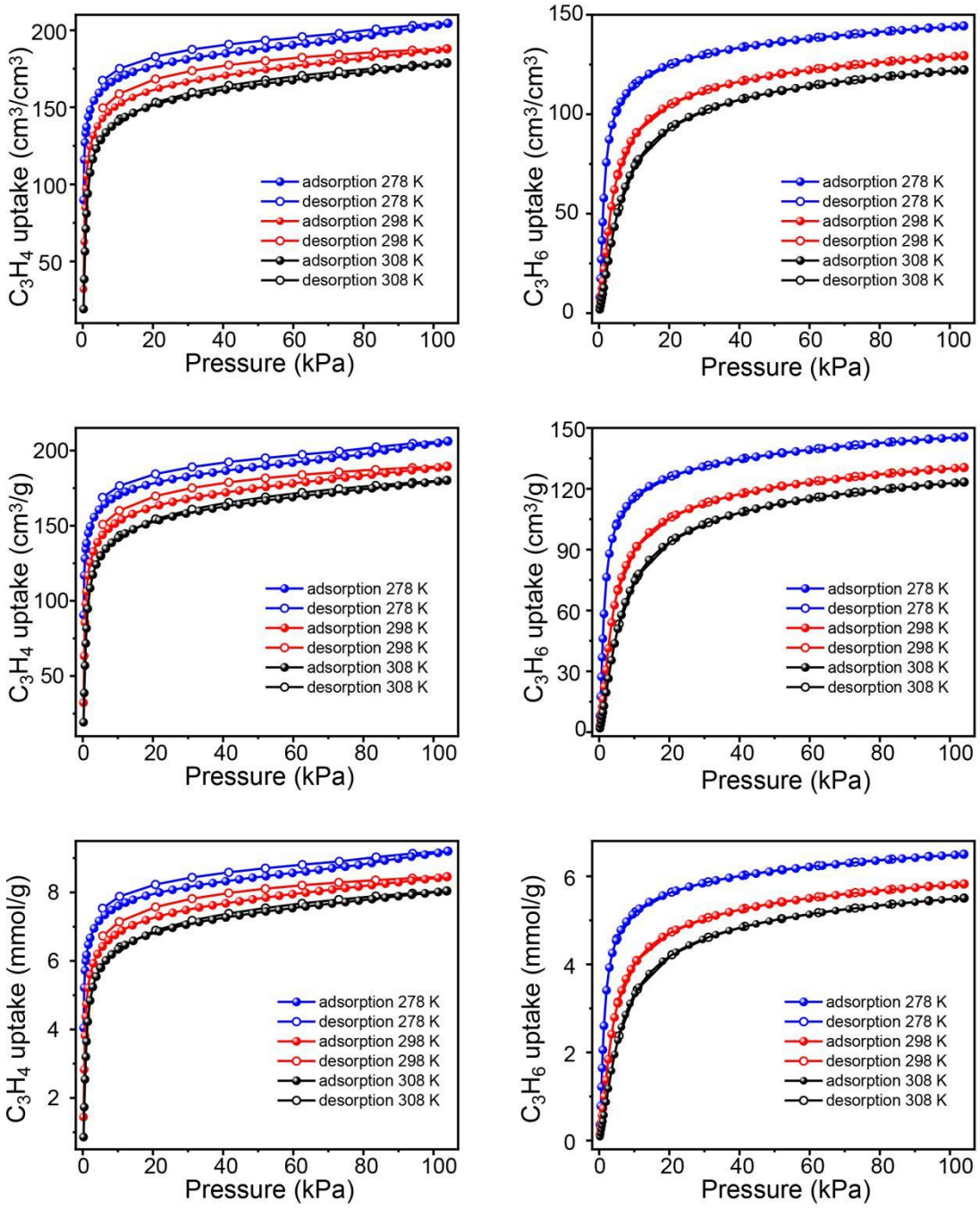

Fig. S23 The sorption isotherms of C_3H_4 and C_3H_6 on ZNU-2-Si at 278, 298, and 308 K in units of cm^3/cm^3, cm^3/g and mmol/g.

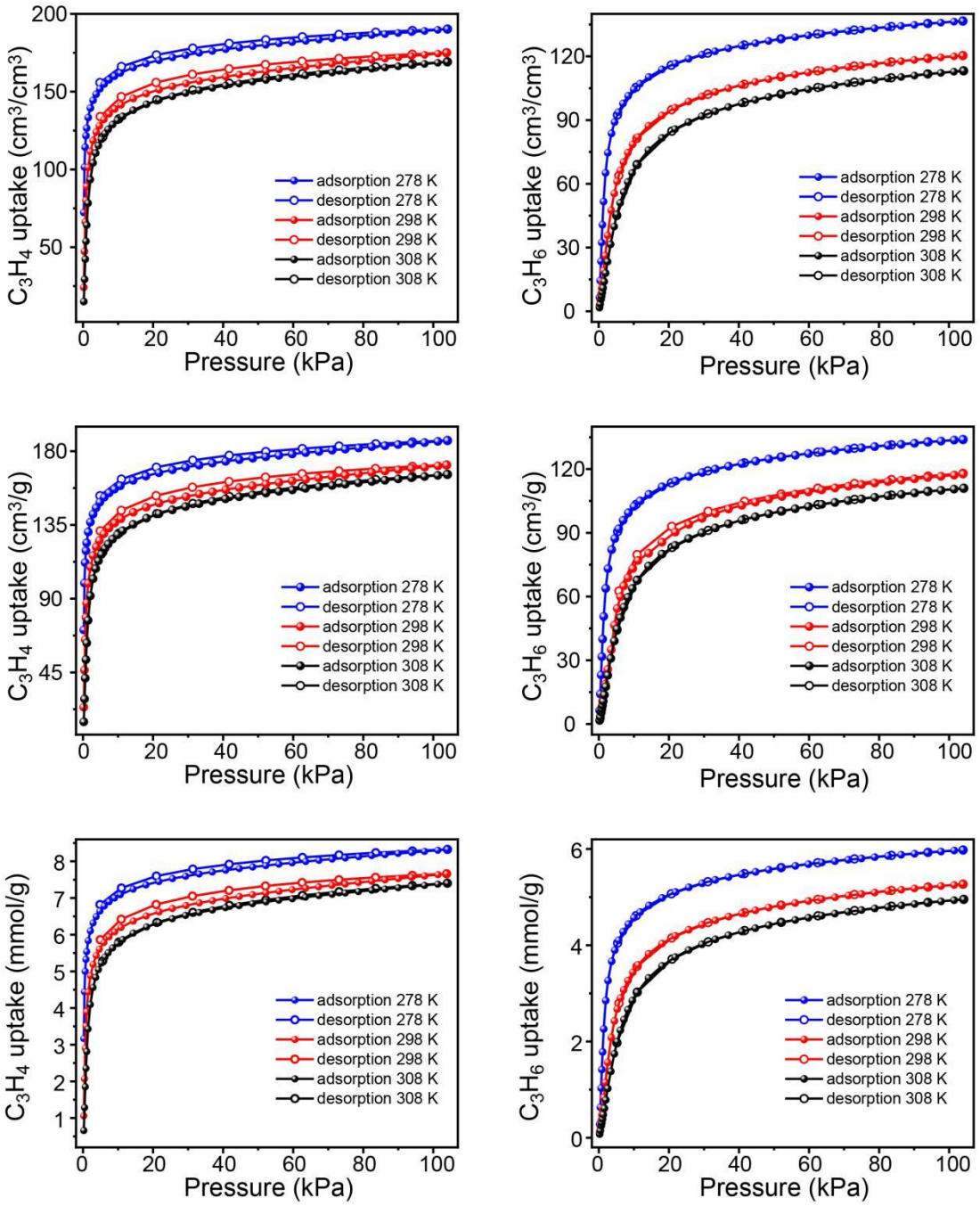

Fig. S24 The sorption isotherms of C_3H_4 and C_3H_6 on ZNU-2-Ti at 278, 298, and 308 K in units of cm^3/cm^3, cm^3/g and mmol/g.

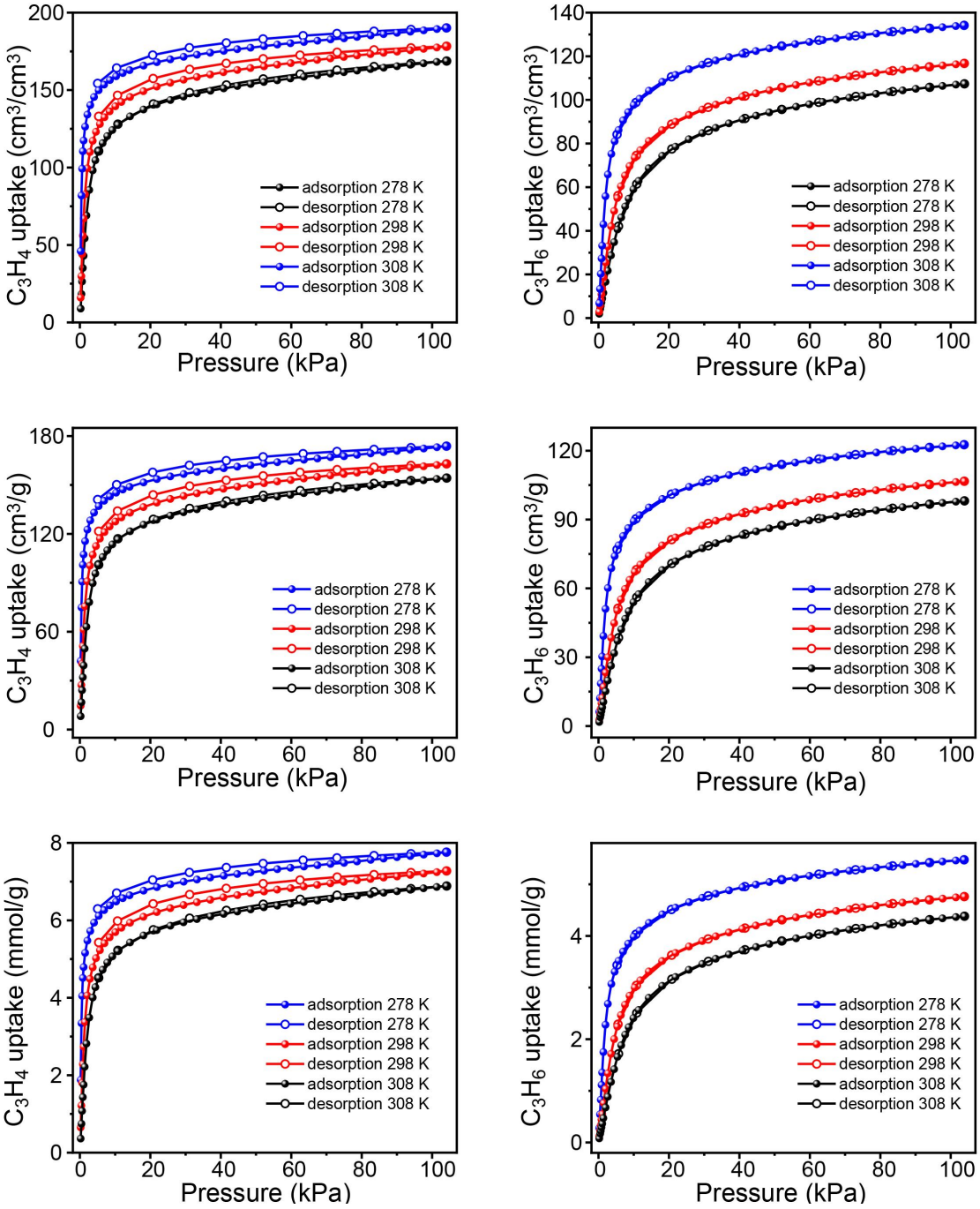

Fig. S25 The sorption isotherms of C_3H_4 and C_3H_6 on ZNU-2-Nb at 278, 298, and 308 K in units of cm^3/cm^3, cm^3/g and mmol/g.

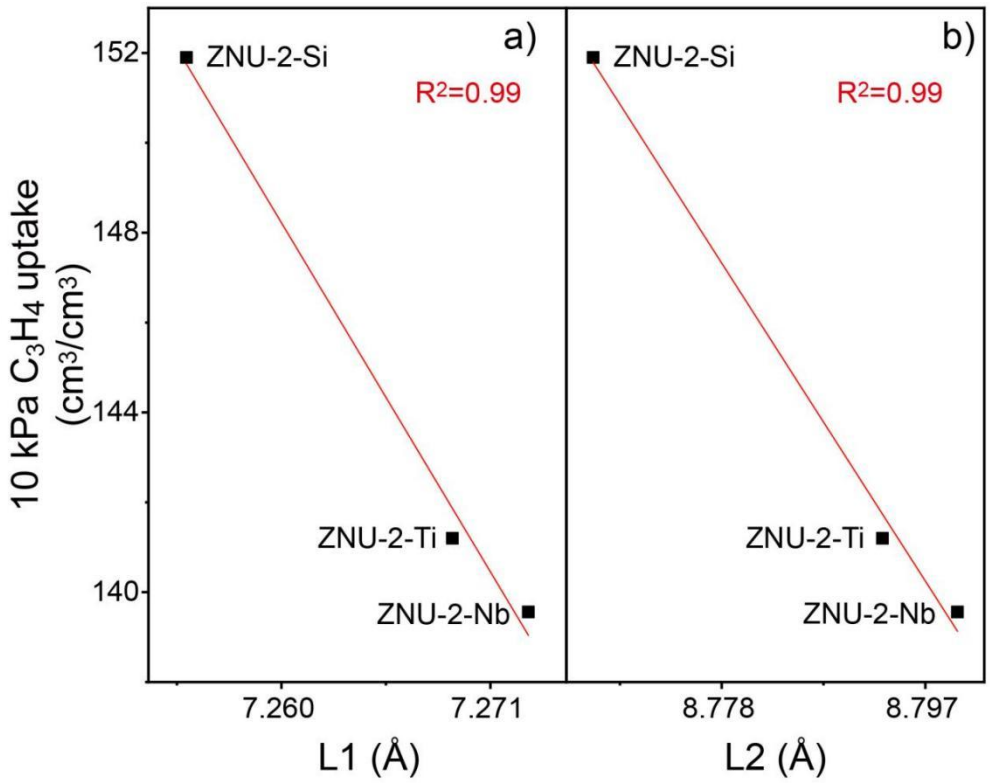

a)	y=-706.12 x + 5274.65	R^2=0.99
b)	y=-372.25 x + 3414.97	R^2=0.99

Fig. S26 Plots of the C_3H_4 uptake at 10 kPa on ZNU-2 and the dimensions of tridentate ligands (L1) and Cu-Cu distances (L2) of ZNU-2.

Table S7 Dual-site Langmuir-Freundlich fits for C_3H_4, and C_3H_6 in ZNU-2-Si.

	Site A				Site B			
	$q_{A,sat}$ mol kg^{-1}	b_{A0} Pa$^{-\nu A}$	E_A kJ mol^{-1}	νA	$q_{B,sat}$ mol kg^{-1}	b_{B0} Pa$^{-\nu B}$	E_B kJ mol^{-1}	νB
C_3H_4	6.42	6.616E-14	55.4	1.28	2.8	4.036E-13	44	1
C_3H_6	5.2	4.575E-13	44.3	1.26	1.65	2.132E-15	54.2	1

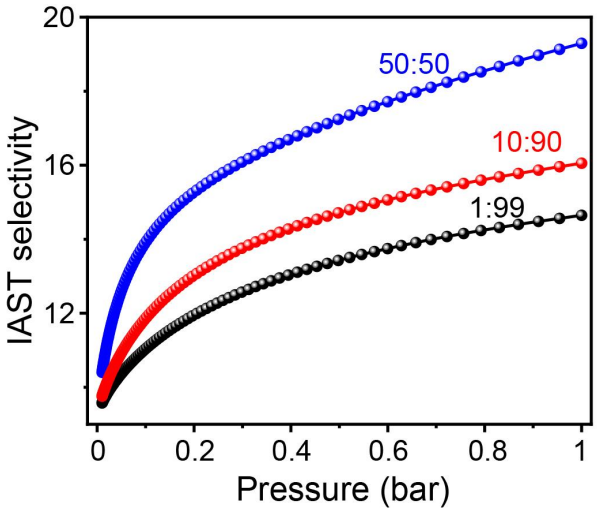

Fig. S27 IAST selectivity of ZNU-2-Si towards gas mixtures of C_3H_4/C_3H_6 (50/50 10/90 and 1/99) at 298 K.

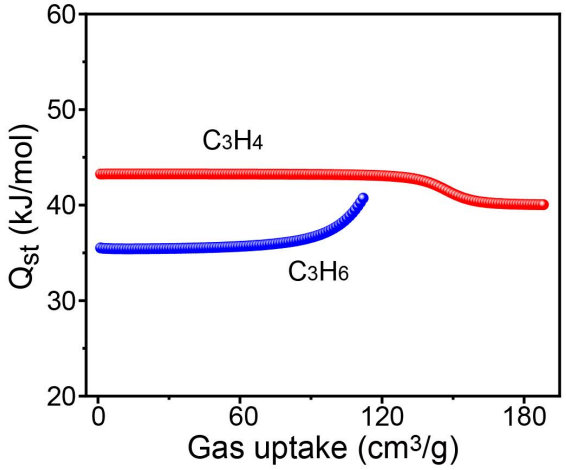

Fig. S28 The isosteric heat of adsorption, Q_{st}, for C_3H_4 and C_3H_6 on ZNU-2-Si.

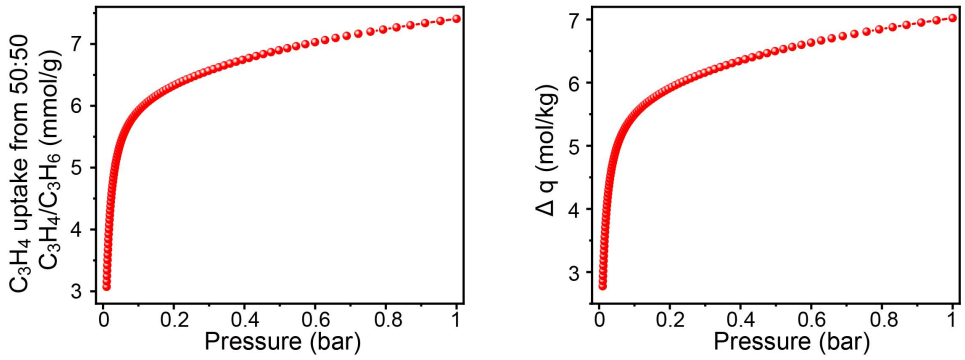

Fig. S29 Left: the adsorption isotherm of C_3H_4 from C_3H_4/C_3H_6 (50/50) mixture on ZNU-2-Si. Right: IAST based separation potential for C_3H_4/C_3H_6 (50/50) mixtures.

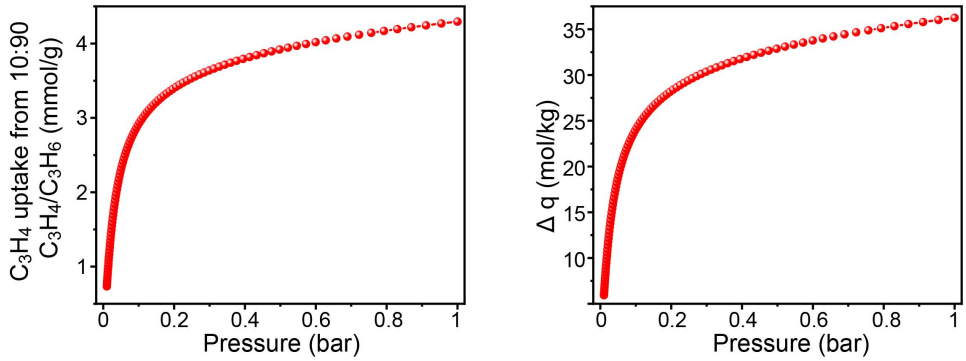

Fig. S30 Left: the adsorption isotherm of C_3H_4 from C_3H_4/C_3H_6 (10/90) mixture on ZNU-2-Si. Right: IAST based separation potential for C_3H_4/C_3H_6 (10/90) mixtures.

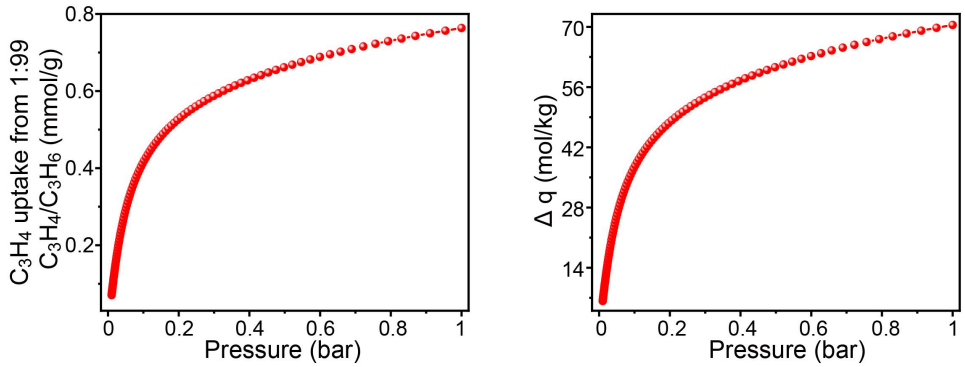

Fig. S31 Left: the adsorption isotherm of C_3H_4 from C_3H_4/C_3H_6 (1/99) mixture on ZNU-2-Si. Right: IAST based separation potential for C_3H_4/C_3H_6 (1/99) mixtures.

Table S8 Dual-site Langmuir-Freundlich fits for C_3H_4, and C_3H_6 in ZNU-2-Ti.

	Site A				Site B			
	$q_{A,sat}$ mol/kg	b_{A0} Pa^{-1}	E_A kJ/mol	νA	$q_{B,sat}$ mol/kg	b_{B0} Pa^{-1}	E_B kJ/mol	νB
C_3H_4	6	1.387E-13	53.3	1.24	2.5	3.443E-13	44.2	1
C_3H_6	4.4	3.417E-13	44.4	1.3	2.1	6.722E-14	46	1

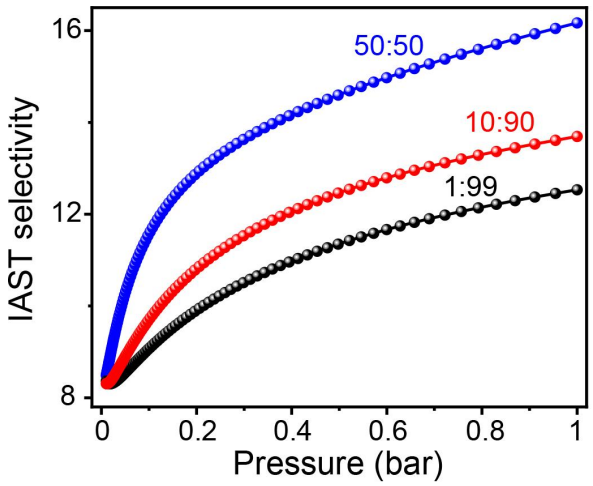

Fig. S32 IAST selectivity of ZNU-2-Ti towards gas mixtures of C_3H_4/C_3H_6 (50/50 10/90 and 1/99) at 298 K.

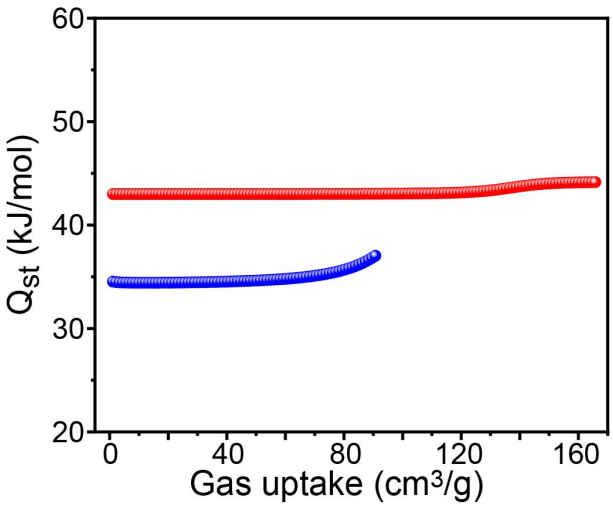

Fig. S33 The isosteric heat of adsorption, Q_{st}, for C_3H_4 and C_3H_6 on ZNU-2-Ti.

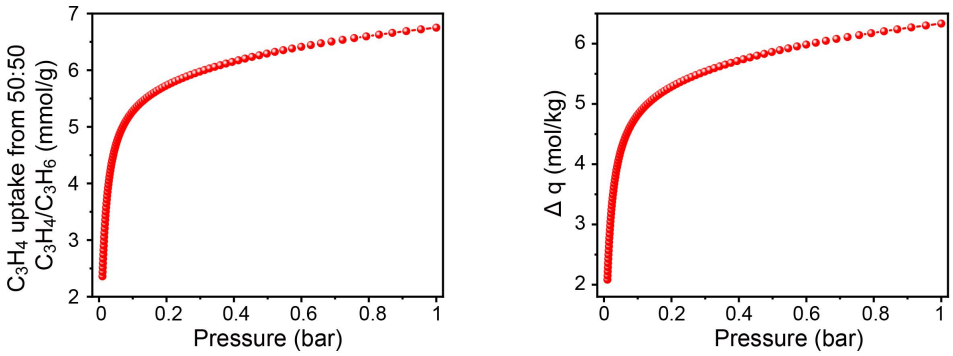

Fig. S34 Left: the adsorption isotherm of C_3H_4 from C_3H_4/C_3H_6 (50/50) mixture on ZNU-2-Ti. Right: IAST based separation potential for C_3H_4/C_3H_6 (50/50) mixtures.

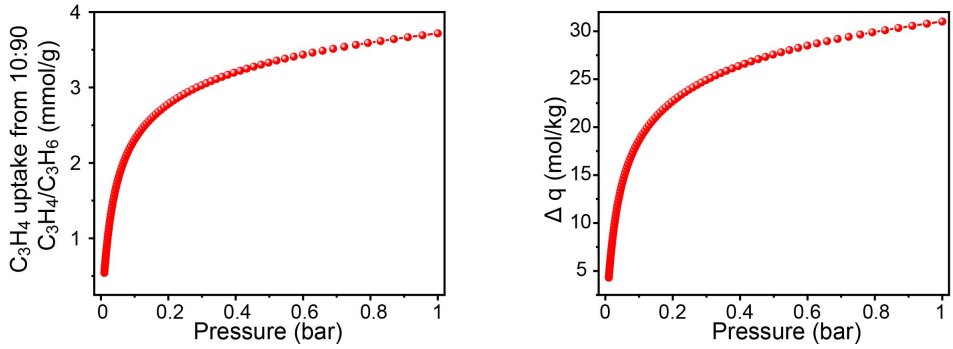

Fig. S35 Left: the adsorption isotherm of C_3H_4 from C_3H_4/C_3H_6 (10/90) mixture on ZNU-2-Ti. Right: IAST based separation potential for C_3H_4/C_3H_6 (10/90) mixtures.

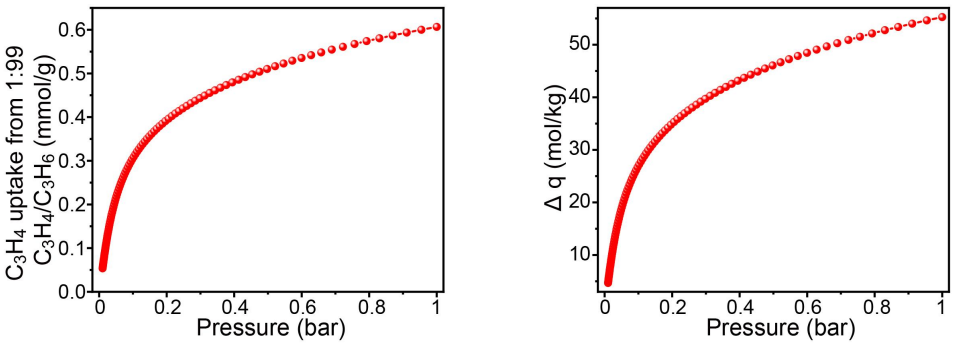

Fig. S36 Left: the adsorption isotherm of C_3H_4 from C_3H_4/C_3H_6 (1/99) mixture on ZNU-2-Ti. Right: IAST based separation potential for C_3H_4/C_3H_6 (1/99) mixtures.

Table S9 Dual-site Langmuir-Freundlich fits for C_3H_4, and C_3H_6 in ZNU-2-Nb.

	Site A				Site B			
	$q_{A,sat}$ mol kg^{-1}	b_{A0} $Pa^{-\nu A}$	E_A kJ mol^{-1}	νA	$q_{B,sat}$ mol kg^{-1}	b_{B0} $Pa^{-\nu B}$	E_B kJ mol^{-1}	νB
C_3H_4	5.9	3.368E-13	50	1.2	2.2	1.716E-12	39.2	1
C_3H_6	4.2	2.960E-11	36	1.13	1.6	1.972E-16	60	1

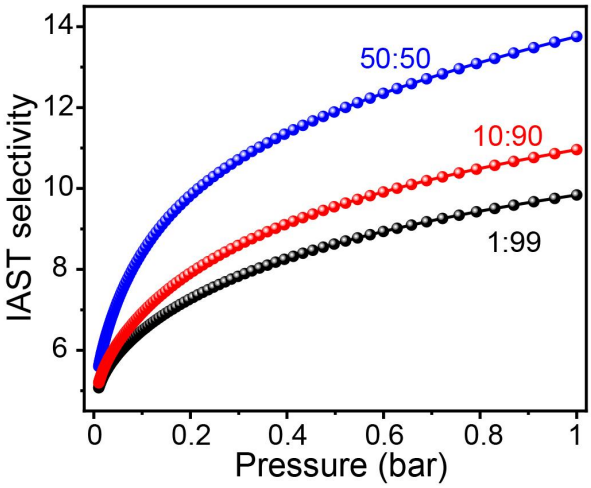

Fig. S37 IAST selectivity of ZNU-2-Nb towards gas mixtures of C_3H_4/C_3H_6 (50/50 10/90 and 1/99) at 298 K.

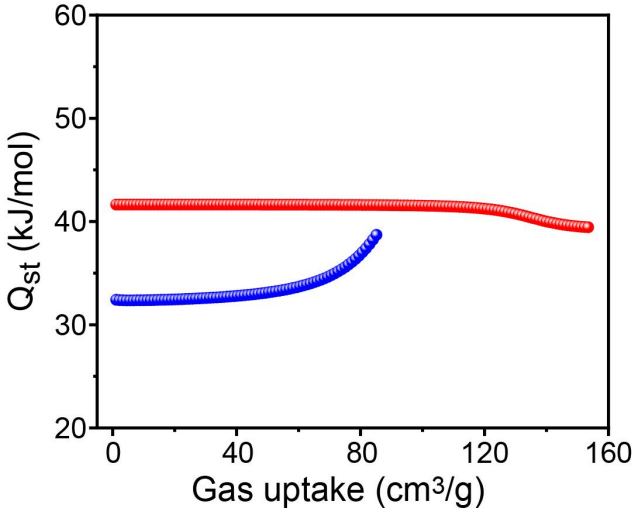

Fig. S38 The isosteric heat of adsorption, Q_{st}, for C_3H_4 and C_3H_6 on ZNU-2-Nb.

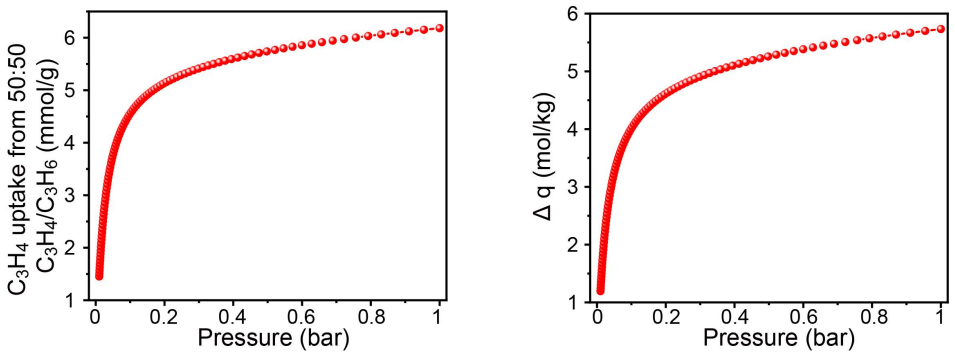

Fig. S39 Left: the adsorption isotherm of C_3H_4 from C_3H_4/C_3H_6 (50/50) mixture on ZNU-2-Nb. Right: IAST based separation potential for C_3H_4/C_3H_6 (50/50) mixtures.

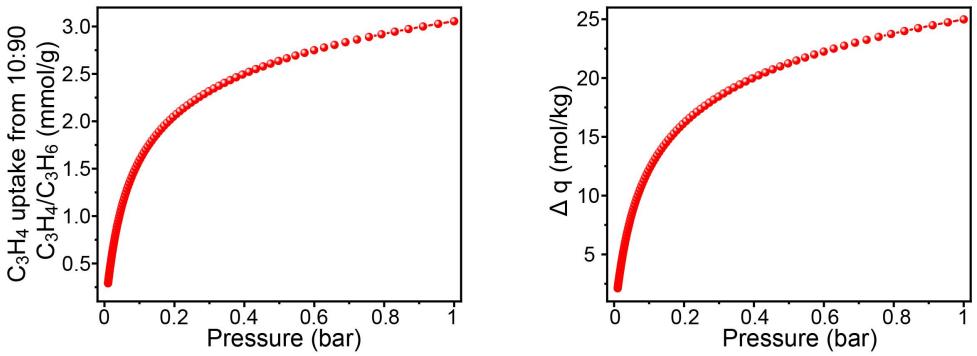

Fig. S40 Left: the adsorption isotherm of C_3H_4 from C_3H_4/C_3H_6 (10/90) mixture on ZNU-2-Nb. Right: IAST based separation potential for C_3H_4/C_3H_6 (10/90) mixtures.

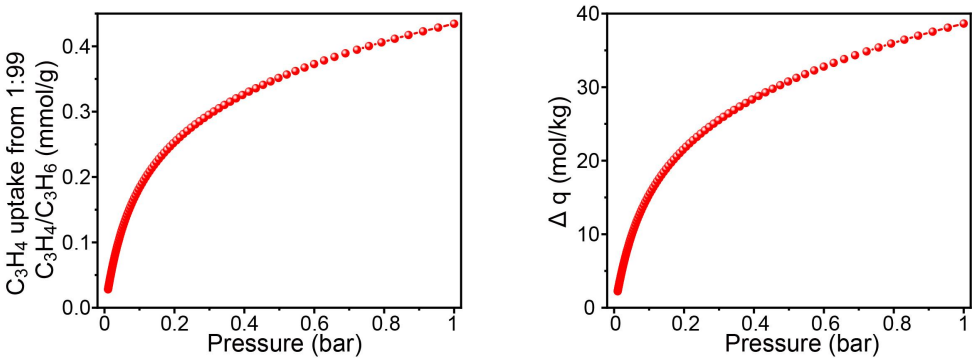

Fig. S41 Left: the adsorption isotherm of C_3H_4 from C_3H_4/C_3H_6 (1/99) mixture on ZNU-2-Nb. Right: IAST based separation potential for C_3H_4/C_3H_6 (1/99) mixtures.

Fig. S10 Unary isotherm fit parameters for C_3H_4 and C_3H_6 in SIFSIX-1-Cu at 298 K.

	Site A			Site B		
	$q_{A,sat}$ mol kg^{-1}	b_A $Pa^{-\nu A}$	ν_A dimensionless	$q_{B,sat}$ mol kg^{-1}	b_B $Pa^{-\nu B}$	ν_B dimensionless
C_3H_4	8	5.815E-07	1	8.4	4.451E-04	1
C_3H_6	2.4	7.168E-10	2.45	4	6.642E-05	1

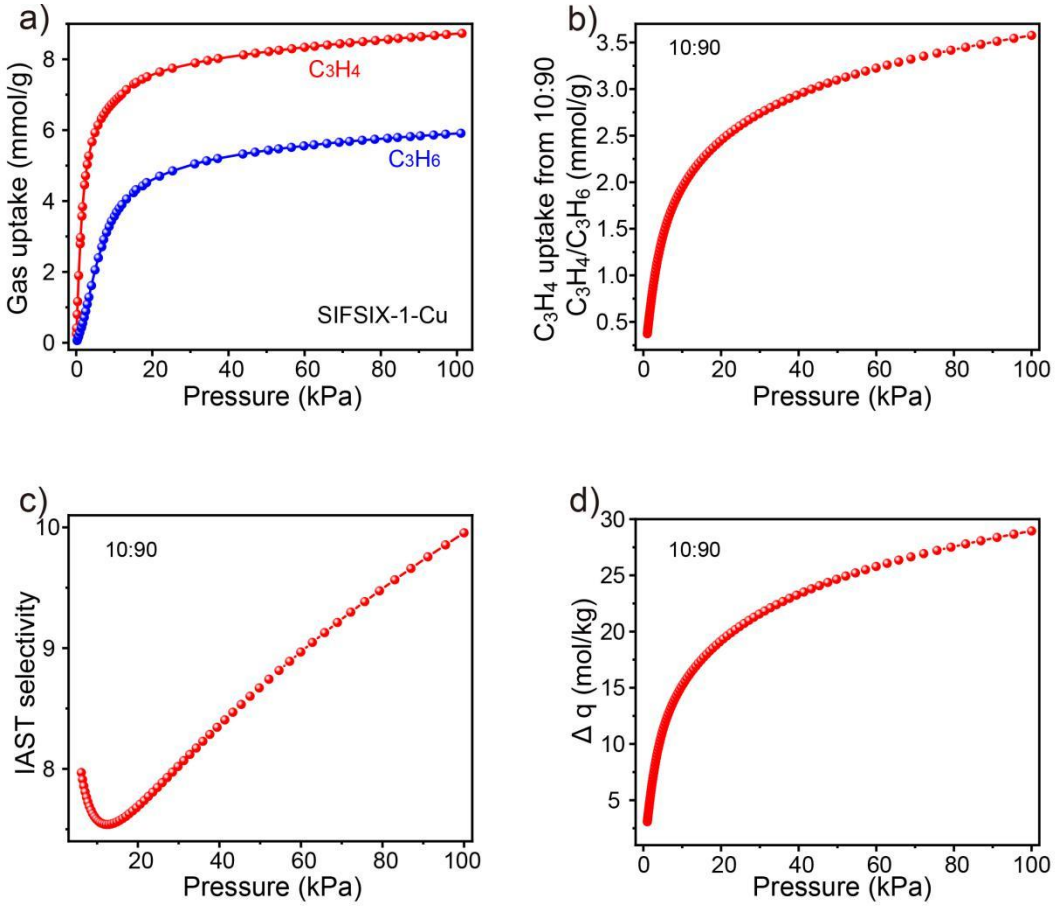

Fig. S42 (a) C_3H_4 and C_3H_6 adsorption isotherms for SIFSIX-1-Cu at 298 K. (b) IAST selectivity of SIFSIX-1-Cu towards gas mixtures of C_3H_4/C_3H_6 (10/90). (c) The adsorption isotherm of C_3H_4 from C_3H_4/C_3H_6 (10/90) mixture on SIFSIX-1-Cu. (d) IAST based separation potential for C_3H_4/C_3H_6 (10/90) mixtures.

Table S11 Unary isotherm fit parameters for C_3H_4 and C_3H_6 in SIFSIX-2-Cu-i at 298 K.

	Site A			Site B		
	$q_{A,sat}$ mol kg^{-1}	b_A Pa$^{-\nu A}$	ν_A dimensionless	$q_{B,sat}$ mol kg^{-1}	b_B Pa$^{-\nu B}$	ν_B dimensionless
C_3H_4	8.2	1.544E-06	1	3.5	1.390E-03	1
C_3H_6	1.1	1.248E-04	1	2.3	3.052E-05	1

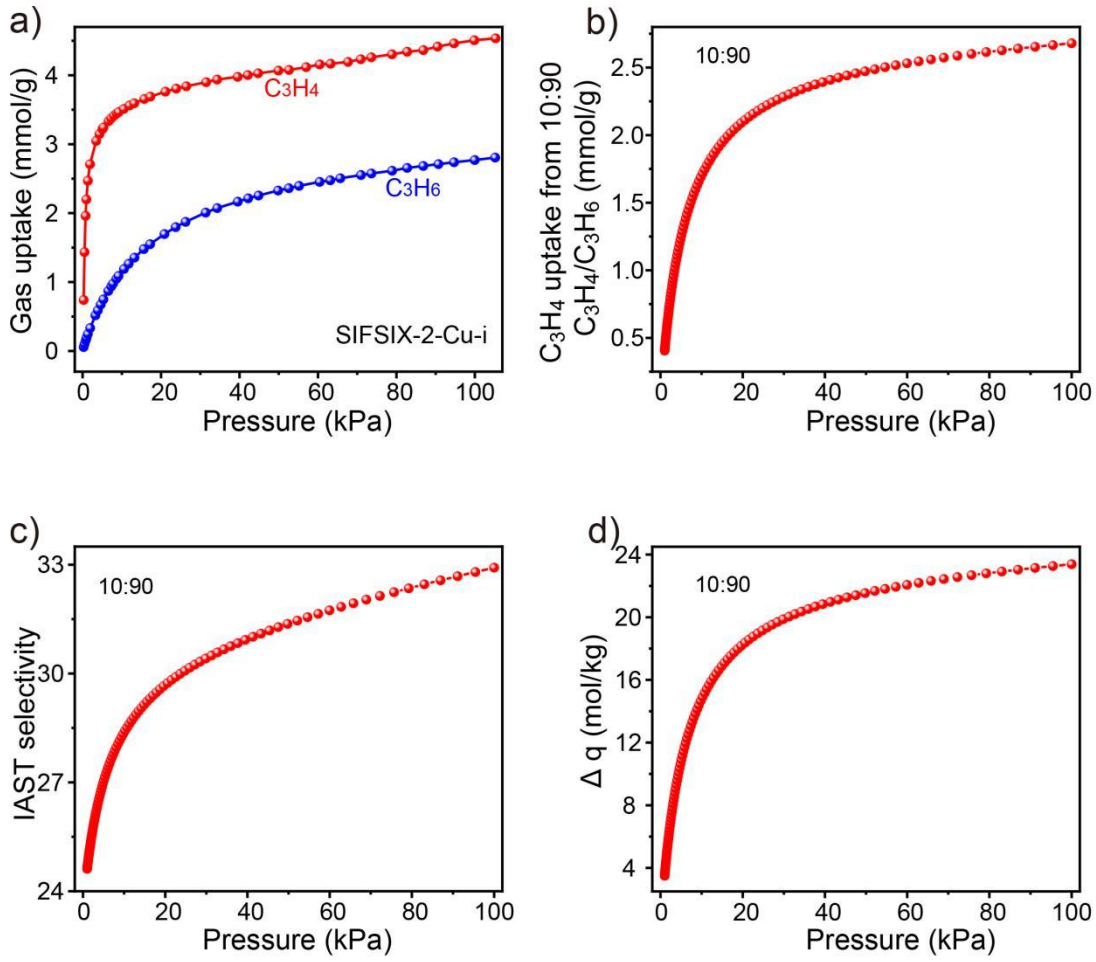

Fig. S43 (a) C_3H_4 and C_3H_6 adsorption isotherms for SIFSIX-2-Cu-i at 298 K. b) IAST selectivity of SIFSIX-2-Cu-i towards gas mixtures of C_3H_4/C_3H_6 (10/90). (c) The adsorption isotherm of C_3H_4 from C_3H_4/C_3H_6 (10/90) mixture on SIFSIX-2-Cu-i. (d) IAST based separation potential for C_3H_4/C_3H_6 (10/90) mixtures.

Table S12 Unary isotherm fit parameters for C_3H_4 and C_3H_6 in SIFSIX-3-Ni at 298 K.

	Site A			Site B		
	$q_{A,sat}$ mol kg^{-1}	b_A $Pa^{-\nu A}$	ν_A dimensionless	$q_{B,sat}$ mol kg^{-1}	b_B $Pa^{-\nu B}$	ν_B dimensionless
C_3H_4	0.6	6.453E-03	0.42	2.65	7.240E-04	2
C_3H_6	2.8	1.152E-05	1.23			

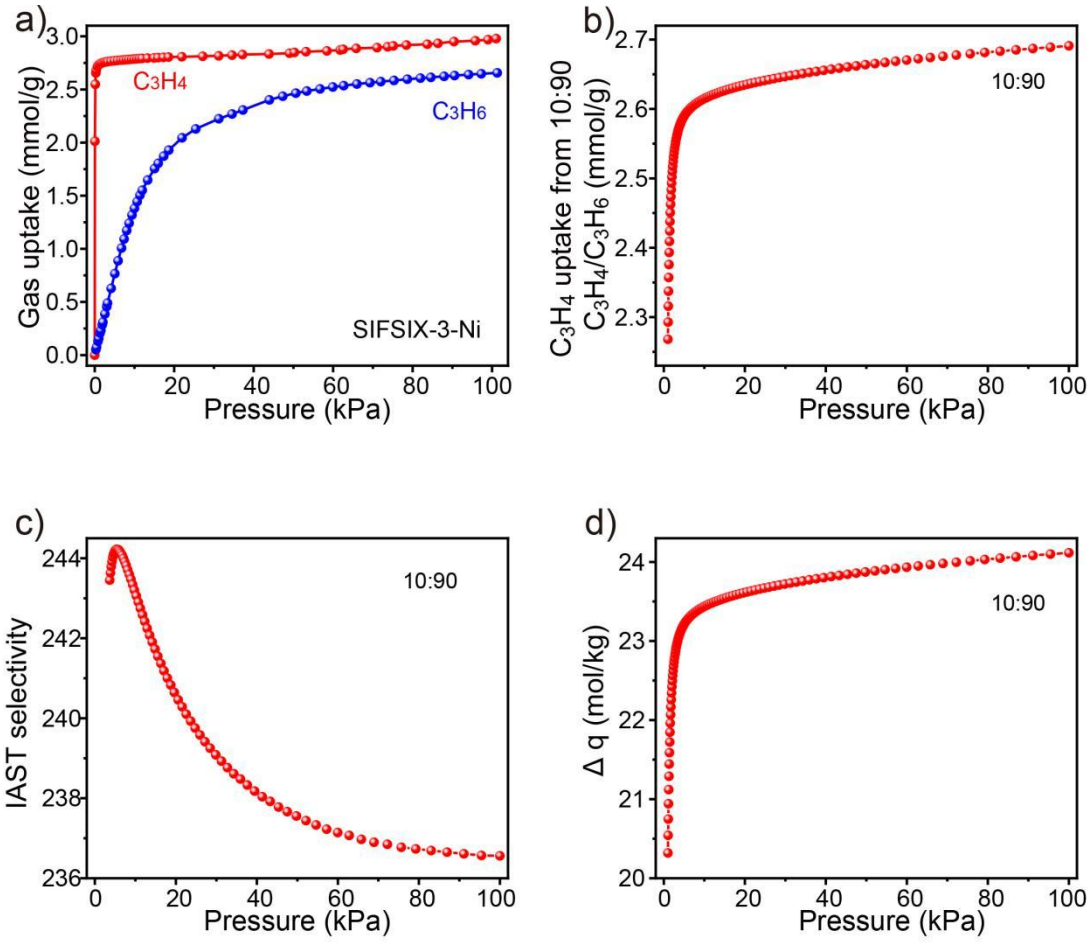

Fig. S44 (a) C_3H_4 and C_3H_6 adsorption isotherms for SIFSIX-3-Ni at 298 K. (b) IAST selectivity of SIFSIX-3-Ni towards gas mixtures of C_3H_4/C_3H_6 (10/90). (c) The adsorption isotherm of C_3H_4 from C_3H_4/C_3H_6 (10/90) mixture on SIFSIX-3-Ni. (d) IAST based separation potential for C_3H_4/C_3H_6 (10/90) mixtures.

Table S13 Unary isotherm fit parameters for C_3H_4, and C_3H_6 in ZU-62 at 298 K.

	Site A			Site B		
	$q_{A,sat}$ mol kg^{-1}	b_A Pa$^{-\nu A}$	ν_A dimensionless	$q_{B,sat}$ mol kg^{-1}	b_B Pa$^{-\nu B}$	ν_B dimensionless
C_3H_4	8	4.965E-04	0.47	2.8	3.564E-03	1
C_3H_6	0.8	3.313E-17	4.6	2.3	4.092E-05	1

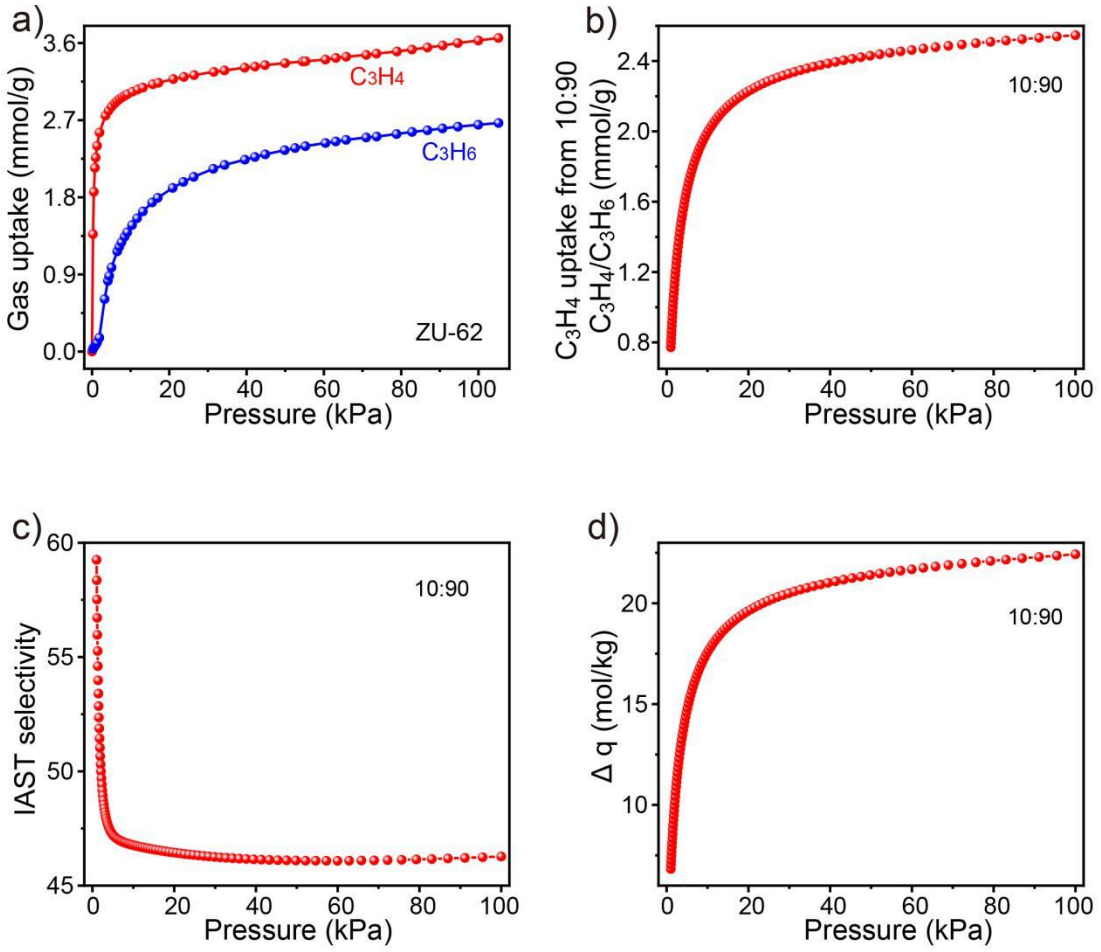

Fig. S45 (a) C_3H_4 and C_3H_6 adsorption isotherms for ZU-62 at 298 K. (b) IAST selectivity of ZU-62 towards gas mixtures of C_3H_4/C_3H_6 (10/90). (c) The adsorption isotherm of C_3H_4 from C_3H_4/C_3H_6 (10/90) mixture on ZU-62. (d) IAST based separation potential for C_3H_4/C_3H_6 (10/90) mixtures.

Table S14 Unary isotherm fit parameters for C_3H_4, and C_3H_6 in SIFSIX-14-Cu-i at 298 K.

	Site A			Site B		
	$q_{A,sat}$ mol kg^{-1}	b_A $Pa^{-\nu A}$	ν_A dimensionless	$q_{B,sat}$ mol kg^{-1}	b_B $Pa^{-\nu B}$	ν_B dimensionless
C_3H_4	1.7	1.879E-03	0.64	2.2	3.746E-18	6.35
C_3H_6	1.15	2.672E-81	18	20	9.099E-06	0.67

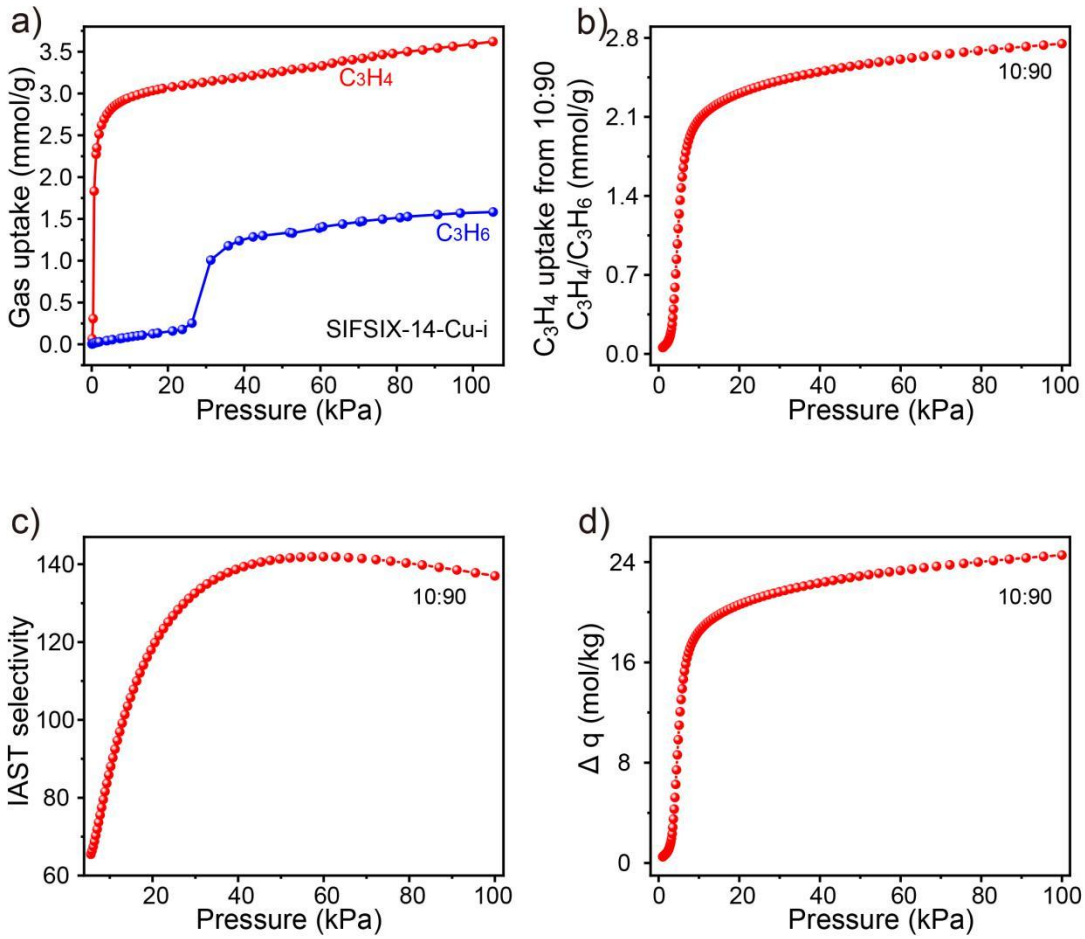

Fig. S46 (a) C_3H_4 and C_3H_6 adsorption isotherms for SIFSIX-14-Cu-i at 298 K. (b) IAST selectivity of SIFSIX-14-Cu-i towards gas mixtures of C_3H_4/C_3H_6 (10/90). (c) The adsorption isotherm of C_3H_4 from C_3H_4/C_3H_6 (10/90) mixture on SIFSIX-14-Cu-i. (d) IAST based separation potential for C_3H_4/C_3H_6 (10/90) mixtures.

Table S15 Unary isotherm fit parameters for C_3H_4, and C_3H_6 in GeFSIX-14-Cu-i at 298 K.

	Site A			Site B		
	$q_{A,sat}$ mol kg^{-1}	b_A $Pa^{-\nu A}$	ν_A dimensionless	$q_{B,sat}$ mol kg^{-1}	b_B $Pa^{-\nu B}$	ν_B dimensionless
C_3H_4	1.4	3.778E-04	1	1.9	1.316E-10	4.08
C_3H_6	1.12	1.183E-45	10	4	5.019E-05	0.65

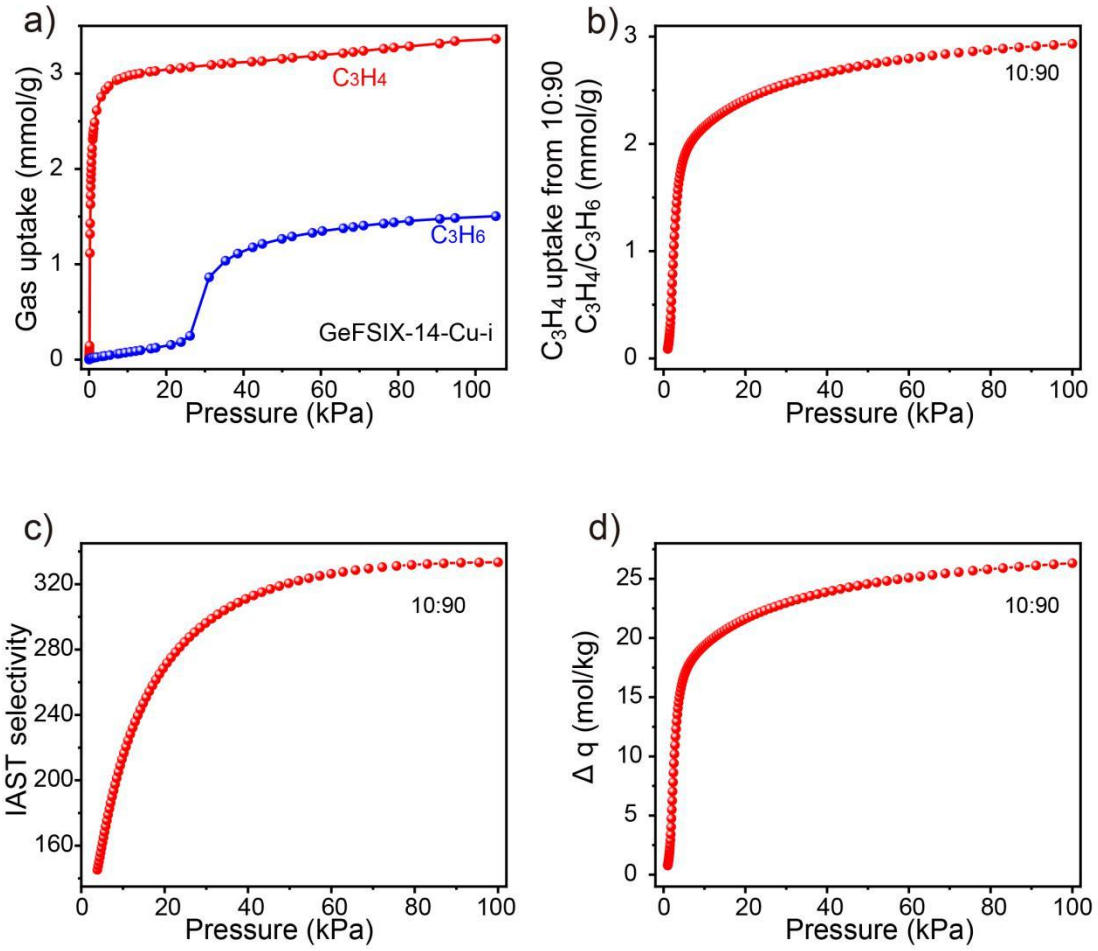

Fig. S47 (a) C_3H_4 and C_3H_6 adsorption isotherms for GeFSIX-14-Cu-i at 298 K. (b) IAST selectivity of GeFSIX-14-Cu-i towards gas mixtures of C_3H_4/C_3H_6 (10/90). (c) The adsorption isotherm of C_3H_4 from C_3H_4/C_3H_6 (10/90) mixture on GeFSIX-14-Cu-i. (d) IAST based separation potential for C_3H_4/C_3H_6 (10/90) mixtures.

Table S16 Unary isotherm fit parameters for C_3H_4, and C_3H_6 in TIFSIX-14-Cu-i at 298 K.

	Site A			Site B		
	$q_{A,sat}$ mol kg^{-1}	b_A Pa$^{-\nu A}$	ν_A dimensionless	$q_{B,sat}$ mol kg^{-1}	b_B Pa$^{-\nu B}$	ν_B dimensionless
C_3H_4	2	3.869E-04	1	1.5	8.723E-07	3
C_3H_6	1.77	4.129E-06	1.2			

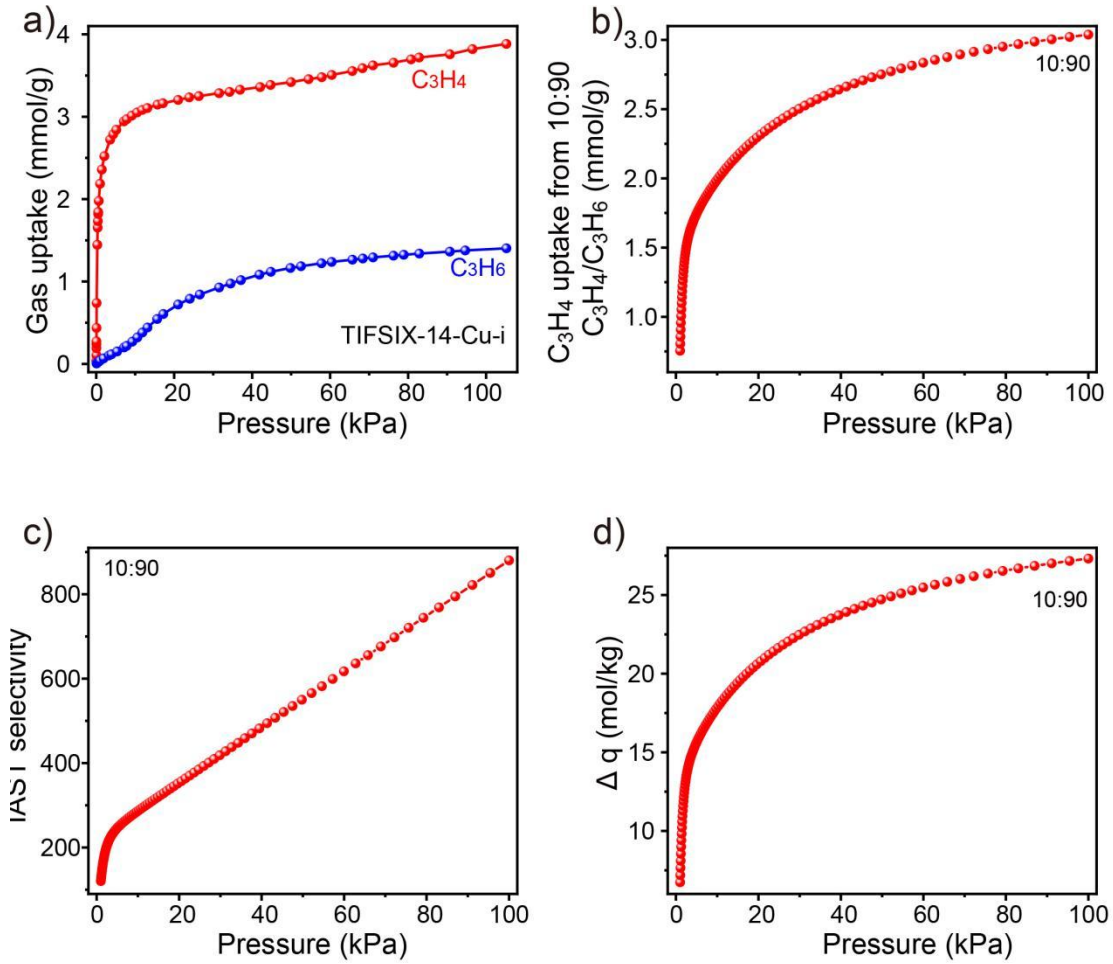

Fig. S48 (a) C_3H_4 and C_3H_6 adsorption isotherms for TIFSIX-14-Cu-i at 298 K. (b) IAST selectivity of TIFSIX-14-Cu-i towards gas mixtures of C_3H_4/C_3H_6 (10/90). (c) The adsorption isotherm of C_3H_4 from C_3H_4/C_3H_6 (10/90) mixture on TIFSIX-14-Cu-i. (d) IAST based separation potential for C_3H_4/C_3H_6 (10/90) mixtures.

Table S17 Comparison of the reported materials on C_3H_4 adsorption capacity at 1 kPa, 10 kPa and 100 kPa, and IAST selectivity towards C_3H_4/C_3H_6.

	C_3H_4 uptake (mmol/g)			Selectivity	Ref
	1 kPa	10kPa	100kPa	1:99	
ELM-12	1.83	2.54	2.74	84	[1]
ZJUT-1	0.35	1.07	2.28	70	[2]
NKMOF-11	1.78	2.12	3.10	1074	[3]
JXNU-6	0.36	2.59	5.07	3.1	[4]
NbOFFIVE-1-Ni	1.70	1.72	1.89	882	[5]
UTSA-200	2.99	3.30	3.62	20000	[6]
NKMOF-1-Ni	1.85	2.38	3.50	630.4[a]	[7]
NKMOF-1-Cu	2.03	2.35	3.33	610.5[a]	[7]
GeFSIX-dps-Cu	0.41	3.1	3.73	39.24[b]	[8]
HOF-30	1.15	1.79	2.67	7.7	[9]
Co-gallate	1.21	2.23	3.20	152	[10]
Mg-gallate	1.15	2.70	3.74	65	[10]
Ni-gallate	0.82	1.82	2.64	113	[10]

Continued

Ca-based MOF	2.60	2.79	3.01	38[c]	[11]
MIL-100 (Cr)	1.52	4.98	14.52	4.5	[6]
ZIF-8	0.13	1.44	6.28	1.9	[6]
Cu-BTC	1.47	8.17	10.48	3.2	[6]
SIFSIX-3-Zn	2.05	2.11	2.26	115	[5]
ZU-16-Co	2.45	2.47	2.58	248	[12]
TIFSIX-3-Ni	1.86	1.91	2.11	$>10^6$	[12]
FJI-W1	2.75	5.80	7.09	2.2	[35]
SIFSIX-1-Cu	2.79	6.82	8.72	8.97	[5]/This work
SIFSIX-2-Cu-i	2.21	3.48	4.51	30.58	[5,13,14]/This work
SIFSIX-3-Ni	2.73	2.79	2.97	242.06	[5]/This work
ZU-62	2.28	3.02	3.63	46.31	[14]/This work
SIFSIX-14-Cu-i	2.27	2.95	3.59	112.86	This work
TIFSIX-14-Cu-i	2.19	3.04	3.86	306.12	[13]/This work
GeFSIX-14-Cu-i	2.34	2.97	3.36	240.14	[13]/This work
ZNU-2-Si	**4.74**	**6.83**	**8.46**	**14.6/16.1[b]/19.3[d]**	**This work**
ZNU-2-Ti	**3.9**	**6.18**	**7.66**	**12.5/13.7[b]/16.2[d]**	**[15]/This work**
ZNU-2-Nb	**2.74**	**5.70**	**7.28**	**9.8/11.0[b]/13.8[d]**	**This work**
propyne/propylene: 0.5/99 [a]; 10/90 [b]; 0.5/99.5 [c]; 50/50[d]					

UTSA-200 and SIFSIX-14-Cu-i feature the same crystal structures. However, as Li et al[6] claimed, the preparation of UTSA-200 needs careful control of the reaction condition and a small amount of impurities are easily produced during the production of UTSA-200, which would greatly affect the separation performance. Thus, for clarity, UTSA-200 refers to the material with slightly better performance reported by Li[8] and SIFSIX-14-Cu-i refers to our synthesized material in this work which is also true in the main text.

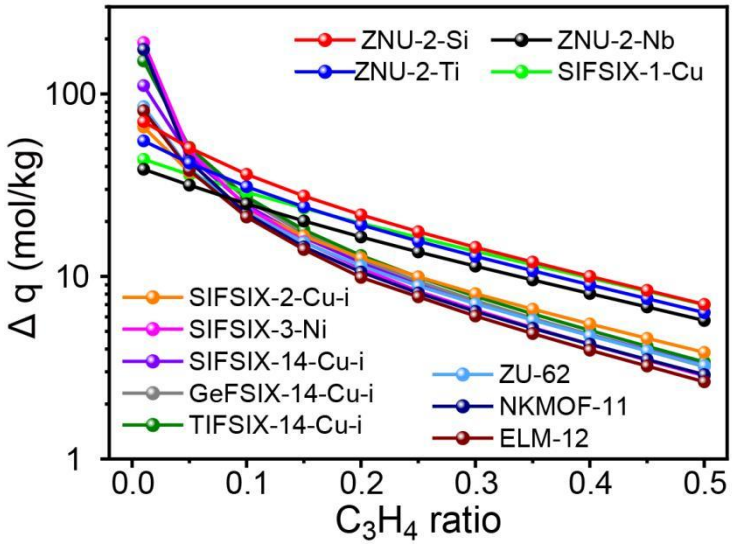

Fig. S49 Comparison of the IAST based separation potential for C_3H_4/C_3H_6 mixtures in different proportions in ZNU-2 and reported top performing MOFs.

Table S18 Comparison of the reported materials on C_3H_4 adsorption enthalpy (Q_{st}).

	Q_{st} (kJ/mol)	Ref
ELM-12	60.6	[1]
ZU-62	121.9/71.0	[14, 11]
SIFSIX-2-Cu-i	82.0/46.0	[5,14]
ZJUT-1	33.6	[2]
NKMOF-11	85.0	[3]
JXNU-6	40.0	[4]
SIFSIX-1-Cu	37.2	[5]
SIFSIX-3-Ni	68.0	[5]
UTSA-200	55.3	[6]
NKMOF-1-Ni	65.1	[11]
NKMOF-1-Cu	67.2	[11]
Co-gallate	82.1	[10]
Mg-gallate	66.8	[10]
Ni-gallate	84.4	[10]
Ca-based MOF	55.4	[11]
Cu-BTC	46.0	[16]
FJI-W1	61.7	[35]
ZNU-2-Si	43.3	this work
ZNU-2-Ti	43.0	[1]/this work
ZNU-2-Nb	41.6	this work

IV Crystallography based DFT calculation

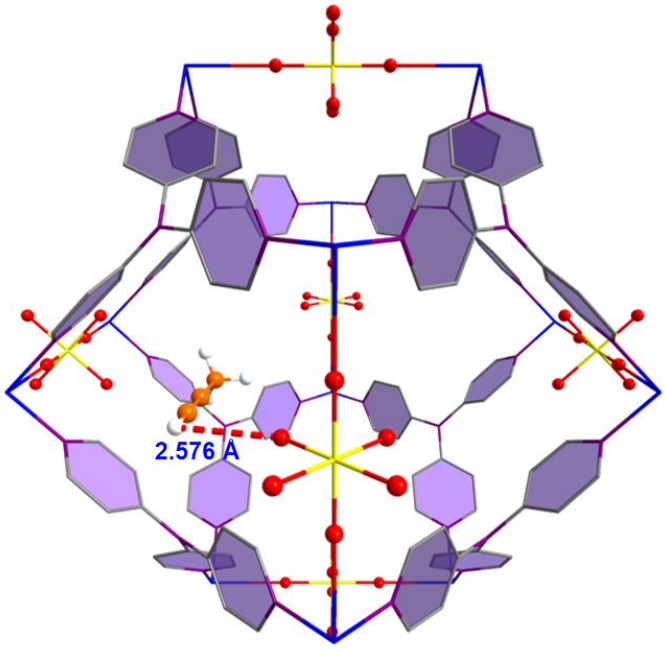

ΔE = -39.35 kJ/mol

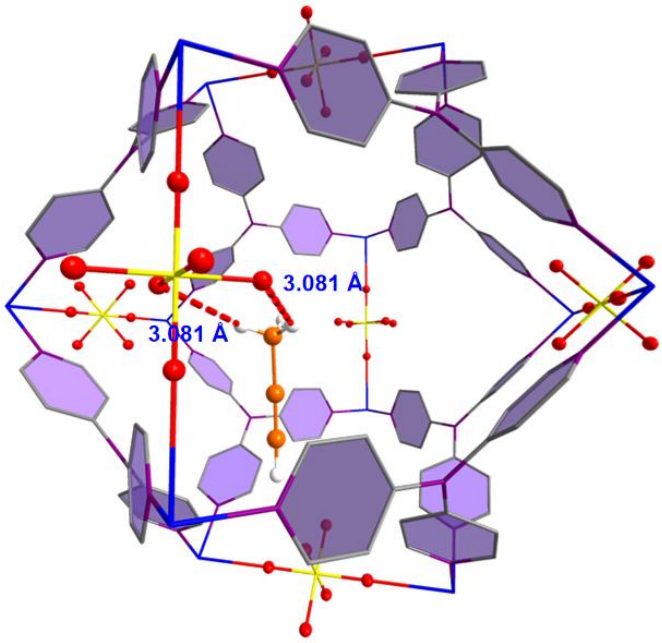

ΔE = -35.87 kJ/mol

Fig. S50 DFT calculated interaction energy of ZNU-2-Si and C_3H_4 with two similar configurations. The one with alkynyl C-H end closer to the interlaced channel (above) display higher binding energy (-39.35 kJ/mol) than the other one (below).

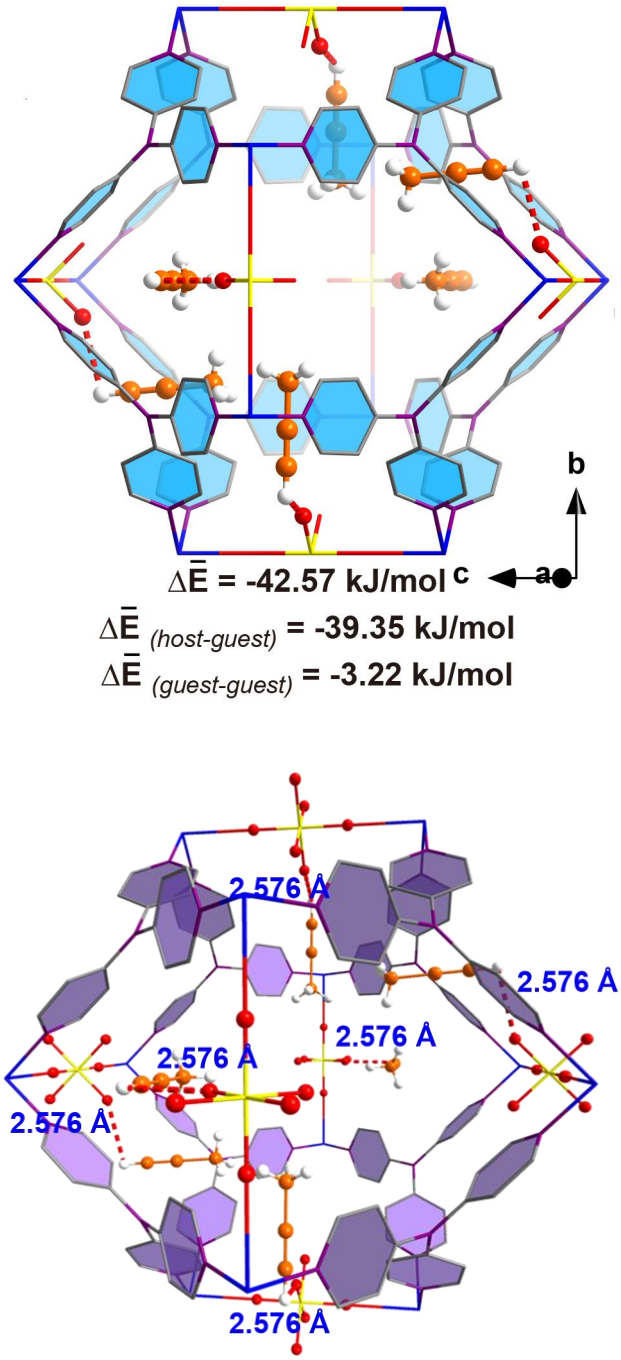

Fig. S51 DFT calculated interaction energy of ZNU-2-Si and gas molecules under the situation that six C_3H_4 located in a cage.

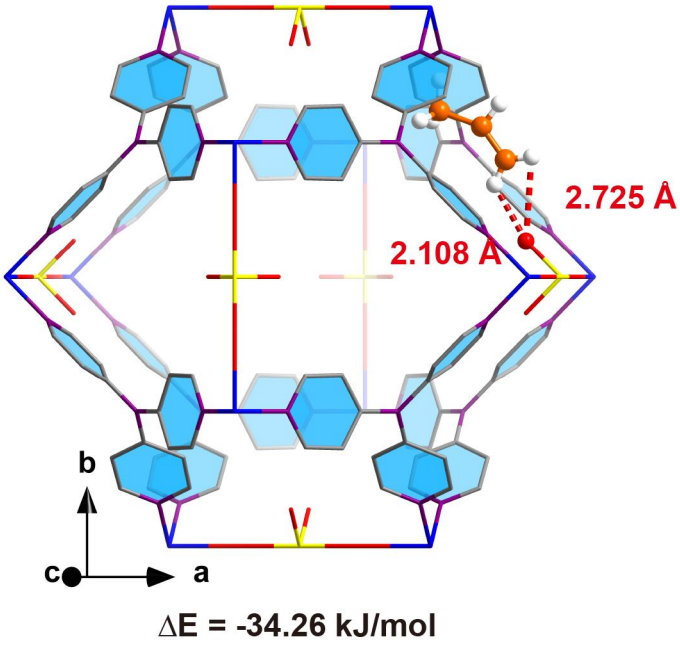

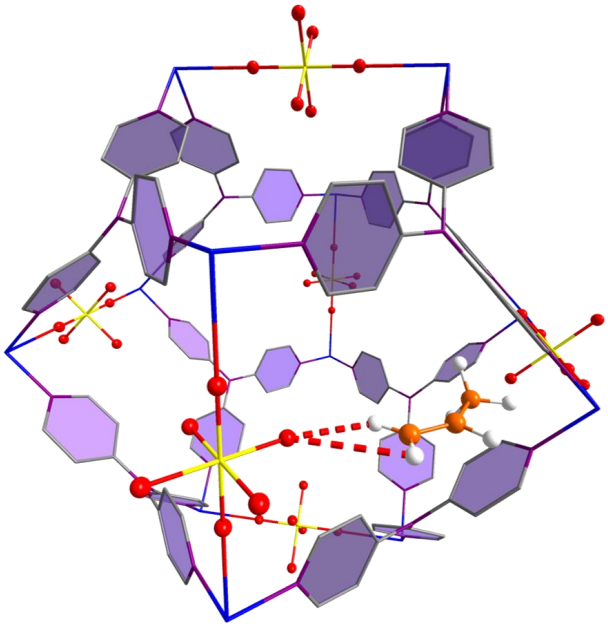

Fig. S52 DFT calculated interaction energy of ZNU-2-Si and gas molecules under the situation that a C_3H_6 located in a cage.

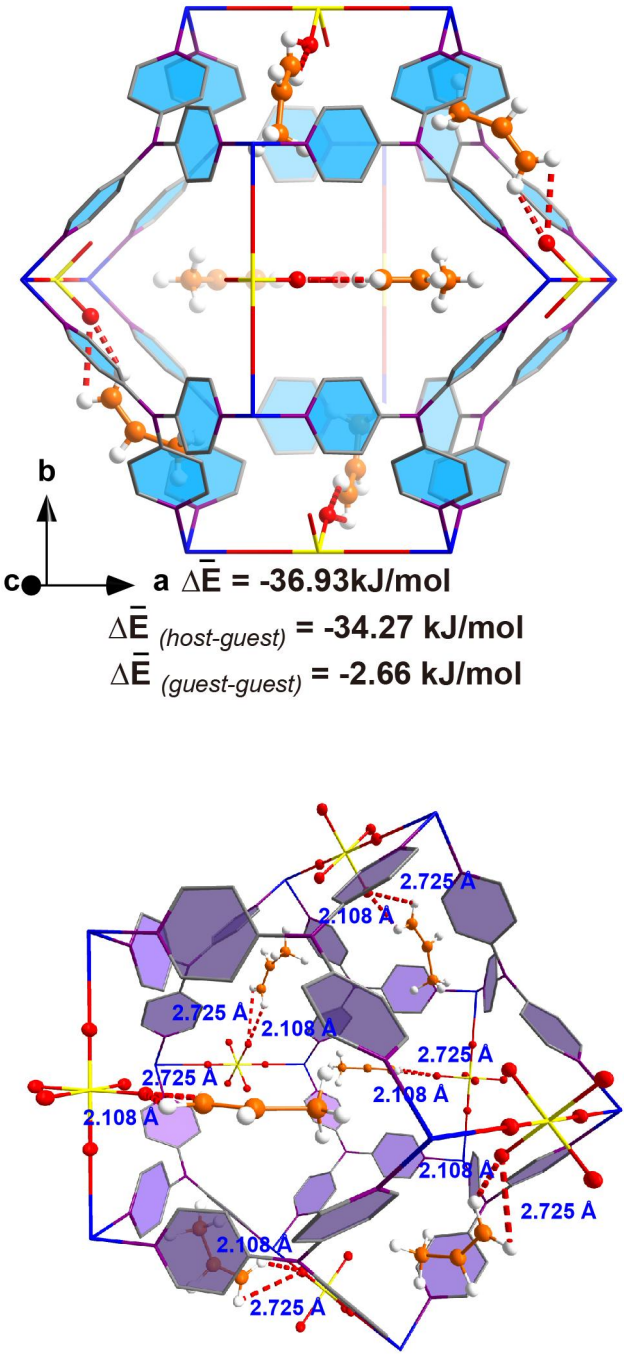

Fig. S53 DFT calculated interaction energy of ZNU-2-Si and gas molecules under the situation that six C_3H_6 located in a cage.

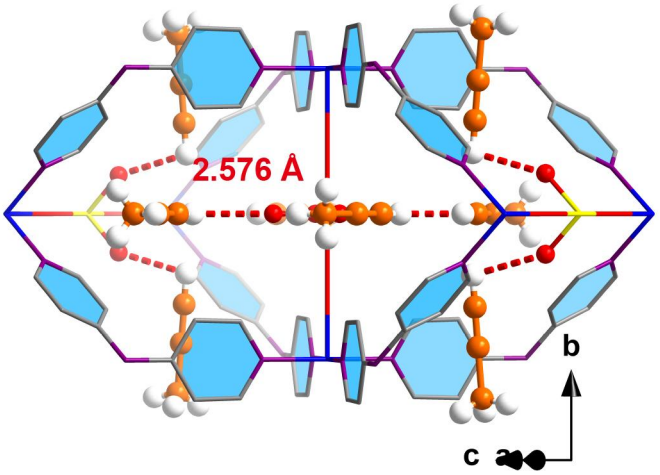

$\Delta\bar{E}$ = -44.25 kJ/mol

$\Delta\bar{E}_{(host\text{-}guest)}$ = -39.36 kJ/mol

$\Delta\bar{E}_{(guest\text{-}guest)}$ = -4.89 kJ/mol

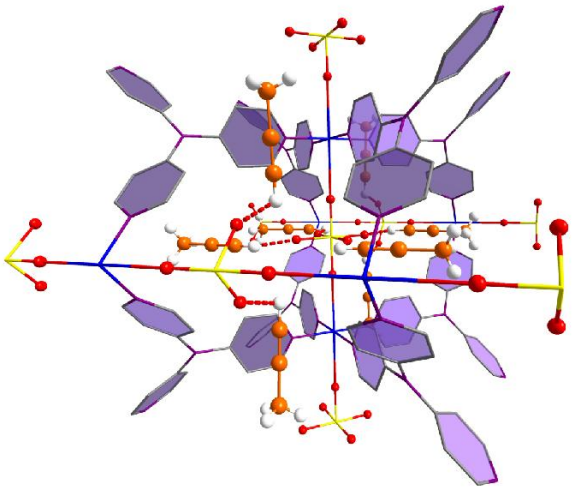

Fig. S54 DFT calculated interaction energy of ZNU-2-Si and gas molecules under the situation that 8 C_3H_4 molecules located near two neighbouring two interlaced channels.

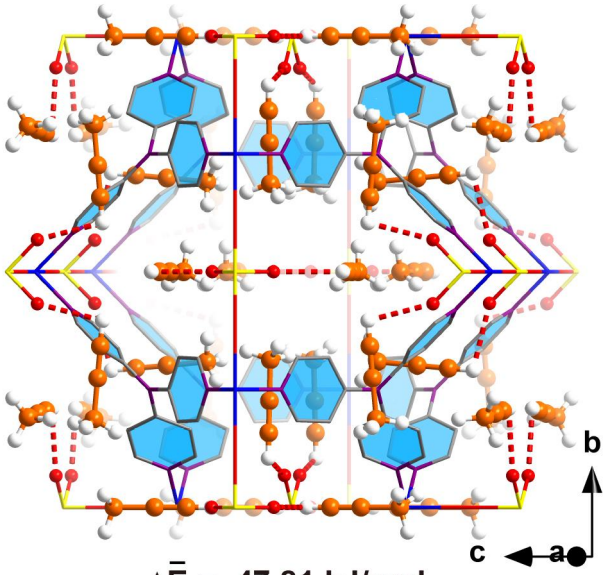

Fig. S55 DFT calculated interaction energy of ZNU-2-Si and gas molecules under the situation that 8 C_3H_4 molecules located near two neighbouring two interlaced channels.

V GCMC simulation based DFT calculation

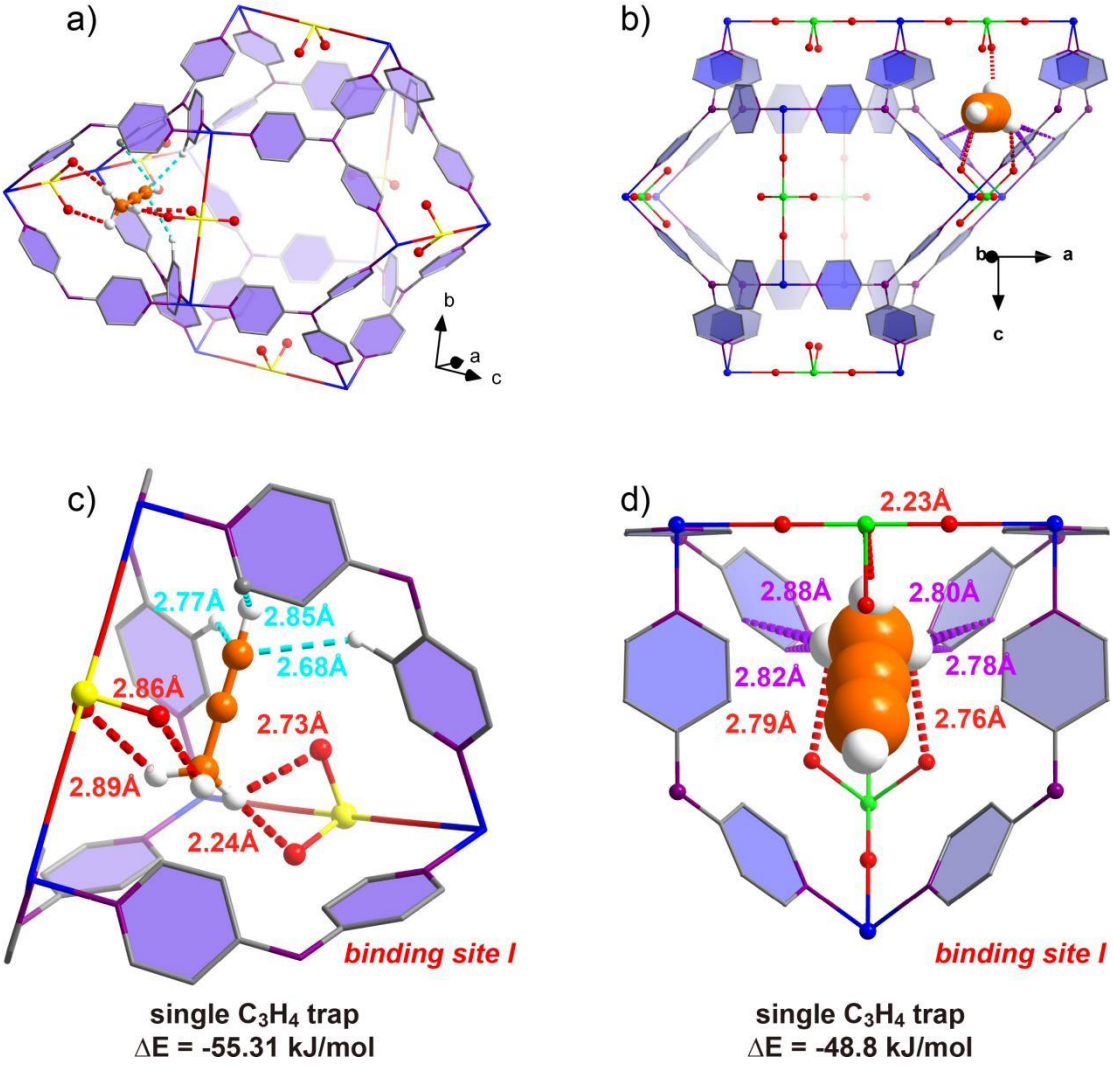

Fig. S56 The DFT-D optimized adsorption configuration of C_3H_4 in the first binding site in the channel among four cages (Left: ZNU-2-Si (a, c); Right: ZNU-2-Ti (b, d)).

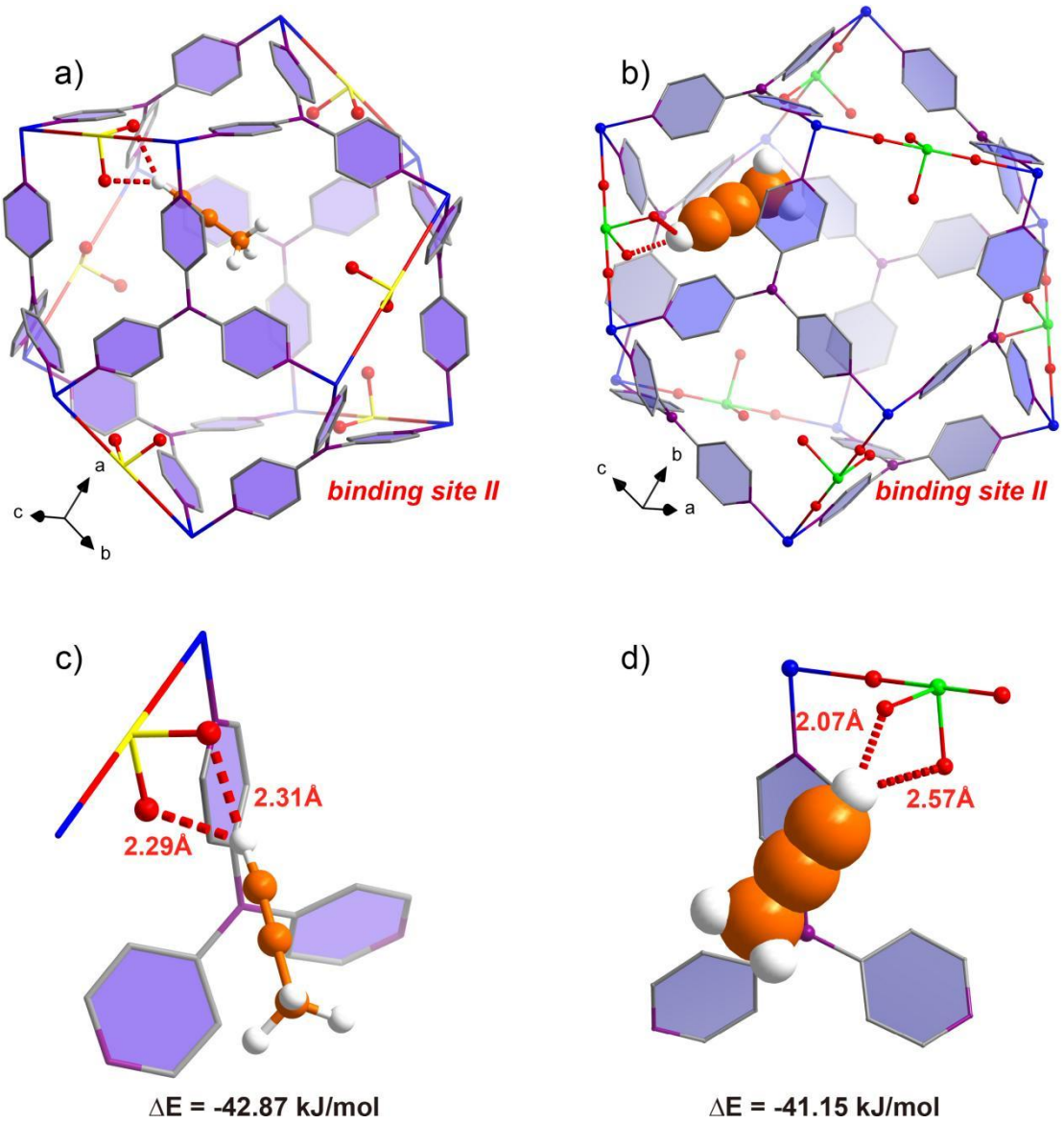

Fig. S57 The DFT-D optimized adsorption configuration of one C_3H_4 in the second binding site in the cage (Left: ZNU-2-Si (a,c); Right: ZNU-2-Ti (b, d)).

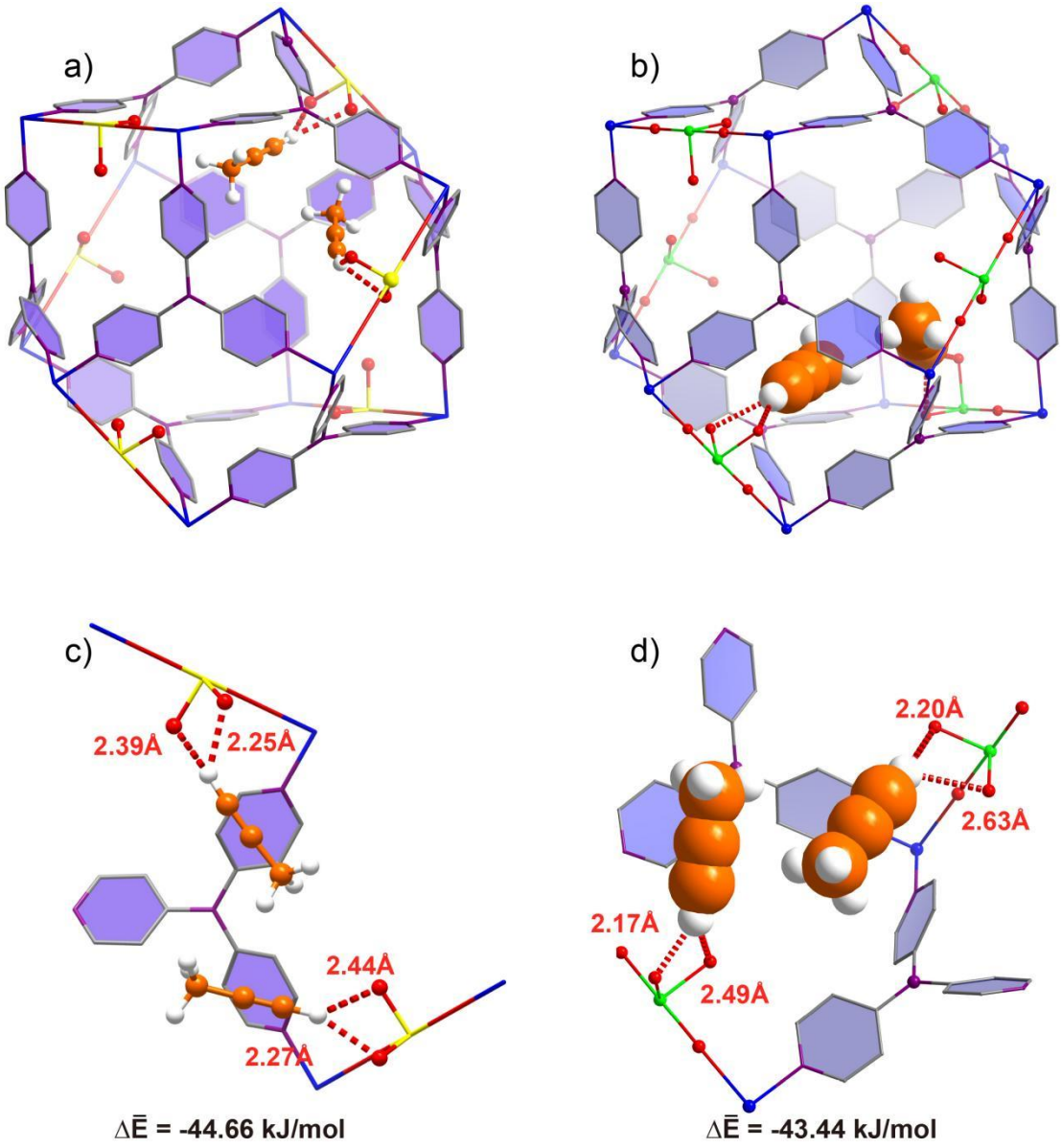

Fig. S58 The DFT-D optimized adsorption configuration of two C_3H_4 molecules in the cage (Left: ZNU-2-Si (a,c); Right: ZNU-2-Ti (b, d)).

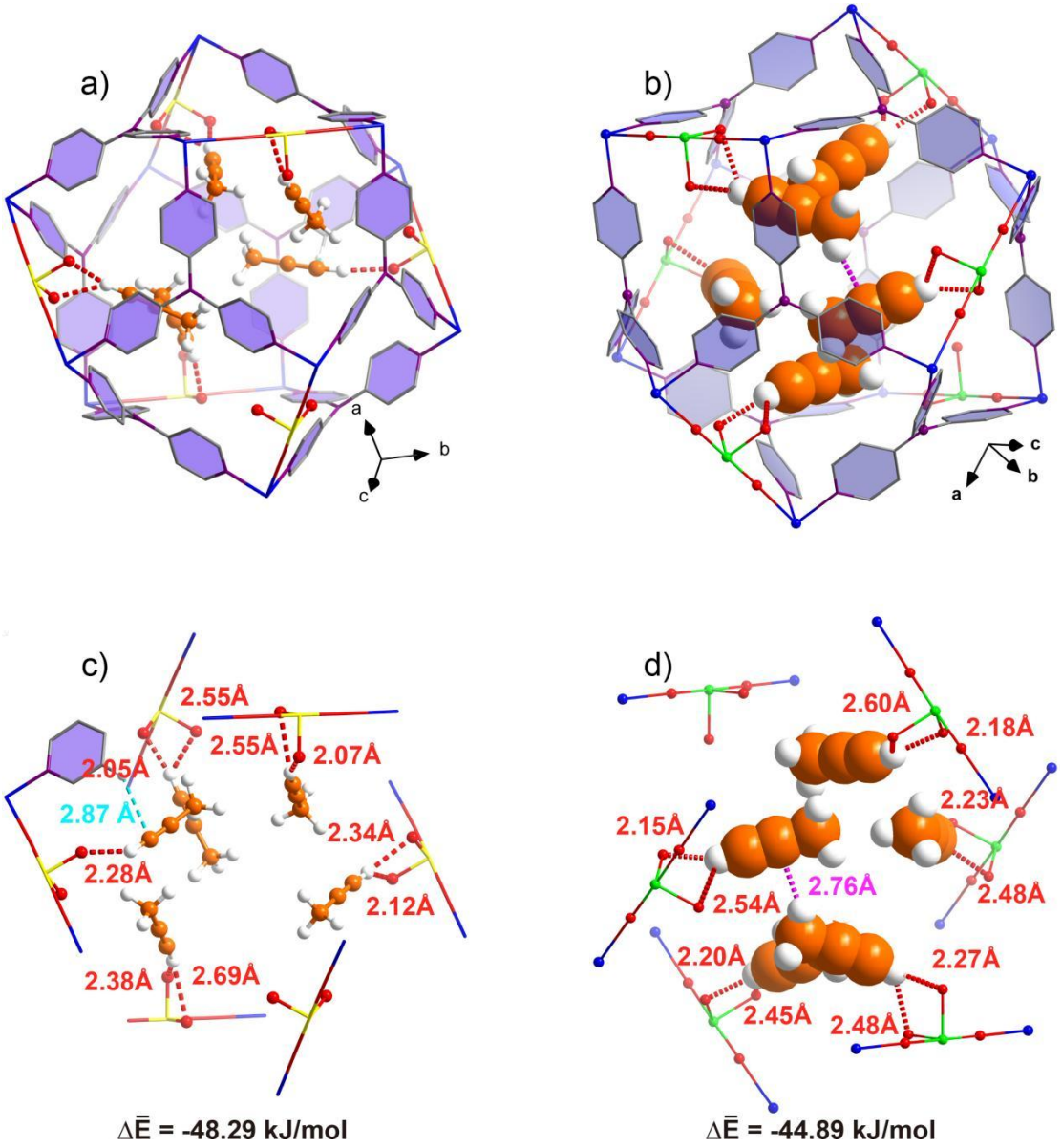

Fig. S59 The DFT-D optimized adsorption configuration of five C_3H_4 molecules in the cage (Left: ZNU-2-Si (a,c); Right: ZNU-2-Ti (b, d)).

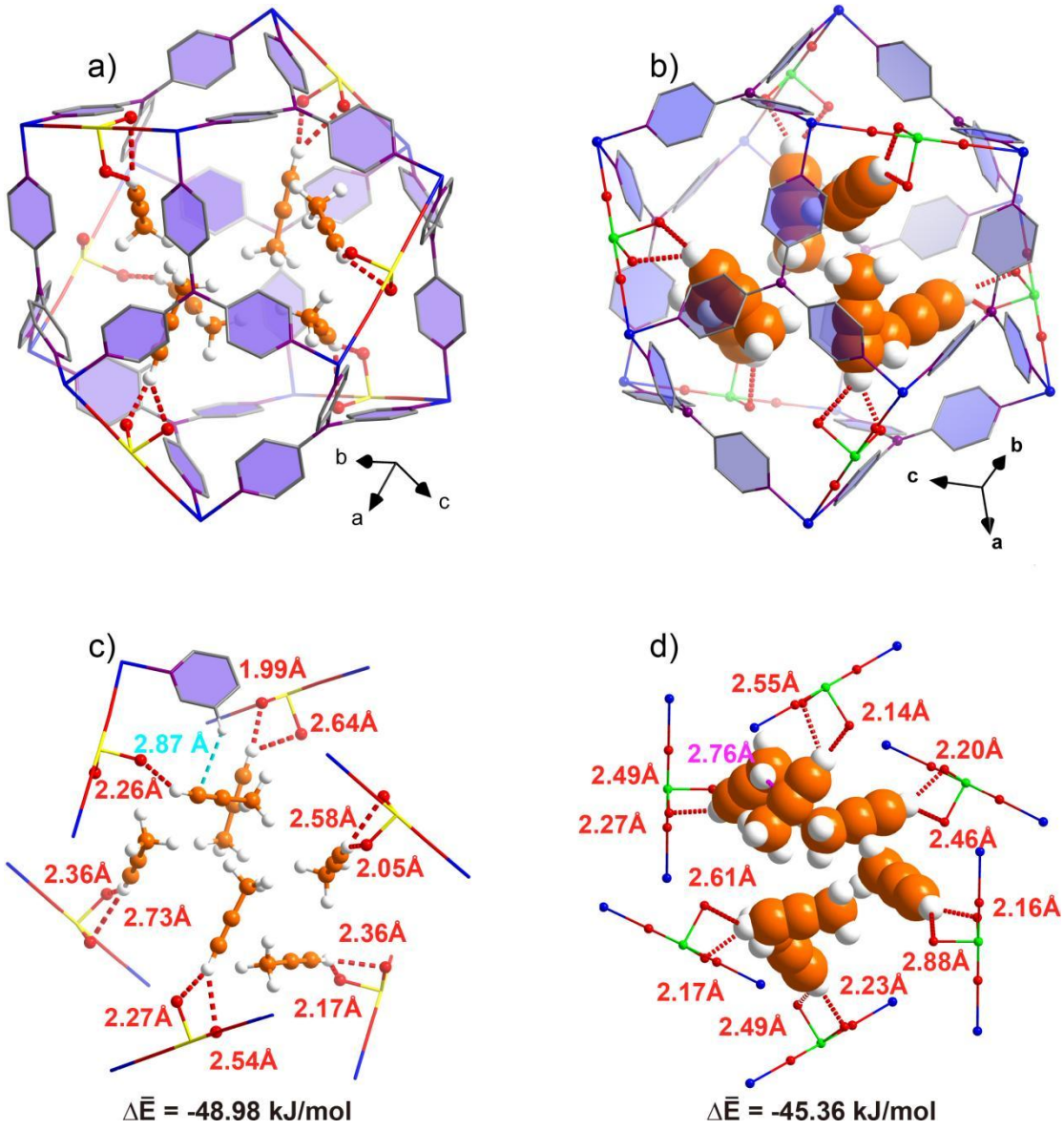

Fig. S60 The DFT-D optimized adsorption configuration of six C_3H_4 molecules in the cage (Left: ZNU-2-Si (a,c); Right: ZNU-2-Ti (b, d)).

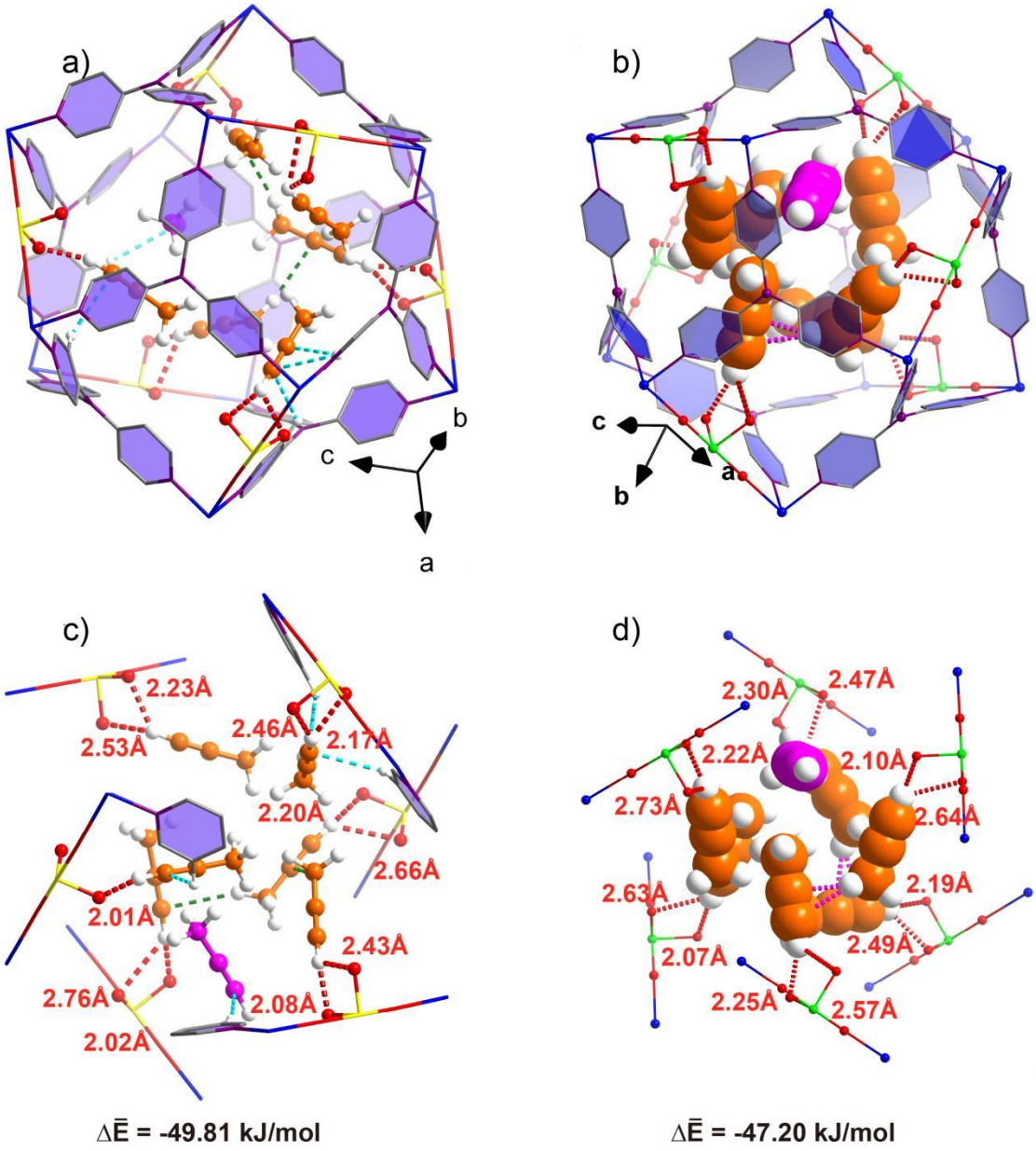

Fig. S61 The DFT-D optimized adsorption configuration of seven C_3H_4 molecules in the cage (Left: ZNU-2-Si (a,c); Right: ZNU-2-Ti (b, d)).

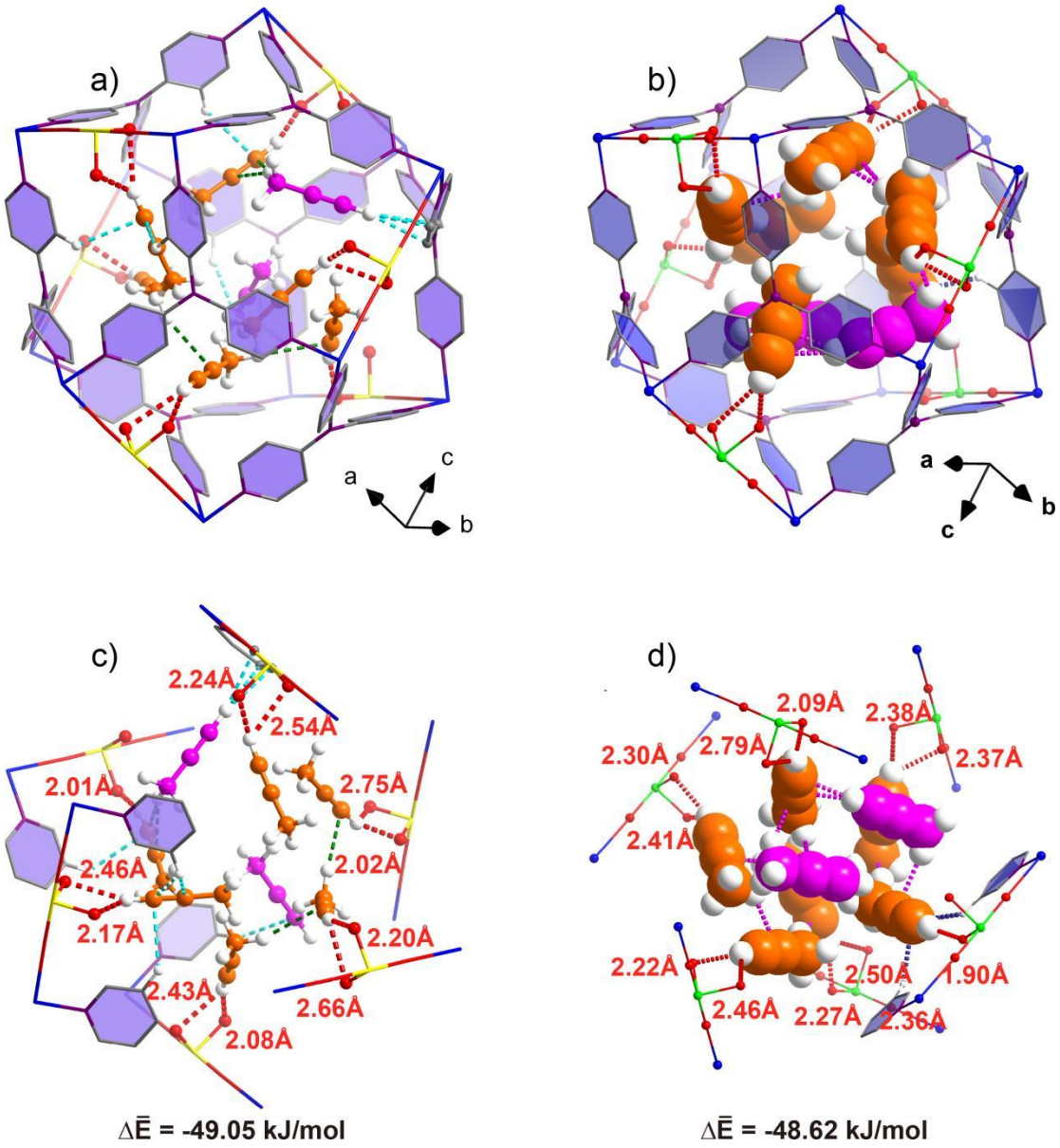

Fig. S62 The DFT-D optimized adsorption configuration of eight C_3H_4 molecules in the cage (Left: ZNU-2-Si (a,c); Right: ZNU-2-Ti (b, d)).

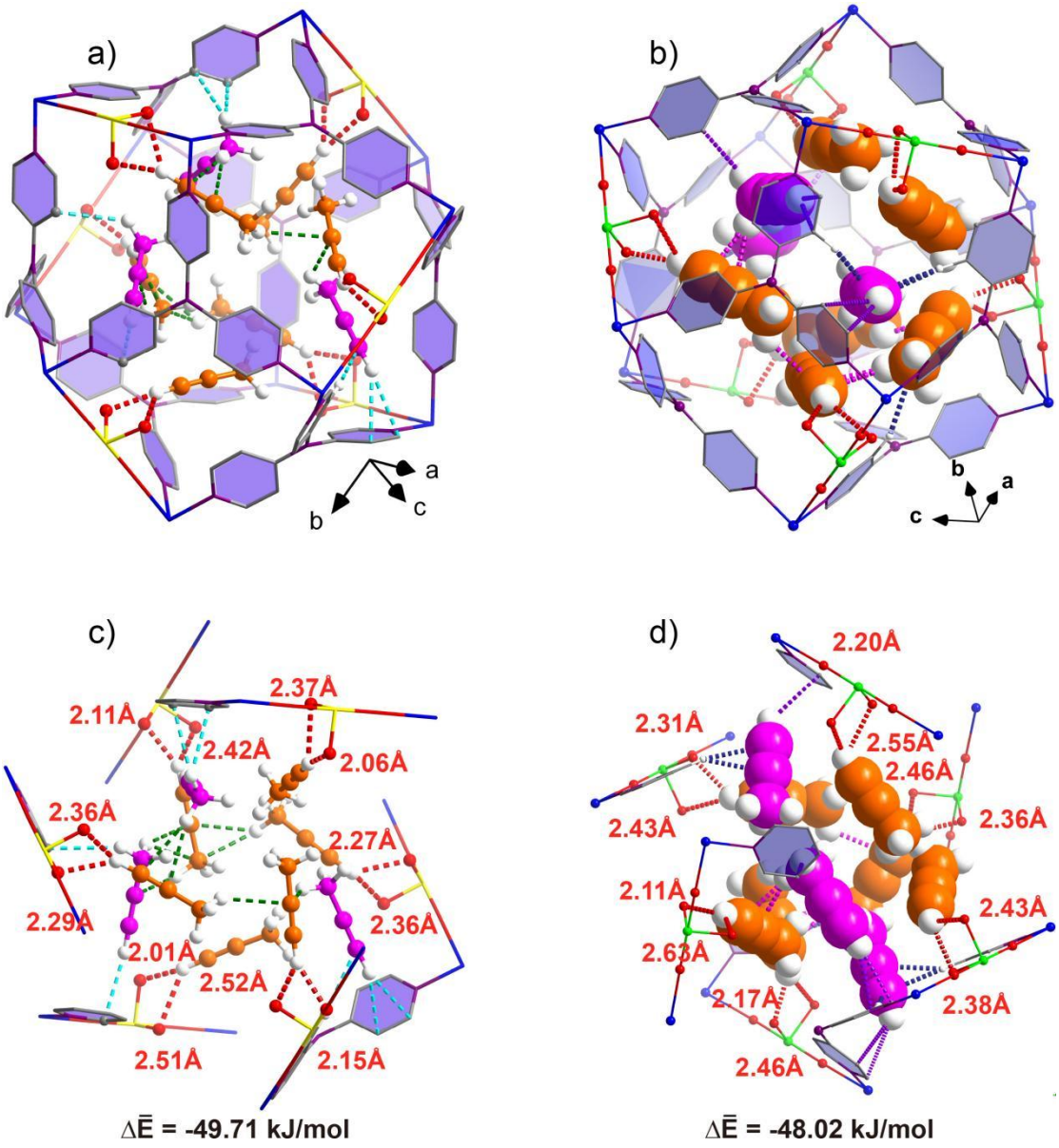

Fig. S63 The DFT-D optimized adsorption configuration of nine C_3H_4 molecules in the cage (Left: ZNU-2-Si (a,c); Right: ZNU-2-Ti (b, d)).

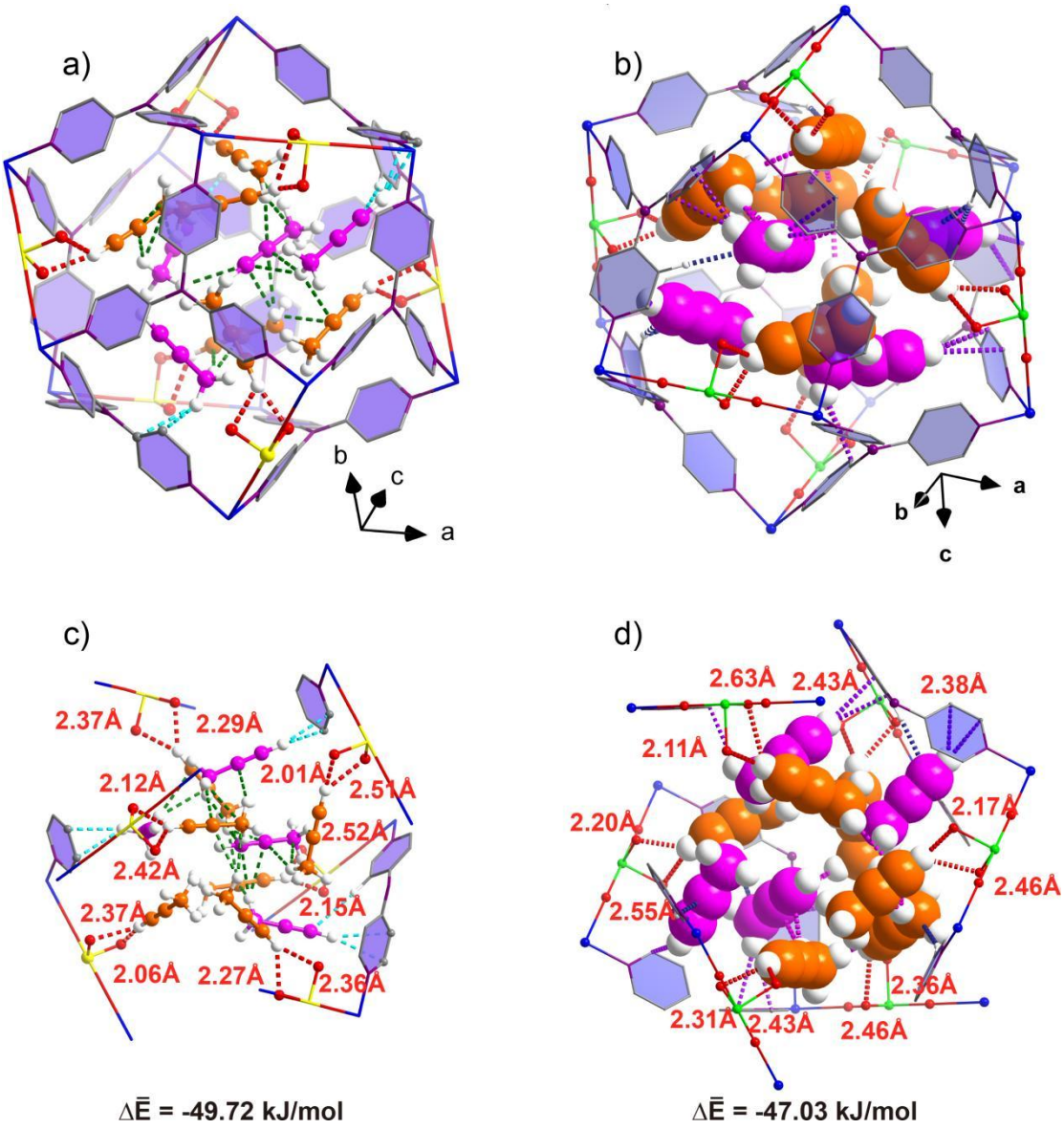

Fig. S64 The DFT-D optimized adsorption configuration of ten C_3H_4 molecules in the cage (Left: ZNU-2-Si (a,c); Right: ZNU-2-Ti (b, d)).

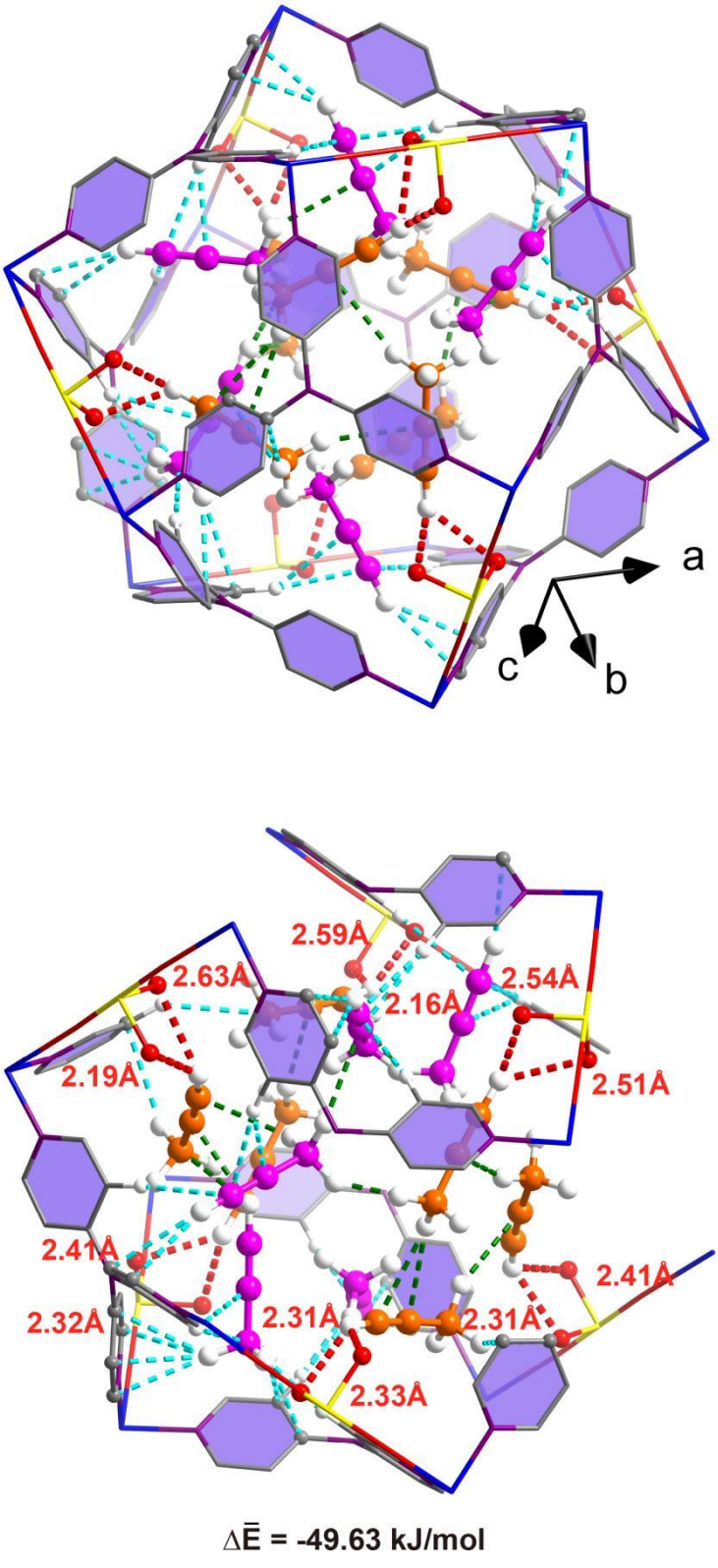

Fig. S65 The DFT-D optimized adsorption configuration of eleven C_3H_4 molecules in the cage of ZNU-2-Si.

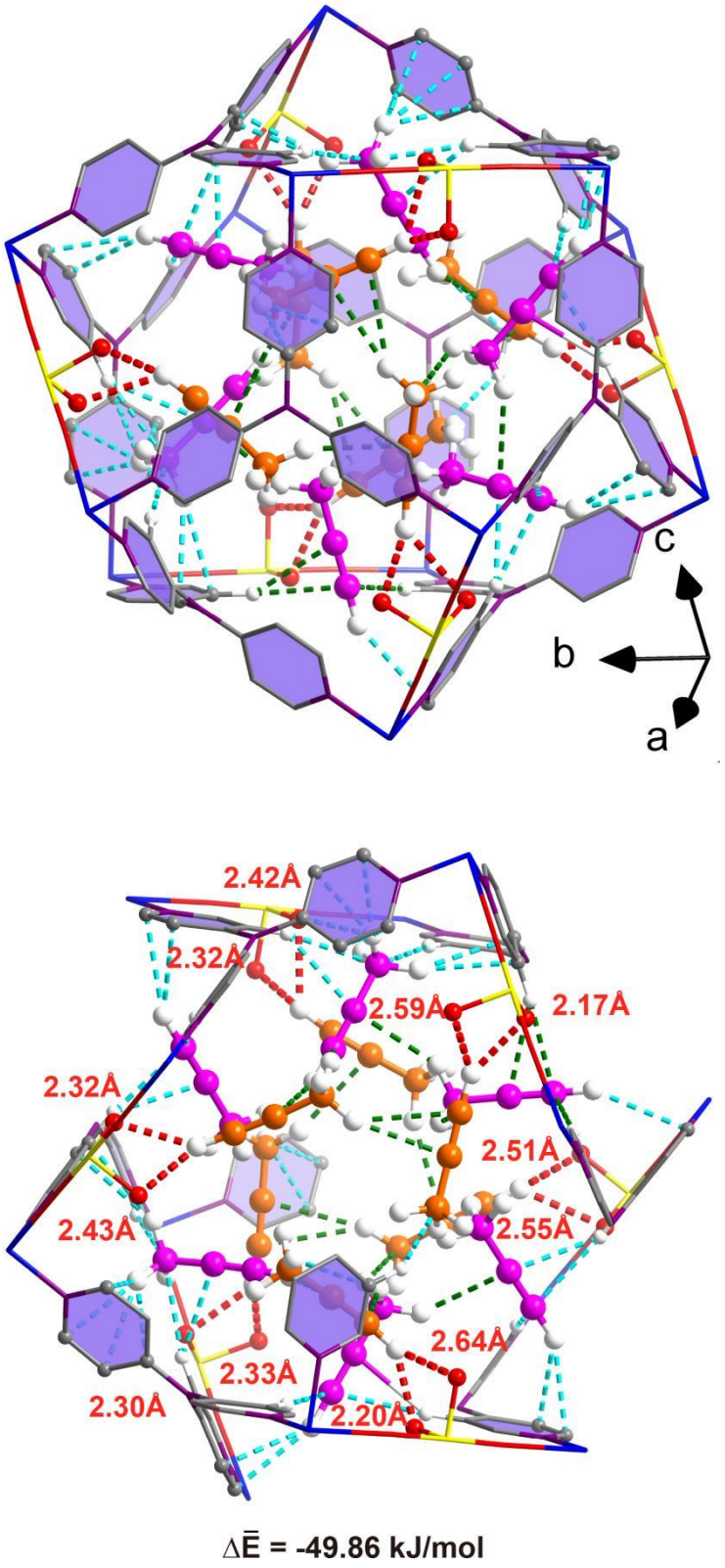

Fig. S66 The DFT-D optimized adsorption configuration of twelve C_3H_4 molecules in the cage of ZNU-2-Si.

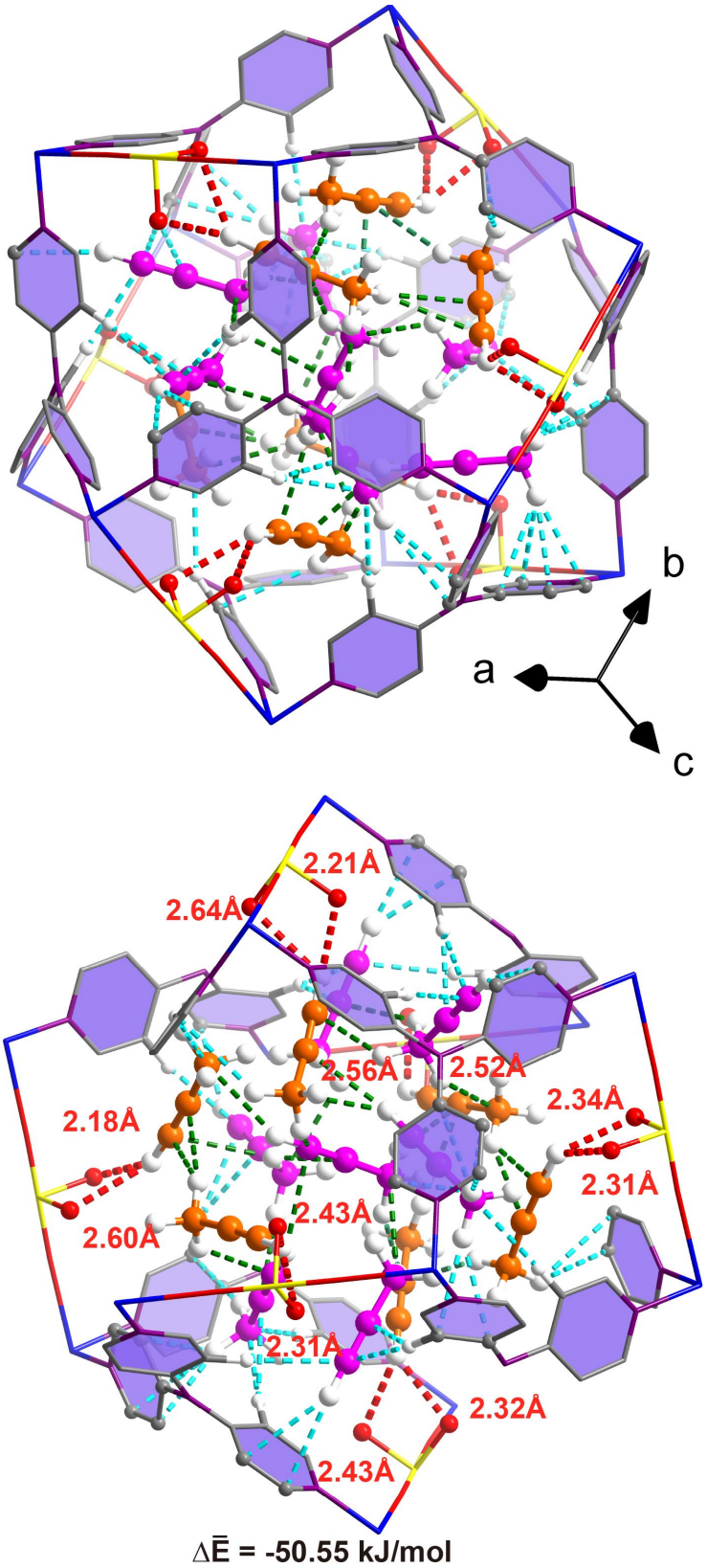

Fig. S67 The DFT-D optimized adsorption configuration of thirteen C_3H_4 molecules in the cage of ZNU-2-Si.

Table S19 Comparison of the average binding energy of C_3H_4 molecules absorbed in ZNU-2-Si and ZNU-2-Ti.

Number of C_3H_4 molecular	**Average binding energy (kJ/mol)**	
	ZNU-2-Si	**ZNU-2-Ti**
1 (binding site I)	-55.31	-48.78
1 (binding site II)	-42.87	-41.15
2	-44.66	-43.44
5	-48.29	-44.88
6	-48.98	-45.35
7	-49.81	-47.20
8	-49.05	-48.62
9	-49.71	-48.01
10	-49.72	-47.03
11	-49.63	-
12	-49.86	-
13	-50.55	-

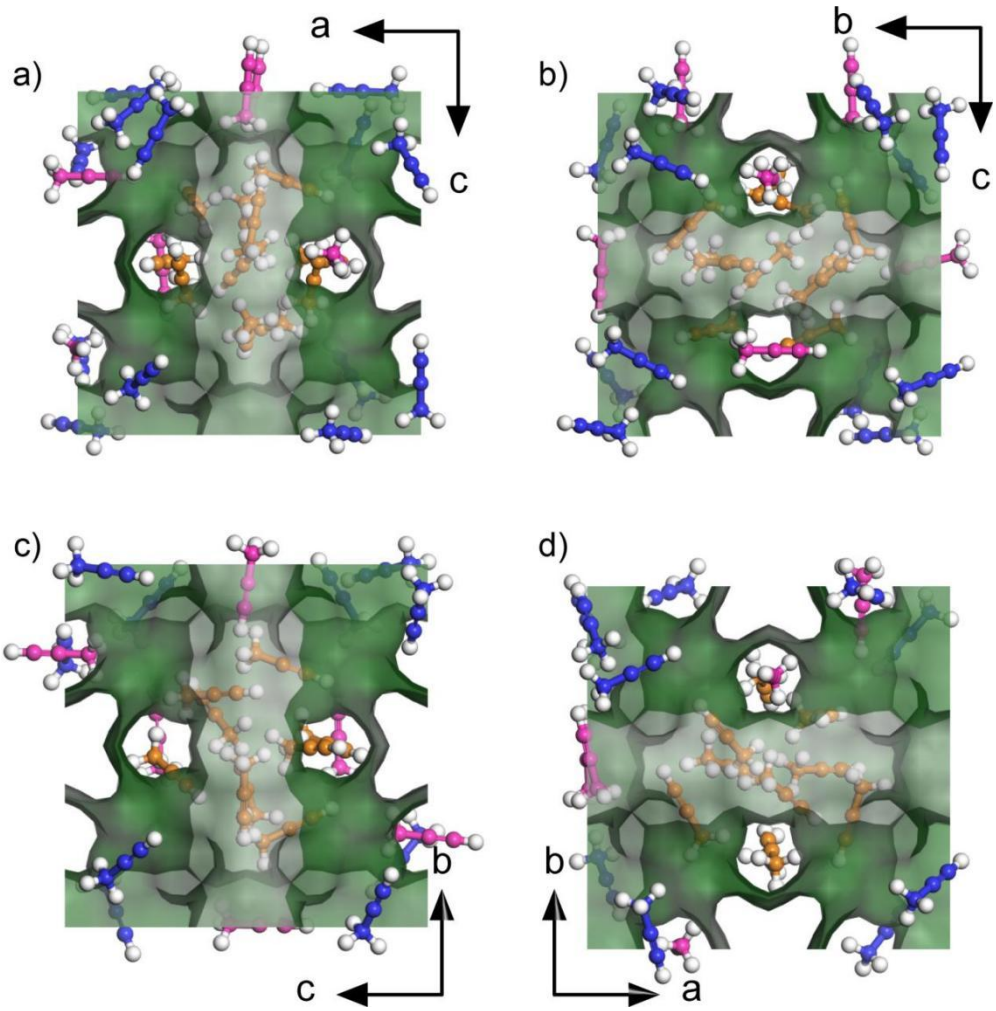

Fig. S68 The GCMC optimized adsorption configuration of saturated C_3H_4 molecules in the unit cell of ZNU-2-Si (a, b) and ZNU-2-Ti (c, d)

An unit cell is consisted of six channels and two cages (there is a complete cage in the middle of the cell and eight corners from eight different cages; each corner accounts for one-eighth of a cage). Pink C_3H_4 molecules: located in the channel (the first binding site); Orange C_3H_4 molecules: located in the cage (the second binding site); Blue C_3H_4 molecules: in the other corner-cages (the second binding site).

The simulated uptake capacity of C_3H_4 molecules in an unit cell in ZNU-2-Si is 30, equals to 5 C_3H_4 for each SiF_6^{2-}, while in ZNU-2-Ti is 25, equals to 4.17 C_3H_4 for each TiF_6^{2-}. The results calculated from GCMC are approximate to the experimental C_3H_4/MFSIX ratio values of 4.54/4.26 (Fig. S21).

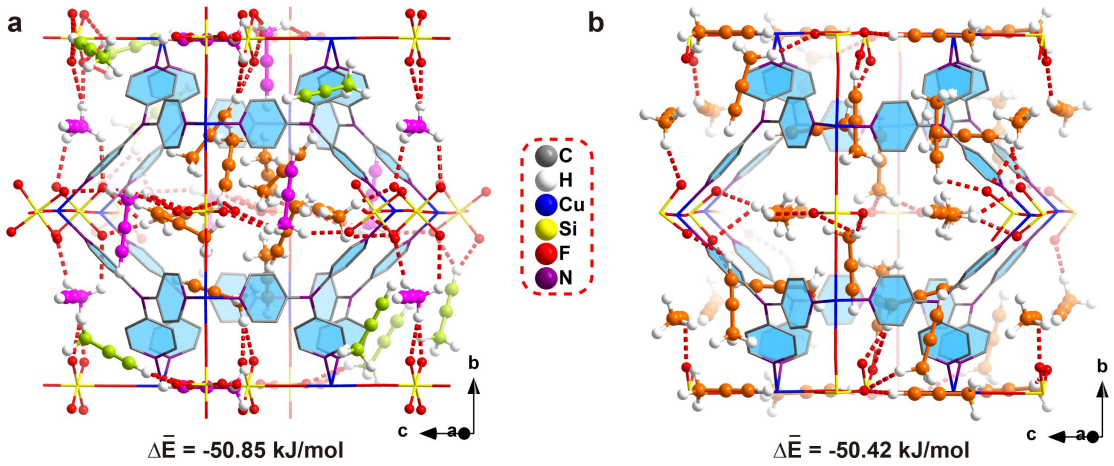

Fig. S69. The GCMC optimized adsorption configuration of 24 C_3H_4 molecules in the unit cell of ZNU-2-Si.(a) a holistic view; (b) Viewed around a cage; (c-e) Viewed around the interlaced channel.

As described above, An unit cell is consisted of six channels and two cages (there is a complete cage in the middle of the cell and eight corners from eight different cages; each corner accounts for one-eighth of a cage). Pink C_3H_4 molecules: located in the interlaced channel (the first binding site); Orange C_3H_4 molecules: located in the cage (the second binding site); Green C_3H_4 molecules: in the other corner-cages (the second binding site).

VI MD simulation

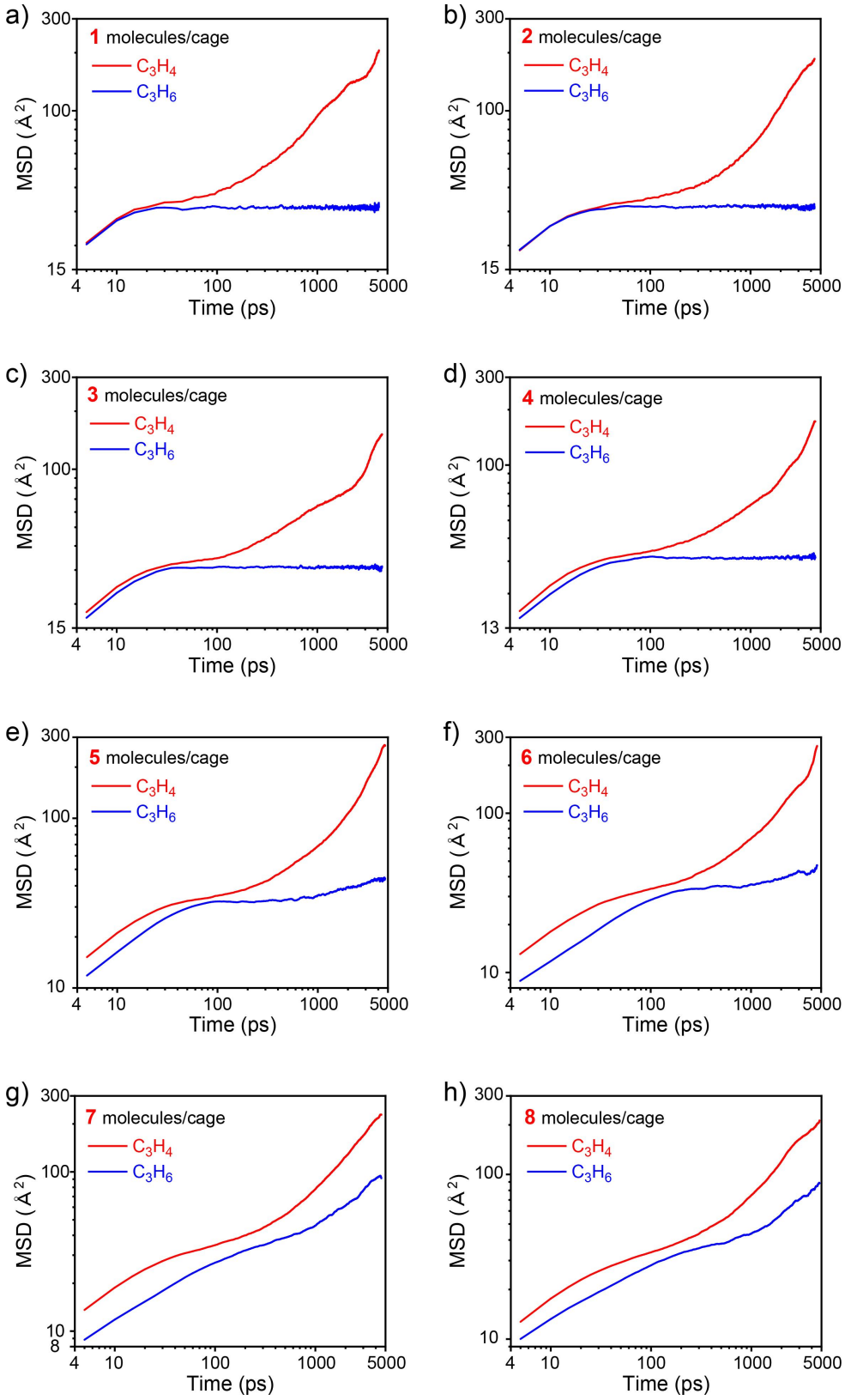

Fig. S70 MD simulations. MSD plot of C_3H_4 and C_3H_6 molecules in ZNU-2-Si with 1-8 molecules in a single cage.

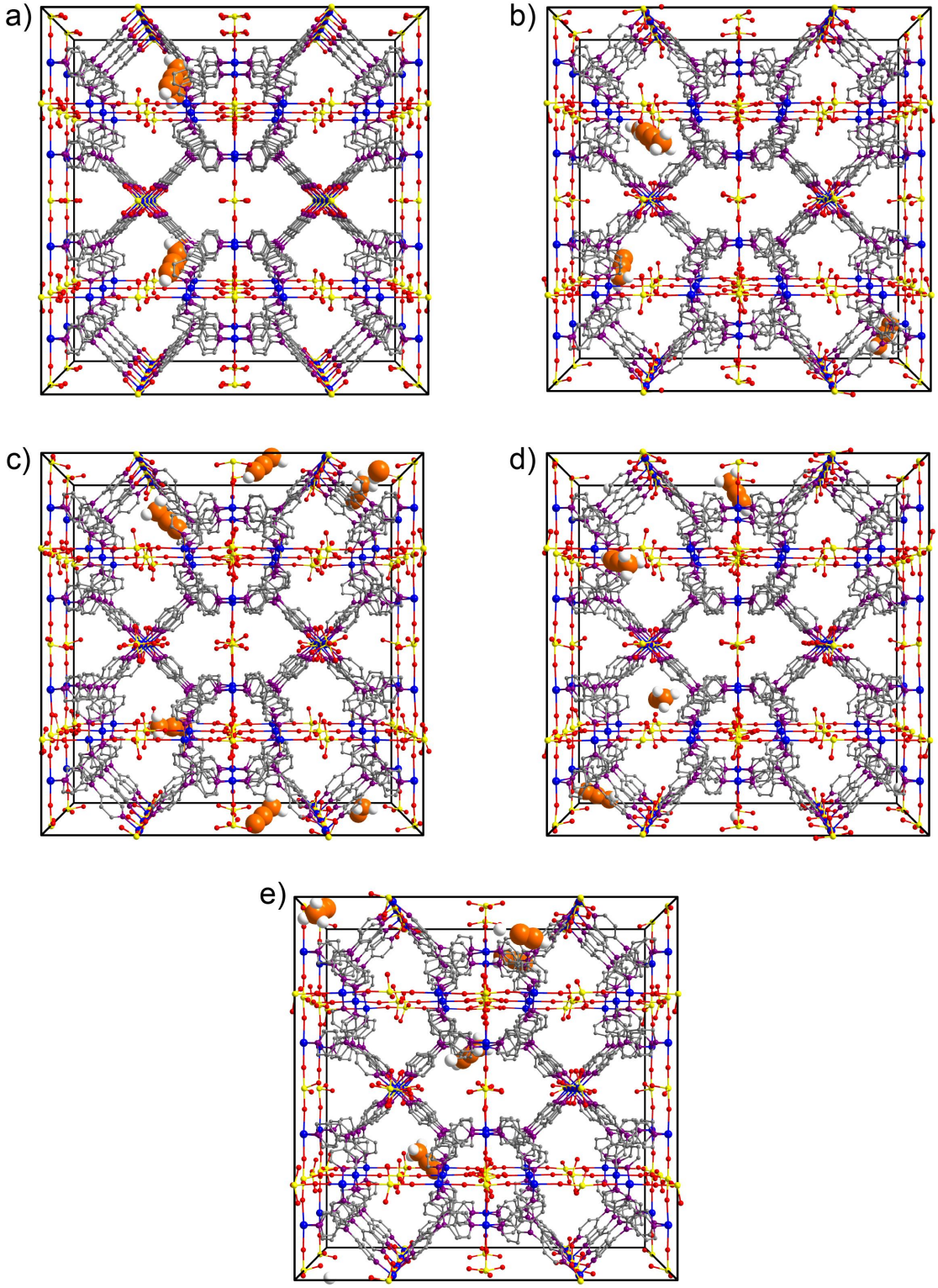

Fig. S71 MD simulations. Snapshots of MD simulation of C_3H_4 molecules in (a) 0, (b) 1250, (c) 2500, (d) 3750 and (e) 5000 ps under the loading of 1 C_3H_4/cage.

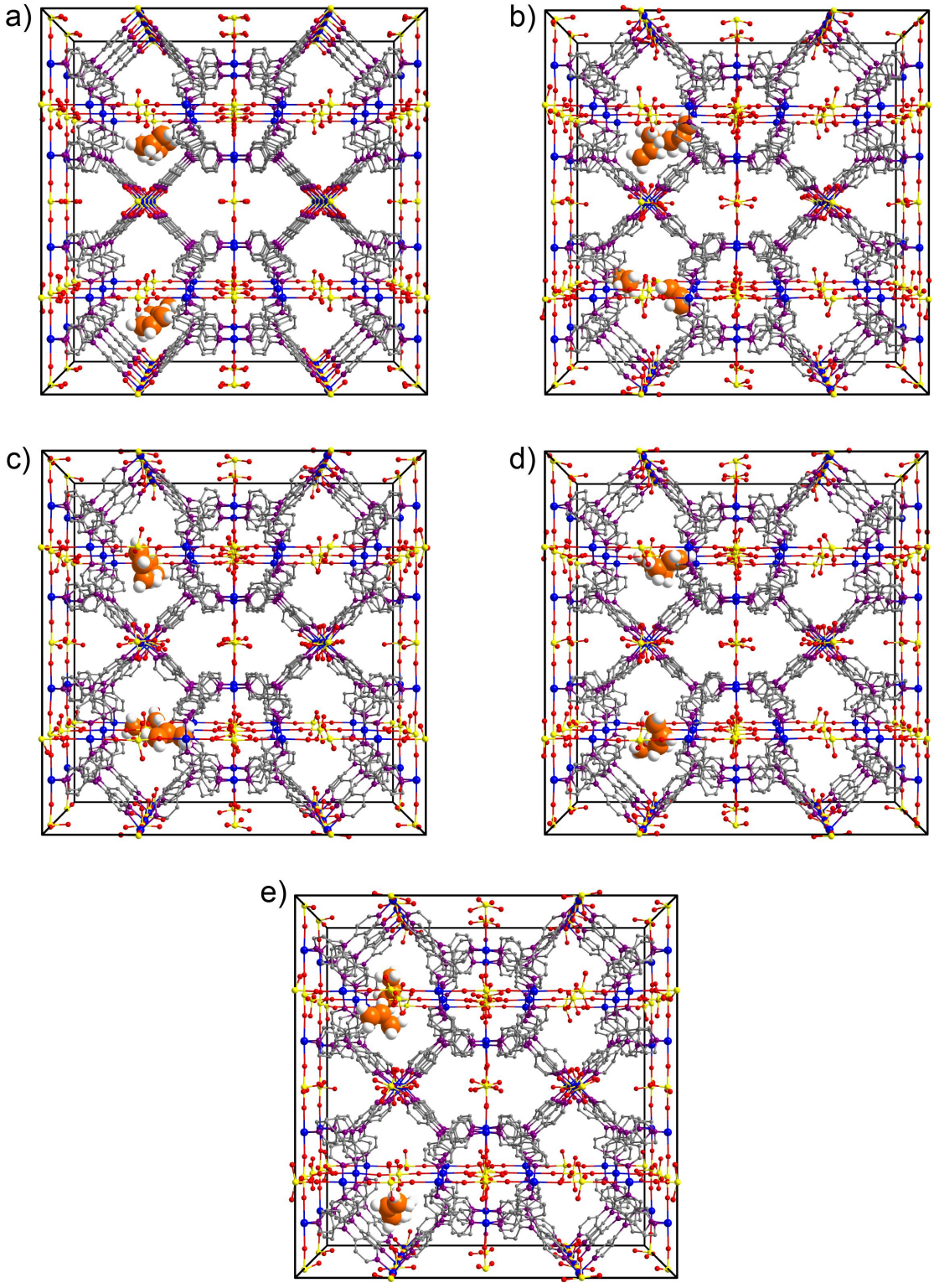

Fig. S72 MD simulations. Snapshots of MD simulation of C_3H_6 molecules in (a) 0, (b) 1250, (c) 2500, (d) 3750 and (e) 5000 ps, under the loading of 1 C_3H_6/cage.

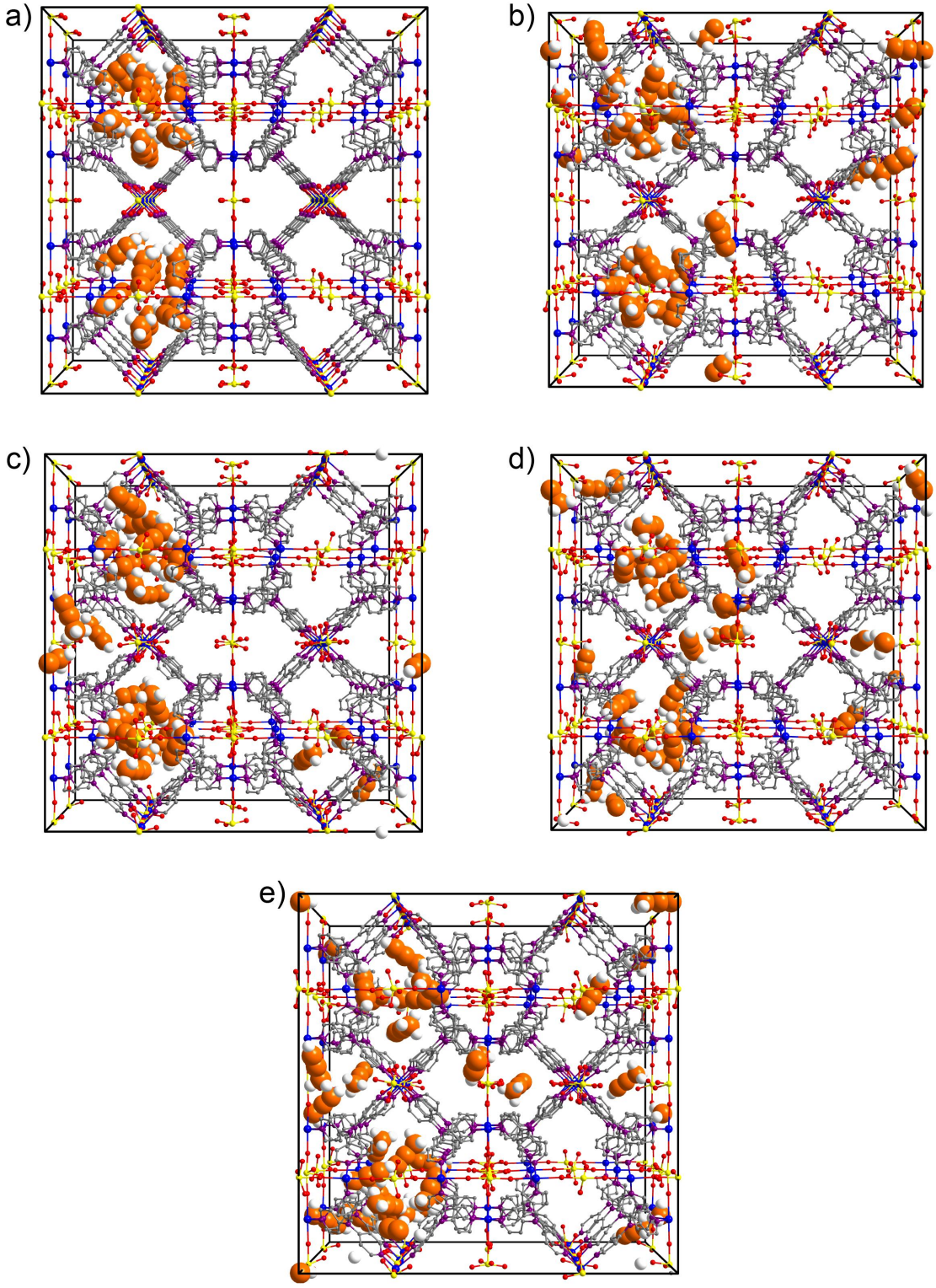

Fig. S73 MD simulations. Snapshots of MD simulation of C_3H_4 molecules in (a) 0, (b) 1250, (c) 2500, (d) 3750 and (e) 5000 ps, under the loading of 7 C_3H_4/cage.

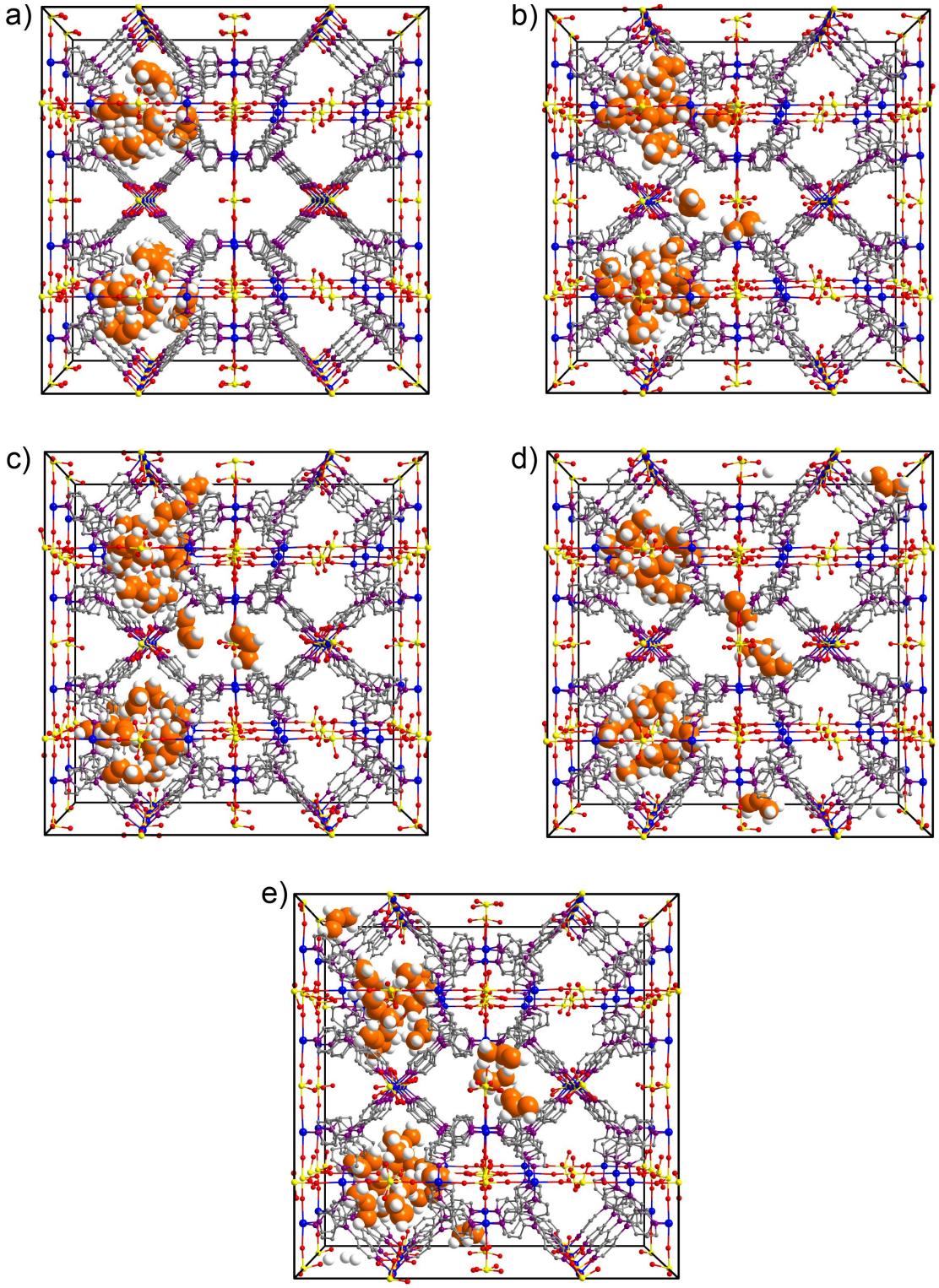

Fig. S74 MD simulations. Snapshots of MD simulation of C_3H_6 molecules in (a) 0, (b) 1250, (c) 2500, (d) 3750 and (e) 5000 ps, under the loading of 7 C_3H_6/cage.

Table S20 The diffusion coefficient of C_3H_4 and C_3H_6 on ZNU-2-Si.

Group	**C_3H_4_Slope**	**C_3H_6_Slope**	**C_3H_4_diffusion coefficient ($m^2 \cdot s^{-1}$)**	**C_3H_6_diffusion coefficient ($m^2 \cdot s^{-1}$)**
1 molecule	0.02832	4.08E-05	4.72E-11	6.79E-14
2 molecules	0.03908	5.86E-05	6.51333E-11	9.76352E-14
3 molecules	0.02512	9.40E-05	4.18667E-11	1.567E-13
4 molecules	0.02934	2.79E-04	4.89E-11	4.64478E-13
5 molecules	0.05144	0.00284	8.57333E-11	4.73333E-12
6 molecules	0.03942	0.00245	6.57E-11	4.08333E-12
7 molecules	0.04529	0.01499	7.54833E-11	2.49833E-11
8 molecules	0.0449	0.0122	7.48333E-11	2.03333E-11

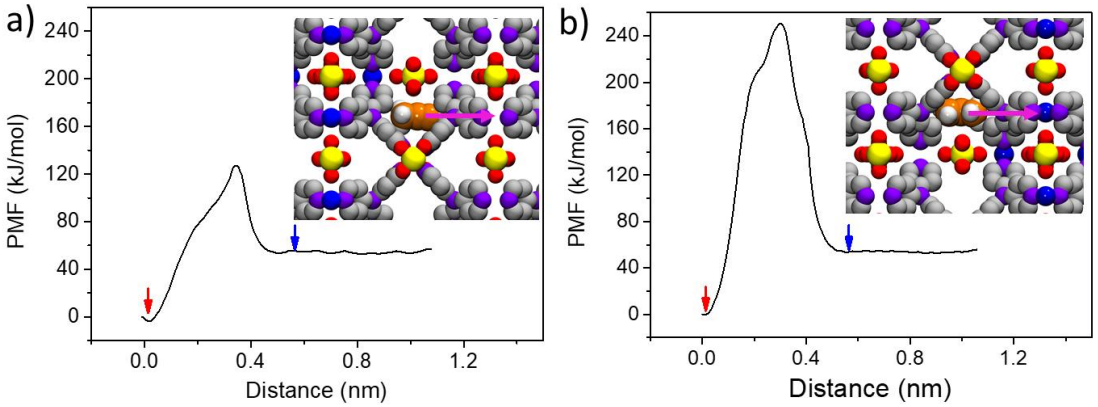

Fig. S75 Potential of mean forces (PMFs) for pulling a C_3H_4 (a) and C_3H_6 (b) from the narrow channel (indicated by red arrow) to cage-like pores (indicated by blue arrow). Insert: Magenta arrows represent the pulling direction of C_3H_4 and C_3H_6 during PMF calculations.

For the above MD simulation, the framework is considered flexible except the Cu atoms. Thus the pyridine ring and SiF_6^{2-} can be rotational and the pore window between the narrow channel and the cage can be expanded to allow guest to transport successfully. These result are consistent with the experiments.

We also tried MD simulation considering the framework is completely rigid. In this case both C_3H_4 and C_3H_6 are very difficult to diffuse from one cage to another due to the limitation of the over-contracted pore window (4.0 Å). Therefore, another method, i.e. comparison of the potential of mean forces, was applied. The free energies of C_3H_4 and C_3H_6 moving from the narrow channel to the cage-like pore were detected by the potential of mean force (PMF) method. The results show that C_3H_4 has lower free energy barrier than C_3H_6, suggesting that C_3H_4 is much easier to transport from channel to cage-like pores than C_3H_6.

VII Breakthrough simulations and experiments

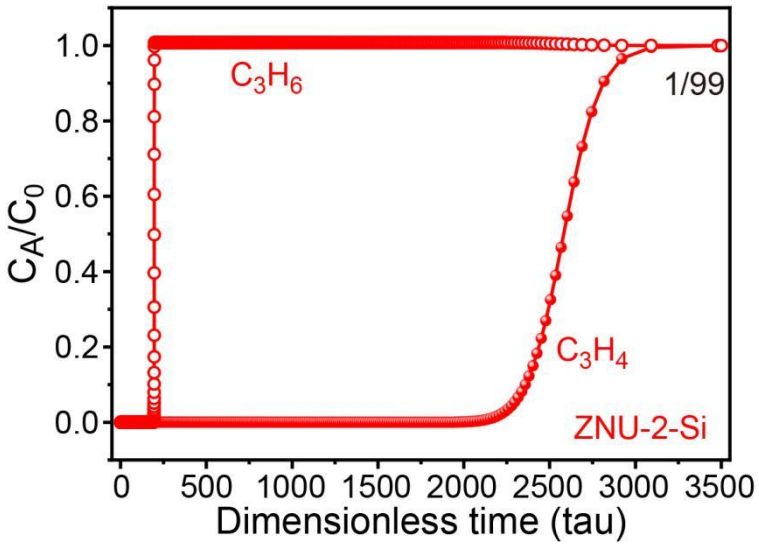

Fig. S76 Simulated breakthrough curves of ZNU-2-Si for C_3H_4/C_3H_6 (1/99) at 298 K.

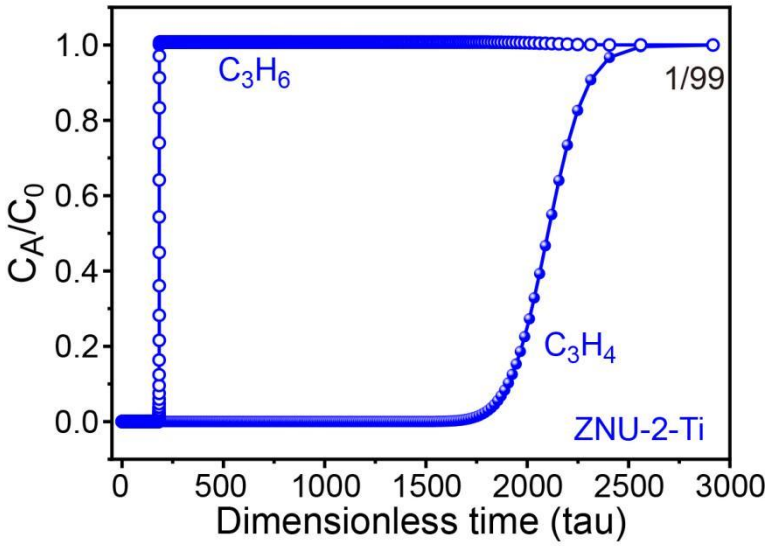

Fig. S77 Simulated breakthrough curves of ZNU-2-Ti for C_3H_4/C_3H_6 (1/99) at 298 K.

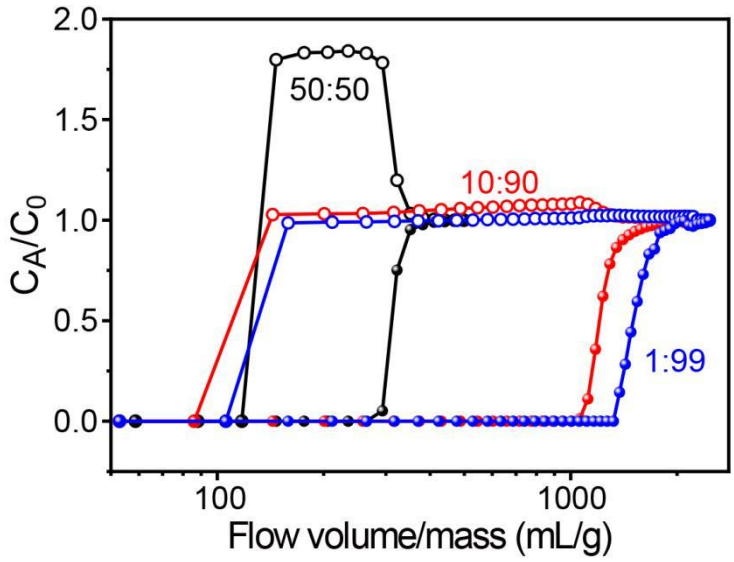

Fig. S78 Comparison of the experimental dynamic breakthrough curves of ZNU-2-Si. Breakthrough for C_3H_4/C_3H_6 with different ratios. Breakthrough conditions: flow rate 4.1 mL/min (50/50), 4.0 mL/min (10/90), 4.3 mL/min (1/99) at 298 K.

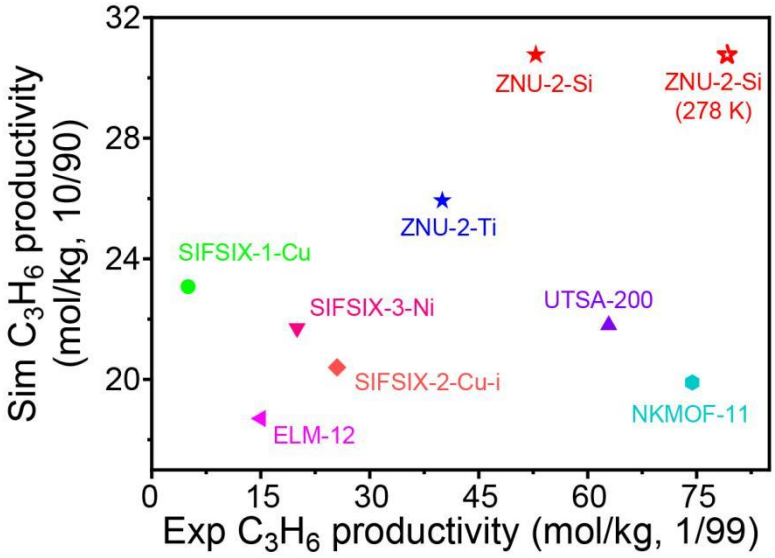

Fig. S79 Comparison of the C_3H_6 productivity from 10/90 (sim) and 1/99 (exp) C_3H_4/C_3H_6.

Table S21 Experimental dynamic C_3H_6 productivity and C_3H_4 uptake for ZNU-2-Si from different gas ratios and under different temperatures.

Conditions	Experimental C_3H_6 productivity (mol/kg)	Experimental C_3H_4 captured amount (mol/kg)
v/v 50/50 298 K	5.38	7.06
v/v 10/90 298 K	37.81	5.54
v/v 1/99 298 K	52.86	0.69
v/v 1/99 278 K	79.20	1.05
v/v 1/99 308 K	47.19	0.30

Table S22 Comparison of the C_3H_6 productivity from 10/90 and 1/99 C_3H_4/ C_3H_6.

	Simulated C_3H_6 productivity from 10/90 mixtures (mol/kg)	Experimental C_3H_6 productivity from 1/99 mixtures (mol/kg)
SIFSIX-1-Cu	23.08	5.0
UTSA-200	21.8	62.9
SIFSIX-3-Ni	21.7	20.0
SIFSIX-2-Cu-i	20.4	25.5
ELM-12	18.7	15.0
NKMOF-11	19.9	74.4
ZNU-2-Ti	25.93 (25.50)[a]	42.0
ZNU-2-Si	30.76 (37.81)[a]	52.9/79.20[b]
[a] Experimental values; [b] 278 K		

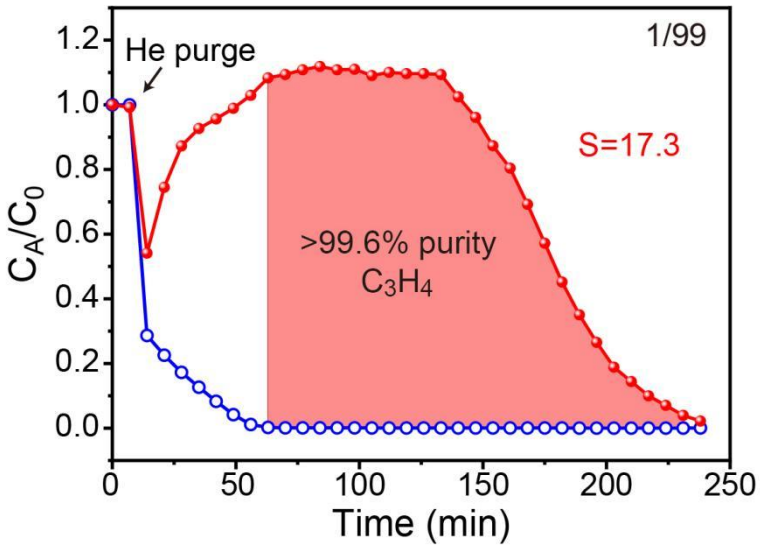

Fig. S80 Experimental dynamic desorption curves of ZNU-2-Si after breakthrough experiment of C_3H_4/C_3H_6 (1/99). Desorption conditions: Ar flow rate 5 mL/min at 348 K.

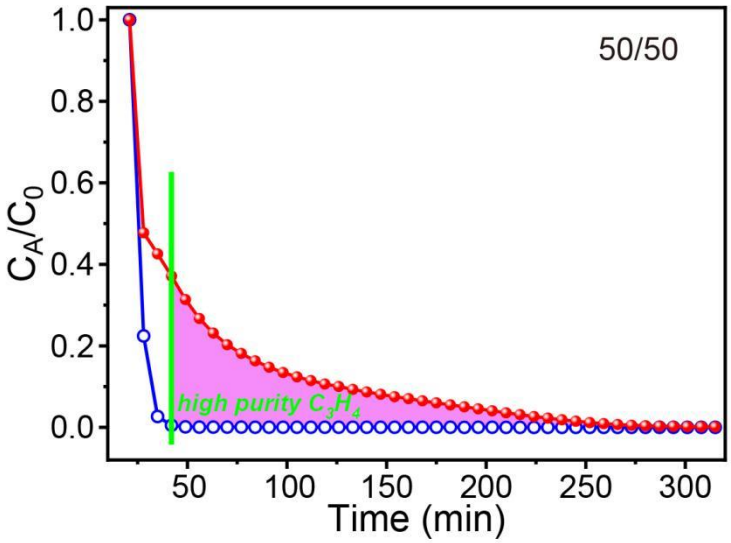

Fig. S81 Experimental dynamic desorption curves of ZNU-2-Si after breakthrough experiment of C_3H_4/C_3H_6 (50/50). Desorption conditions: Ar flow rate 5 mL/min at 348 K. The calculated amount of >99 % purity C_3H_4 (pink area) is 4.7 mmol/g.

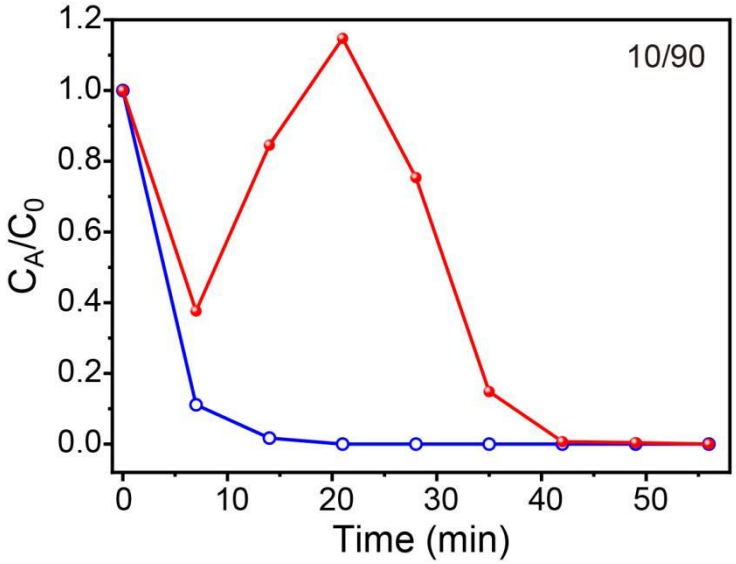

Fig. S82 Experimental dynamic desorption curves of ZNU-2-Si after breakthrough experiment of C_3H_4/C_3H_6 (10/90). Desorption conditions: Ar flow rate 20 mL/min at 393 K.

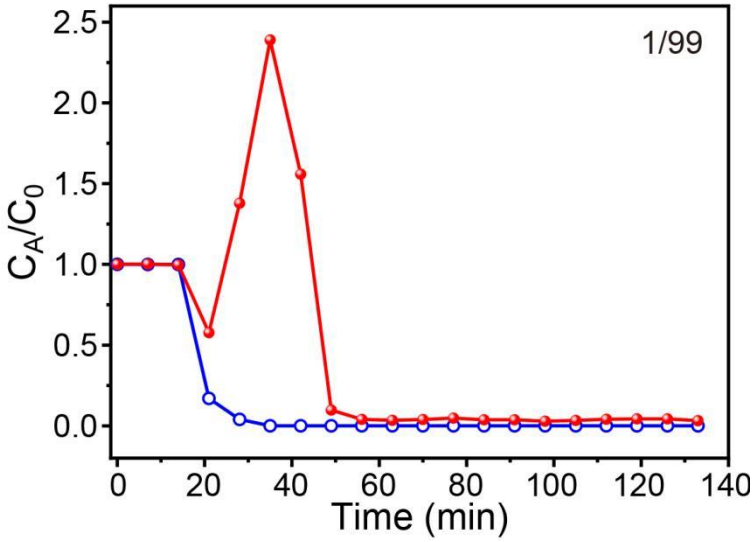

Fig. S83 Experimental dynamic desorption curves of ZNU-2-Si after breakthrough experiment of C_3H_4/C_3H_6 (1/99). Desorption conditions: Ar flow rate 20 mL/min at 393 K.

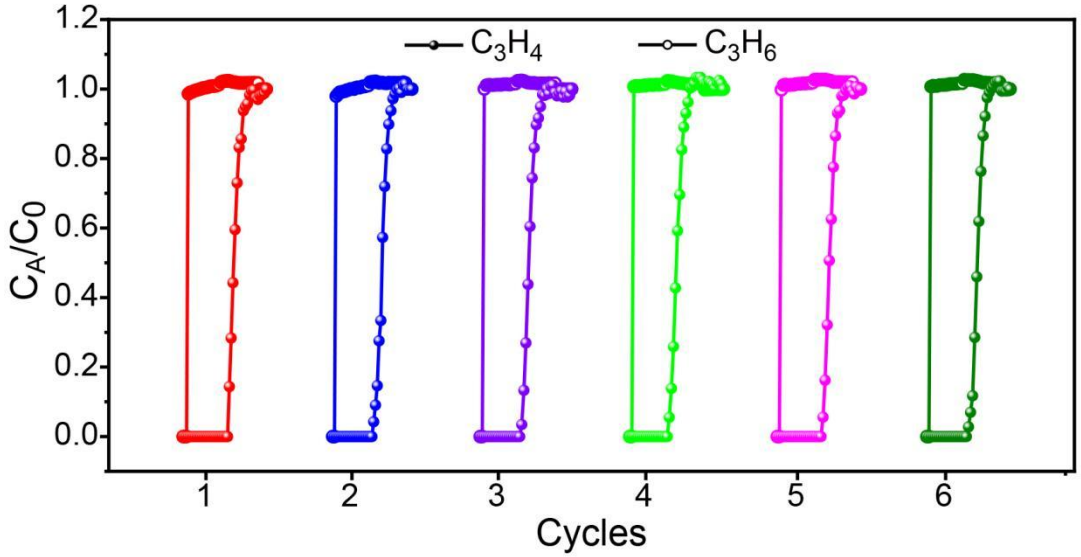

Fig. S84 Six cycles of experimental breakthrough curves of ZNU-2-Si for C_3H_4/C_3H_6 (1/99) at 298 K. (Activation condition of ZNU-2-Si between circles: Ar flow rate 20 mL/min at 393 K).

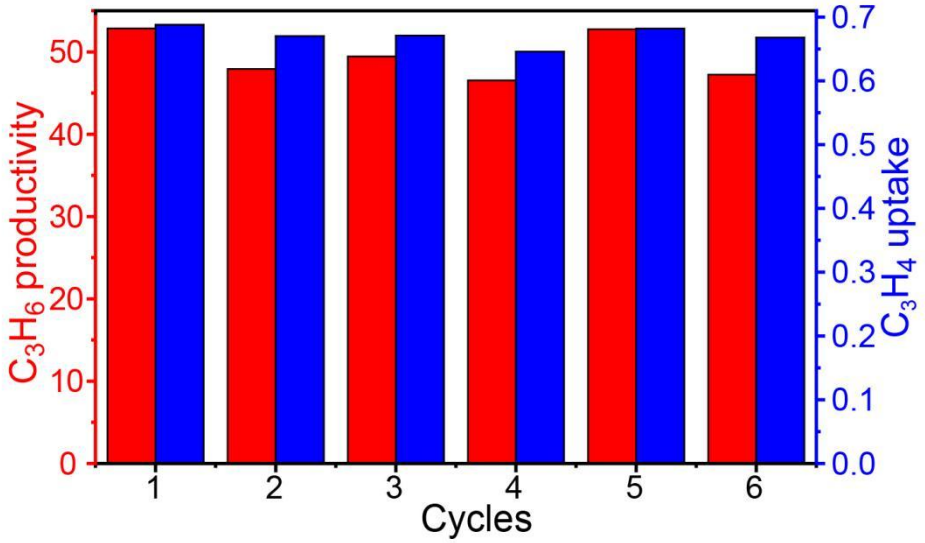

Fig. S85 Comparison of figures for dynamic C_3H_6 production and C_3H_4 uptake of ZNU-2-Si for C_3H_4/C_3H_6 (1/99) at 298 K in 6 cycles (activation condition of ZNU-2-Si between circles: Ar flow rate 20 mL/min at 393 K).

VIII Stability test

Table S23 Comparison of the stability of ZNU-2 with other reported materials in the context of C_3H_4/C_3H_6 separation .

Materials	thermal stability (℃)	air stability	stability in humid air	water stability	stability in acid	stability in base	cycling stability	Ref
ELM-12	295	-	-	√	-	-	√	[1, 17, 18]
ZU-62	230	√	√	√	-	-	√	[14, 19]
SIFSIX-2-Cu-i	170	√	√	×	-	-	√	[20-23]
ZJUT-1	232	√	√	√	-	-	√	[2]
GeFSIX-14-Cu-i	220	-	×	×	-	-	√	[13, 21]
TIFSIX-14-Cu-i	230	-	-	-	-	-	√	[13]
NKMOF-11	-	-	√	√	√	√	√	[3]
JXNU-6	365	-	-	-	-	-	-	[4]
SIFSIX-1-Cu	150	-	×	×	-	-	√	[5, 24, 22]
SIFSIX-3-Ni	264	√	√	×	-	-	√	[5, 22]
SIFSIX-3-Zn	157	-	×	×	-	-	√	[20, 25, 26]

Continued

NbOFFIVE-1-Ni	303	-	√	√	-	-	√	[27-29]
UTSA-200	201	-	×	×	-	-	√	[6, 22, 30]
NKMOF-1-Ni	382	√	√	√	√	√	√	[7, 31]
NKMOF-1-Cu	214	√	√	√	√	√	-	[7, 31]
GeFSIX-dps-Cu	214	√	√	√	-	-	√	[8]
Co-gallate	276	√	-	-	-	-	√	[10]
Mg-gallate	401	√	-	-	-	-	-	[10]
Ni-gallate	290	√	-	-	-	-	-	[10]
Ca-based MOF	520	√	√	√	√	√	-	[11]
Cu-BTC	306	√	×	×	-	-	√	[16, 32-34]
FJI-W1	200	√	√	√	-	-	√	[35]
ZNU-2-Si	**250**	√	√	√	√	√	√	**this work**
ZNU-2-Ti	**308**	√	√	√	√	√	√	**this work**
ZNU-2-Nb	**300**	√	√	√	√	√	√	**this work**

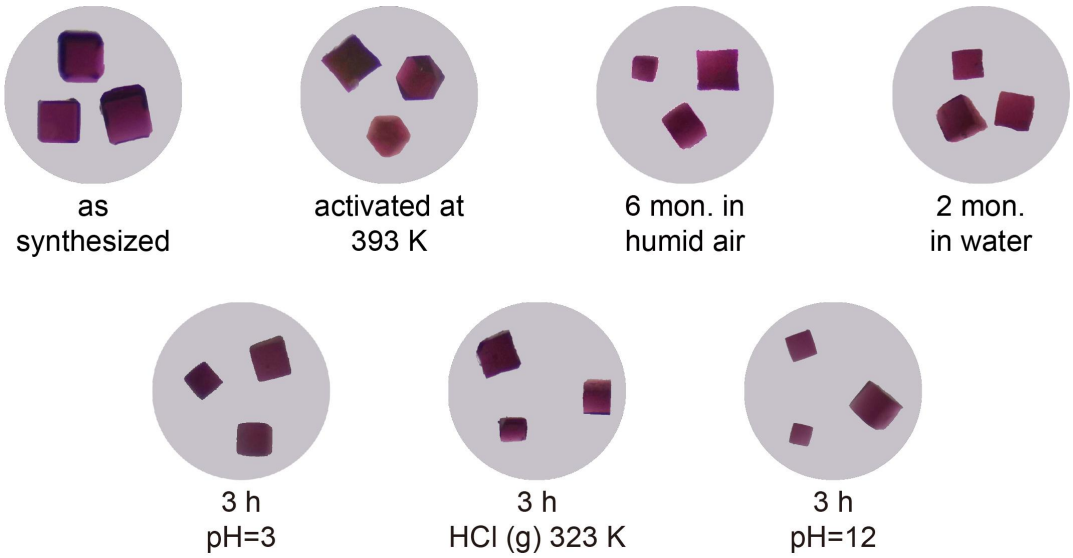

Fig. S86 Photographs of single crystals of ZNU-2-Si after different treatments showing the high stability of ZNU-2-Si after exposure to 393 K heating under vacuum, humid air, water, acid aqueous solution, basic aqueous solution, and acid vapor.

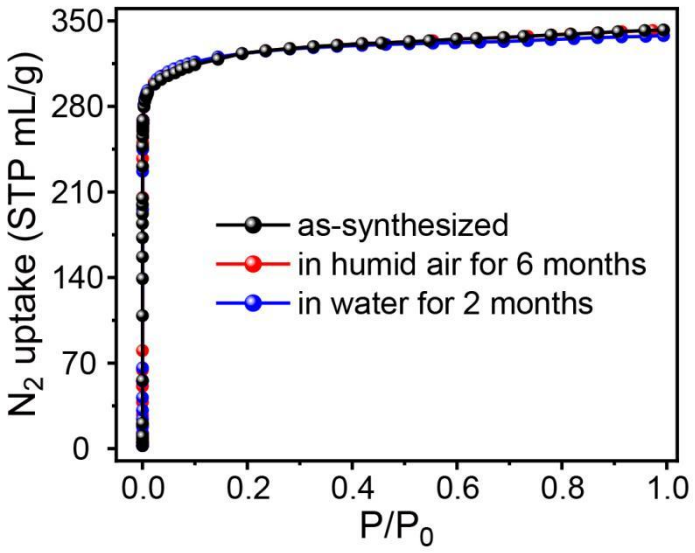

Fig. S87 The adsorption isotherm of N_2 at 77 K on as-synthesized ZNU-2-Si, and ZNU-2-Si after exposure to humid air for 6 months ,soaking in water for 2 months.

Analysis: The overlapping of the N_2 adsorption isotherms on ZNU-2-Si further suggests its good stability.

Table S25 Comparison of the crystallographic parameters of as-synthesized ZNU-2-Si and ZNU-2-Si after multiple sorptions.

Materials	ZNU-2-Si (as-synthesized)	ZNU-2-Si (after multiple sorption experiments)
Cell	a=17.5318(3)	a=17.5267(3)
	b=17.5318(3)	b=17.5267(3)
	c=17.5318(3)	c=17.5267(3)
	α=90	α=90
	β=90	β=90
	γ=90	γ=90
Temperature	293 K	293 K
Volume ($Å^3$)	5388.6(3)	5383.9(3)
Space group	Pm-3n	Pm-3n
Hall group	-P 4n 2 3	-P 4n 2 3
formula	$C_{20}H_{16}CuF_6N_{5.33}Si$	$C_{20}H_{16}CuF_6N_{5.33}Si$
MW	536.69	536.69
density	0.992	0.993
Z	6	6
R	0.0530(887)	0.0529(904)
wR2	0.1813(1142)	0.1875(1141)
S	1.133	1.131
CCDC Nos.	2190368	2190369

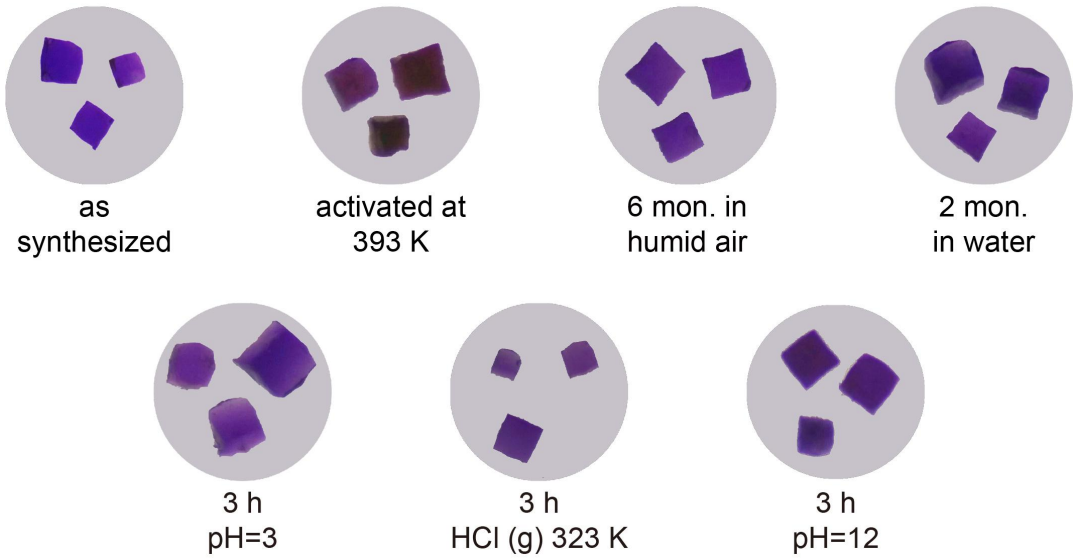

Fig. S88 Photographs of single crystals of ZNU-2-Ti after different treatments showing the high stability of ZNU-2-Ti after exposure to 393 K heating under vacuum, humid air, water, acid aqueous solution, basic aqueous solution, and acid vapor.

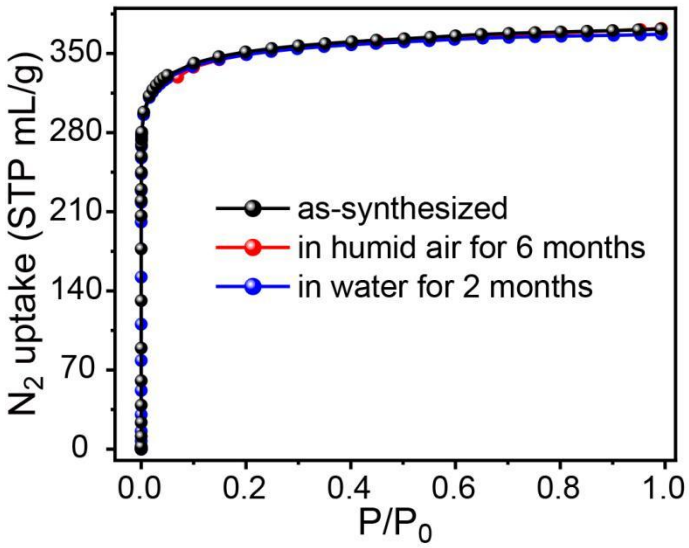

Fig. S89 The adsorption isotherm of N_2 at 77 K on as-synthesized ZNU-2-Ti, and ZNU-2-Ti after exposure to humid air for 6 months ,soaking in water for 2 months。

Analysis: The overlapping of the N_2 adsorption isotherms on ZNU-2-Ti further suggests its good stability.

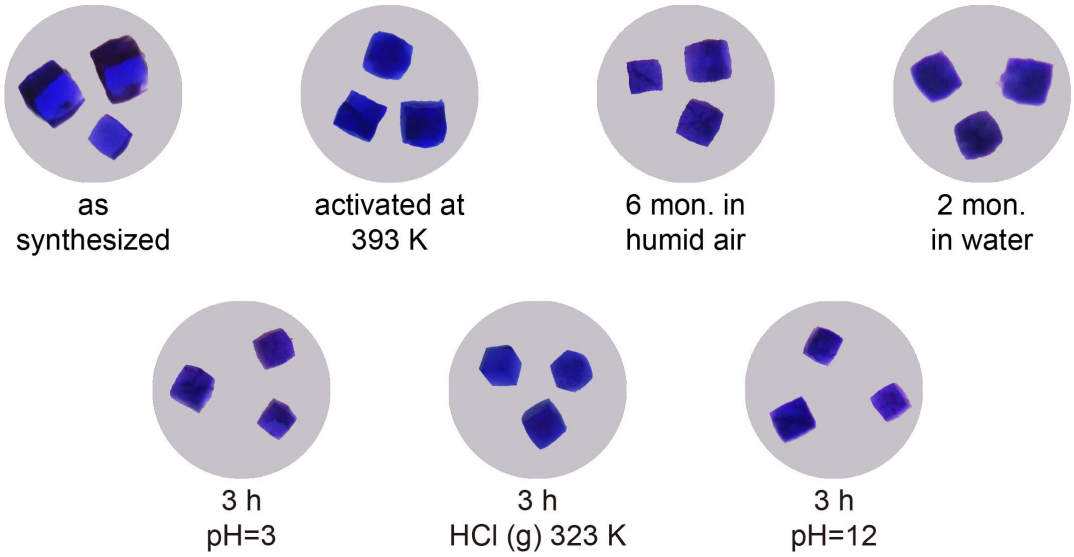

Fig. S90 Photographs of single crystals of ZNU-2-Nb after different treatments showing the high stability of ZNU-2-Nb after exposure to 393 K heating under vacuum, humid air, water, acid aqueous solution, basic aqueous solution, and acid vapor.

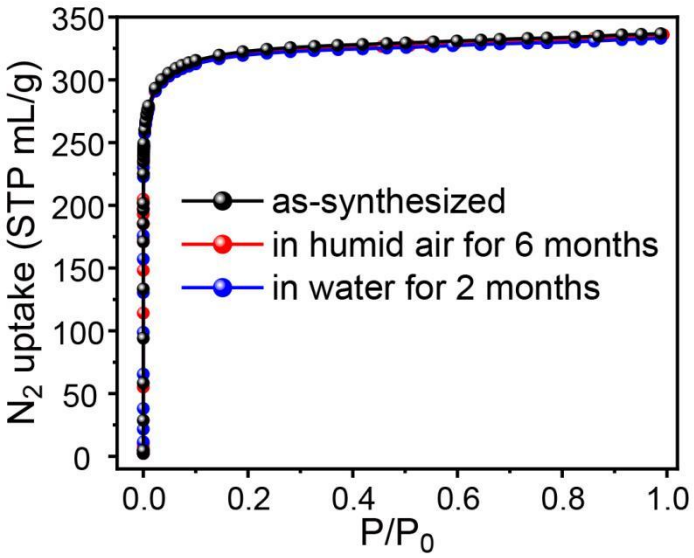

Fig. S91 The adsorption isotherm of N_2 at 77 K on as-synthesized ZNU-2-Nb, and ZNU-2-Nb after exposure to humid air for 6 months ,soaking in water for 2 months.

Analysis: The overlapping of the N_2 adsorption isotherms on the ZNU-2-Nb further suggests its good stability.

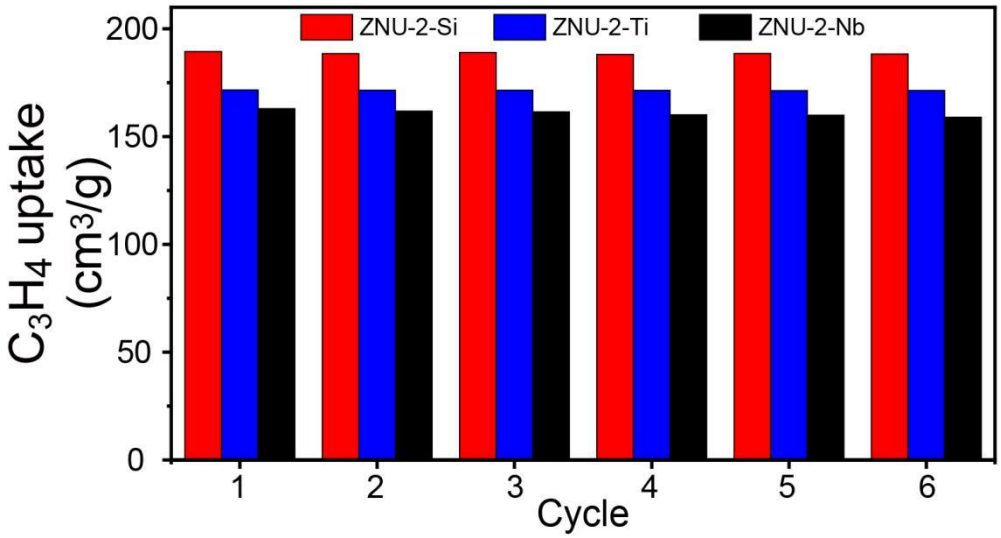

Fig. S92 Comparison of C_3H_4 uptake on the ZNU-2 family at 298 K and 1.0 bar for six cycles.

The retaining of the C_3H_4 uptake on the ZNU-2 family further suggests the good recyclability and stability for applications.

IX References

[1] Li, L. et al. Flexible–Robust Metal–Organic Framework for Efficient Removal of Propyne from Propylene. *J. Am. Chem. Soc.* **139**, 7733-7736 (2017).

[2] Wen, H.-M. et al. Fine-tuning of nano-traps in a stable metal-organic framework for highly efficient removal of propyne from propylene. *J. Mater. Chem. A* **6**, 6931-6937 (2018).

[3] Peng, Y.-L. et al. A robust heterometallic ultramicroporous MOF with ultrahigh selectivity for propyne/propylene separation. *J. Mater. Chem. A* **9**, 2850-2856 (2021)..

[4] Lin, Z. T. et al. Fluorinated Biphenyldicarboxylate-Based Metal-Organic Framework Exhibiting Efficient Propyne/Propylene Separation. *Inorg. Chem.* **59**, 4030-4036 (2020).

[5] Yang, L.et al. A Single-Molecule Propyne Trap: Highly Efficient Removal of Propyne from Propylene with Anion-Pillared Ultramicroporous Materials. *Adv. Mater.* **30**, 1705374 (2018).

[6] Li, L. et al. A Metal-Organic Framework with Suitable Pore Size and Specific Functional Sites for the Removal of Trace Propyne from Propylene. *Angew. Chem. Int. Ed.* **57**, 15183-15188 (2018).

[7] Peng, Y. L. et al. Robust Microporous Metal-Organic Frameworks for Highly Efficient and Simultaneous Removal of Propyne and Propadiene from Propylene. *Angew. Chem. Int. Ed.* **58**, 10209-10214 (2019).

[8] Ke, T. et al. Molecular Sieving of C_2-C_3 Alkene from Alkyne with Tuned Threshold Pressure in Robust Layered Metal-Organic Frameworks. *Angew. Chem. Int. Ed.* **59**, 12725-12730 (2020).

[9] Yu, B. et al. A Solid Transformation into Carboxyl Dimers Based on a Robust Hydrogen-Bonded Organic Framework for Propyne/Propylene Separation. *Angew. Chem. Int. Ed.* **60,** 25942-25948 (2021).

[10] Li, Z. et al. Gallate-Based Metal-Organic Frameworks for Highly Efficient Removal of Trace Propyne from Propylene. *Ind. Eng. Chem. Res.* **59**, 13716-13723 (2020).

[11] Li, L. et al. Calcium-Based Metal-Organic Framework for Simultaneous Capture

of Trace Propyne and Propadiene from Propylene. *ACS Appl. Mater. Interfaces* **12**, 17147-17154 (2020).

[12] Zhang, Z. et al. Fine-Tuning Pore Dimension in Hybrid Ultramicroporous Materials Boosting Simultaneous Trapping of Trace Alkynes from Alkenes. *Small* **16**, 2005360 (2020).

[13] Yang, L. et al. A highly sensitive flexible metal-organic framework sets a new benchmark for separating propyne from propylene. *J. Mater. Chem. A* **6**, 24452-24458 (2018).

[14] Yang, L. et al. An Asymmetric Anion-Pillared Metal-Organic Framework as a Multisite Adsorbent Enables Simultaneous Removal of Propyne and Propadiene from Propylene. *Angew. Chem. Int. Ed.* **57**, 13145-13149 (2018).

[15] Jiang, Y. et al. Comprehensive Pore Tuning in an Ultrastable Fluorinated Anion Cross-Linked Cage-Like MOF for Simultaneous Benchmark Propyne Recovery and Propylene Purification. *Angew. Chem. Int. Ed.* **61**, e202200947 (2022).

[16] Peng, Y. L. et al. Efficient propyne/propadiene separation by microporous crystalline physiadsorbents. *Nat. Commun.* **12**, 5768 (2021).

[17] Kondo, A. et al. Double−Step Gas Sorption of a Two−Dimensional Metal−Organic Framework. *J. Am. Chem. Soc.* **129,** 12362–12363 (2007).

[18] Sotomayor, F. J. Lastoskie, C. M. Carbon dioxide capacity retention on elastic layered metal organic frameworks subjected to hydrothermal cyclin. *Microporous Mesoporous Mater*. *304,* 110377 (2020).

[19] Wang, Q. et al. Separation of Xe from Kr with Record Selectivity and Productivity in Anion-Pillared Ultramicroporous Materials by Inverse Size-Sieving. *Angew. Chem. Int. Ed.* **59,** 3423-3428 (2020).

[20] Cui, X. et al. Pore chemistry and size control in hybrid porous materials for acetylene capture from ethylene. *Science* **353**, 141-144 (2016).

[21] Zhang, Z. et al. Sorting of C4 Olefins with Interpenetrated Hybrid Ultramicroporous Materials by Combining Molecular Recognition and Size-Sieving. *Angew. Chem. Int. Ed.* **56**, 16282-16287 (2017).

[22] O'Nolan, D. et al. Water Vapor Sorption in Hybrid Pillared Square Grid

Materials. *J. Am. Chem. Soc.* **139**, 8508-8513 (2017).

[23] Yang, L. et al. A novel interpenetrated anion-pillared porous material with high water tolerance afforded efficient C_2H_2/C_2H_4 separation. *Chem. Commun.* **55**, 5001-5004 (2019).

[24] Noro, S. et al. Framework Engineering by Anions and Porous Functionalities of Cu(II)/4,4'-bpy Coordination Polymers. *J. Am. Chem. Soc.* **124**, 2568-2583 (2002).

[25] Nugent, P. et al. Porous materials with optimal adsorption thermodynamics and kinetics for CO_2 separation. *Nature* **495**, 80-84 (2013).

[26] Meng, S. S. et al. Ultramicroporous metal-organic frameworks for capillary gas chromatographic separation. *J. Chromatogr. A* **1632**, 461604 (2020).

[27] Bhatt, P. M. et al. A Fine-Tuned Fluorinated MOF Addresses the Needs for Trace CO_2 Removal and Air Capture Using Physisorption. *J. Am. Chem. Soc.* **138**, 9301-9307 (2016).

[28] Khraisheh, M. et al.Effective Separation of Prime Olefins from Gas Stream Using Anion Pillared Metal Organic Frameworks: Ideal Adsorbed Solution Theory Studies, Cyclic Application and Stability. *Catalysts* **11**, 510 (2021).

[29] Chen, K. et al. Enhanced CO_2/CH_4 separation performance of mixed-matrix membranes through dispersion of sorption-selective MOF nanocrystals. *J. Membr. Sci.* **563**, 360-370 (2018).

[30] Li, B. et al. An Ideal Molecular Sieve for Acetylene Removal from Ethylene with Record Selectivity and Productivity. *Adv. Mater.* **29**, 1704210 (2017).

[31] Peng, Y. L. et al. Robust Ultramicroporous Metal–Organic Frameworks with Benchmark Affinity for Acetylene. *Angew. Chem. Int. Ed.* **57**, 10971-10975 (2018).

[32] Xu, S. et al. Methyl-Shield Cu-BTC with High Water Stability through One-Step Synthesis and In Situ Functionalization *Ind. Eng. Chem. Res.* **59**, 12451-12457 (2020).

[33] Sun, Y. et al. Room-Temperature Synthesis of $Pyr_{1/3}$@Cu–BTC with Enhanced Stability and Its Excellent Performance for Separation of Propylene/Propane. *Ind. Eng. Chem. Res.* **59**, 6202-6209 (2020).

[34] Kumar, A. et al. Direct Air Capture of CO_2 by Physisorbent Materials. *Angew.*

Chem. Int. Ed. **54**, 14372-14377 (2015).

[35] Zou, S. et al. Stable Fluorinated Hybrid Microporous Material for the Efficient Separation of C_2-C_3 Alkyne/Alkene Mixtures. *Inorg. Chem.* **61**, 7530-7536 (2022).